Tampere University

Jonna Jokela

DESIGN OF AN ELECTROMAGNETIC COIL ARRAY FOR WIRELESS ENDOSCOPE CAPSULE LOCALIZATION

Master's Thesis
Faculty of Medicine and Health Technology
Supervisors: Dr. Bachir Dekdouk, Prof. Jari Hyttinen
Examiners: Prof. Jari Hyttinen, Dr. Nikta Pournoori
May 2023

ABSTRACT

Jonna Jokela: Design of an Electromagnetic Coil Array for Wireless Endoscope Capsule Localization
Master's Thesis
Tampere University
Master's Programme in Biotechnology and Biomedical Engineering
May 2023

Wireless capsule endoscopy is a technique that visualizes mucosa of gastrointestinal tract. The first wireless capsule endoscope was developed in 2001, and since then, the technology has been in constant development. With its reduced amount of discomfort, ability to visualize the whole gastrointestinal tract and many interesting future prospects, capsule endoscopy is challenging the conventional procedure, in which a camera module at the end of a tube is inserted to the gastrointestinal tract. In general, the method can be used to diagnose many diseases, such as cancers, Celiac disease and Crohn's disease.

In order to achieve all the future prospects of the technology, for example, active steering of the capsule, biopsy and drug-delivery with the capsule, challenge of detecting the capsule's position and orientation inside human needs to be overcome. Therefore, the localization challenge is considered in this thesis. The aim is to select an optimal method for localization based on current research, and to model and develop a prototype that could be utilized in capsule localization. The designed sensor array is evaluated with the help of finite element method -based modelling, sensitivity analysis and practical experiments.

Based on the studied literature, an active magnetic field strength -based localization technique was selected for further analysis. According to the literature, the method provides high accuracy and could also be utilized in other purposes, for example, wireless charging and active locomotion of the capsule. In addition, the method does not suffer from attenuation of the fields within a human body. Therefore, theoretical basis of the magnetic field strength -based localization was presented, and four electromagnetic coil arrays were designed for sensitivity analysis. Contrary to many developed arrays seen in the literature review, all the designed systems were planar, in order to develop a system that could be fitted, for instance, inside a hospital bed. Based on the sensitivity analysis, an array with relatively large sensitivity and optimal number of measurement channels was selected for practical study. In addition, possible markers that could be fitted inside a regular sized endoscopic capsule were numerically modelled. It was found that a resonated solenoid marker with ferrite core causes the largest voltage compared to other modelled targets, and therefore it was constructed for experiments.

The whole array was built and equipped with electronics and measurement devices to be able to perform testing. Two channels of the array were selected for example measurements, and the results were analysed and compared with modelled values and sensitivity patterns. The system was tested at multiple different heights and positions, and the effect of changing the marker's orientation with respect to the array was analysed. It was found that the system gives a reasonable response when the marker is oriented along the excitation magnetic field. With this orientation, it was possible to measure significant voltages caused by the marker even at distance of 25 cm from the array. However, when the marker was oriented so that the excitation field could not properly excite it, the measured voltages got smaller. In addition, at certain orientation, the measured voltages did not seem reliable because voltage caused by the marker could not been discriminated from the noise of the system. The study indicates that the method is suitable for localization of resonated solenoid sample with ferrite core, but further improvements are needed to make the system work at each position and orientation of the marker. In addition, an inversion algorithm that estimates marker's position and orientation based on the measured voltage needs to be integrated to the system.

Keywords: wireless capsule endoscope, electromagnetic induction, sensitivity analysis, LC marker, magnetic dipole approximation, localization

TIIVISTELMÄ

Jonna Jokela: Sähkömagneettisen kelajärjestelmän suunnittelu langattoman kapseliendoskoopin paikannukseen
Diplomityö
Tampereen yliopisto
Bioteknologian ja biolääketieteen tekniikan maisteriohjelma
Toukokuu 2023

Kapseliendoskopia on menetelmä, jonka avulla voidaan kuvata ruoansulatuskanavan limakalvoa. Ensimmäinen kapseliendoskooppi (Engl. Wireless capsule endoscope, WEC) kehitettiin vuonna 2001, ja siitä lähtien teknologia on jatkuvasti kehittynyt. Kapseliendoskopia haastaa perinteisen endoskopian, jossa putken päässä oleva kamerayksikkö työnnetään ruoansulatuskanavaan, sillä se vähentää toimenpiteen aiheuttamaa epämukavuutta. Menetelmää voidaan käyttää koko ruuansulatuskanavan kuvaamiseen, ja lisäksi teknologialla on monia kiinnostavia tulevaisuudennäkymiä. Menetelmää voidaan käyttää diagnosoimaan monia sairauksia, kuten syöpää, keliakiaa ja Crohnin tautia.

Jotta teknologian tulevaisuudennäkymät, kuten kapselin ohjaaminen kehon ulkopuolelta, biopsia ja täsmälääkitys voisivat onnistua, tulee kapselin sijainti ja suunta kehon sisällä selvittää. Sen vuoksi kapselin paikannusta tarkastellaan tässä työssä. Tavoitteena on valita ihanteellinen paikannusmenetelmä kirjallisuuteen perustuen, sekä mallintaa ja kehittää kyseiseen menetelmään perustuva prototyyppi. Järjestelmän toimintaa analysoidaan elementtimenetelmään perustuvan mallinnuksen, herkkyysanalyysin ja käytännön kokeiden perusteella.

Kirjallisuuden perusteella menetelmäksi valikoitui aktiivinen magneettikentän voimakkuuteen perustuva paikannus. Kirjallisuusanalyysi osoittaa, että menetelmä on tarkka, ja sitä on mahdollista hyödyntää myös muihin tarkoituksiin, kuten kapselin langattomaan lataamiseen ja liikuttamiseen. Menetelmässä hyödynnettävät magneettikentät eivät myöskään vaimene kulkiessaan ihmiskehon läpi. Tämän vuoksi magneettikenttien voimakkuuteen perustuvaan paikannukseen tarvittava teoria käytiin läpi, ja neljä erilaista sähkömaneettista käämijärjestelmää suunniteltiin herkkyysanalyysia varten. Toisin kuin monet kirjallisuuskatsauksessa nähdyt järjestelmät, kaikki työssä suunnitellut järjestelmät ovat tasomaisia, jotta ne voitaisiin asentaa esimerkiksi sairaalasängyn sisään. Yksi järjestelmä valittiin käytännön toteutukseen herkkyysanalyysin perusteella. Lisäksi muutama normaalikokoisen endoskopiakapselin sisään mahtuva markkeri mallinnettiin numeerisesti. Simulaatioissa huomattiin, että resonoitu, ferriittiytimellä varustettu solenoidimarkkeri aiheutti suurimman jännitemuutoksen muihin mallinnettuihin markkereihin verrattuna, ja siksi se rakennettiin mittauksia varten.

Koko järjestelmä, sekä sen vaatima elektroniikka ja mittalaitteet koottiin testausta varten, ja esimerkkimittaukset toteutettiin kahta mittauskanavaa hyödyntäen. Saatuja tuloksia verrattiin mallinnettuihin tuloksiin sekä herkkyysanalyysiin. Järjestelmää testattiin useilla eri markkerin sijainneilla ja kallistuskulmilla. Testimittausten perusteella järjestelmän avulla voidaan mitata markkerin aiheuttama jännitemuutos jopa 25 cm etäisyydellä käämeistä, kun markkeri on suuntautunut magneettikenttien mukaisesti. Jos markkerin kallistuskulma käämien suhteen muuttuu, mitattujen jännitteiden amplitudi pienenee, sillä tällöin magneettikenttä ei magnetisoi markkeria optimaalisesti. Lisäksi eräässä kallistuskulmassa järjestelmän mittaamat jännitteet eivät vaikuttaneet päteviltä, sillä markkerin aiheuttama pieni jännitemuutos peittyi järjestelmän häiriöiden alle. Tutkimus osoittaa, että menetelmä on sopiva resonoidun, ferriittiytimellä varustetun solenoidimarkkerin paikallistamiseen, mutta tiettyjä paranuksia tarvitaan, jotta järjestelmä toimisi kaikilla markkerin kallistuskulmilla ja sijainneilla. Lisäksi järjestelmä vaatii toimiakseen inversioalgoritmin, joka arvioi markkerin sijainnin ja kallistuskulman mitattujen jännitteiden perusteella.

Avainsanat: Kapseliendoskopia, sähkömagneettinen induktio, herkkyysanalyysi, LC markkeri, magneettinen dipoli, paikannus

PREFACE

This Master of Science thesis was conducted in the Computational Biophysics and Imaging Group (CBIG), Faculty of Medicine and Health Technology, Tampere University, Finland.

There are several people that I would like to thank for their support and guidance during the process. I would like to give a special thank to my supervisor Bachir Dekdouk for his guidance, encouragement and expertise. Also, I want to thank my supervisor Jari Hyttinen for giving me the opportunity to conduct my thesis in his group and for all the support during the project. Additionally, I would like to thank Anthony Peyton from University of Machester for sharing his knowledge and answering to questions about this work. Finally, I want to thank my family and friends for always supporting me.

Tampere, 8 May 2023

Jonna Jokela

CONTENTS

1. INTRODUCTION 1
2. BACKGROUND OF WIRELESS CAPSULE ENDOSCOPE LOCALIZATION 3
2.1 Wireless capsule endoscopy 3
2.1.1 Principle and structure of WEC 3
2.1.2 Advantages of WECs 5
2.1.3 Challenges of WECs 6
2.2 Methods for localization of WECs 8
2.2.1 Electromagnetic wave -based localization methods 9
2.2.2 Magnetic field strength -based localization methods 10
2.2.3 Other localization methods 13
2.2.4 Comparison of different localization methods 14
2.3 Motivation of the Thesis 16
3. THEORETICAL BACKGROUND 17
3.1 Electromagnetic induction 17
3.1.1 Faraday's law of induction 17
3.1.2 Biot-Savart law 19
3.1.3 Magnetic dipole moment 20
3.1.4 Magnetic polarizability tensor 21
3.2 Inverse problem 23
4. METHODS 26
4.1 Modelling of novel sensor arrays and markers 26
4.1.1 Field calculator 26
4.1.2 Principles of designing the sensor arrays 27
4.1.3 Sensitivity analysis 28
4.1.4 Modelling of markers 28
4.1.5 Modelling and calculation of tensor 29
4.1.6 Resonance and RLC circuit 30
4.1.7 Effective magnetic field 32
4.2 Overview of the measurement system 33
5. RESULTS 36
5.1 Results of modelling 36
5.1.1 Sensitivity of coil design 1 36
5.1.2 Sensitivity of coil design 2 39
5.1.3 Sensitivity of coil design 3 40
5.1.4 Sensitivity of coil design 4 41
5.1.5 Comparison of the coil arrays 43
5.1.6 Results of target response simulations 44
5.1.7 Magnetic polarizability tensors of targets 47
5.1.8 Simulation of effective magnetic field 48
5.2 Final design of the experimental setup 49
5.2.1 Transmitting coils 50
5.2.2 Receiving coils 51
5.2.3 Final coil array 52
5.2.4 Electronics 53
5.2.5 Marker 56

5.3 Results of the experiments 58
6. DISCUSSION 67
7. CONCLUSIONS 71
REFERENCES 72
APPENDIX 1: MATLAB CODES FOR FIELD CALCULATOR 77

LIST OF FIGURES

Figure 1. *The principle of wireless capsule endoscopy. Modified from [6]. 4*
Figure 2. *Structure of a wireless capsule endoscope. 5*
Figure 3. *Endoscopic capsules from different manufacturers. [9] 5*
Figure 4. *Conventional endoscope that contains a flexible tube with an imaging module at its end. [12] 6*
Figure 5. *Principle of electromagnetic induction. 18*
Figure 6. *Illustration of the parameters used in the Biot-Savart law for a finite straight wire. 20*
Figure 7. *Magnetic polarizability tensors for different object shapes and conductivities: magnetic rod, magnetic disk, and non-magnetic, conductive disk. Figure based on [50]. 23*
Figure 8. *Simulated three-axial Helmholtz coil array for calculation of magnetic polarizability tensor of ferrite samples. 29*
Figure 9. *Capacitive and inductive reactances as a function of frequency. 31*
Figure 10. *Schematic of the measurement system. 34*
Figure 11. *A picture of the measurement system. 34*
Figure 12. *Geometry of coil design 1 ..... 37*
Figure 13. *Directions of magnetic field produced by a) square-shaped coil and b) a differential coil on a xz-plane orthogonal to the coils. 37*
Figure 14. *Sensitivity maps of coil design 1, on xy-plane at height of 30 cm from the coil array. The components are calculated using the dipole model approximation. 38*
Figure 15. *Geometry of coil design 2 ..... 39*
Figure 16. *Sensitivity maps of coil design 2, on xy-plane at height of 30 cm from the coil array. The components are calculated using the dipole model approximation. 40*
Figure 17. *Geometry of coil design 3 ..... 40*
Figure 18. *Sensitivity maps of coil design 3, on xy-plane at height of 30 cm from the coil array. The components are calculated using the dipole model approximation. 41*
Figure 19. *Geometry of coil design 4 ..... 42*
Figure 20. *Directions of magnetic field produced by a) square-shaped transmitting coil Tx0, and b) square-shaped coil Tx0 with an inner transmitter Tx1 on a xz-plane orthogonal to the coils. 42*
Figure 21. *Sensitivity maps of coil design 4, on xy-plane at height of 30 cm from the coil array. The components are calculated using the dipole model approximation. 43*
Figure 22. *Comparison of different marker types. The marker is positioned on the receiver axis from depth of 10 cm to 30 cm from the coil array. The simulation is done using channel Tx0-Rx5 of coil design 3. ..... 45*
Figure 23. *The effect of resonance. A solenoid target with ferrite core is kept at one position, and the excitation frequency of the transmitter is changed. The simulation is done using channel Tx0-Rx5 of coil design 1. ..... 46*
Figure 24. *Voltage caused by resonated and non-resonated solenoid targets with ferrite core, when the target is swept across a differential receiver coil. The simulation is done using channel Tx0-Rx5 of coil design 1. ..... 46*
Figure 25. *Impedance of the non-differential transmitting coil as a function of frequency. 50*

Figure 26. *Impedance of one of the differential receiving coils as a function of frequency. The measurement frequency 103 kHz is located at the linear region of the impedance graph.* 52
Figure 27. *A schematic of the final coil array and a picture of the constructed system.* 52
Figure 28. *Electronics of the localization system.* 54
Figure 29. *Schematic of the power amplifier (OPA549).* 55
Figure 30. *Schematic of the instrumentation amplifier (INA103).* 56
Figure 31. *A picture of a resonant LC marker, a schematic, and an equivalent circuit of that.* 57
Figure 32. *Visualization of the basic measurements that are taken with the array: a) Positioning the marker further away from the array at certain xy-position and b) Sweeping the marker through a receiving coil at certain distances from the array. At each position, voltage at the receiving coil is measured.* 58
Figure 33. *Depth measurement with differential transmitter Tx2. The marker is moved away from the array at certain xy-position, and the voltage is measured at each point. a) Signals measured at each depth, smoothed by moving average filter, b) Average amplitude of the signal as a function of depth.* 59
Figure 34. *a) Measured and b) simulated voltages caused by a marker that is placed at different positions across a receiving coil at two depths. The marker is oriented along the z-axis.* 61
Figure 35. *a) Measured and b) Simulated voltages caused by a marker that is placed at different positions across a receiving coil at depth of 10 cm. The marker is oriented 45 degrees to x- and y-axes, and 90 degrees to z-axis.* 62
Figure 36. *a) Measured and b) simulated voltages caused by a marker that is placed at different positions across a receiving coil at depth of 10 cm. The marker is oriented along the y-axis, and 90 degrees to z-axis.* 63
Figure 37. *Sensitivity maps of the coil array, on xy-plane at height of 10 cm from the coil array. The components are calculated using the dipole model approximation.* 64
Figure 38. *a) Measured and b) simulated voltages caused by a marker that is placed at different positions across a receiving coil at depth of 10 cm. The marker is oriented along the x-axis, and 90 degrees to z-axis.* 64
Figure 39. *Depth measurement with the non-differential transmitter Tx0. The marker is placed at different depths from the array at certain xy-position, and the voltage is measured at each point. The marker is oriented along the z-axis. a) Signals at depths from 5 cm to 25 cm. b) Enlarged version of the 20 cm and 25 cm signals.* 65
Figure 40. *Measured signals when the non-differential transmitter Tx0 is used. a) Marker is placed at positions across a receiving coil at depths of 10 cm and 20 cm. The marker is aligned with the z-axis. b) Marker is placed at positions across a receiving coil at depth of 10 cm, while it is oriented along x-axis and 90 degrees to z-axis.* 66

LIST OF SYMBOLS AND ABBREVIATIONS

AI	Artificial intelligence
FEM	Finite element method
EM	Electromagnetic
DoA	Direction of arrival
GI	Gastrointestinal
LED	Light-emitting diode
MRI	Magnetic resonance imaging
PET	Positron emission tomography
RF	Radio frequency
RFID	Radio frequency identification
RLC	Resistor-inductor-capacitor circuit
RSSI	Received signal strength identification
Rx	Receiving coil
ToA	Time of Arrival
Tx	Transmitting coil
WEC	Wireless capsule endoscope

$\boldsymbol{A}$	Magnetic vector potential
α	Angle
α_1, α_2	Angles used in Biot-Savart law
$\boldsymbol{B}$	Magnetic flux density
B_0	Flux density of primary magnetic field
C	Capacitance
$\boldsymbol{D}$	Electric displacement field
d	Constant of demagnetizing factor
$\boldsymbol{E}$	Electric field strength
F	Ratio of cylinder's length and diameter
$\boldsymbol{F}$	Forward model
f	Frequency
f_{res}	Resonant frequency
$\boldsymbol{H}$	Magnetic field strength
$\boldsymbol{H_R}$	Magnetic field strength of receiving coil
$\boldsymbol{H_T}$	Magnetic field strength of transmitting coil
$\boldsymbol{H_{eff}}$	Effective magnetic field strength
$\boldsymbol{H_{ex}}$	Exciting magnetic field strength
I	Current
I_R	Current of receiving coil
$\boldsymbol{J}$	Electric current density
$\boldsymbol{k}$	Normal vector of a plane
K	Constant of dipole model
L	Inductance
l_{wire}	Length of a wire
$\boldsymbol{dL}$	Linear segment of current path
$\boldsymbol{L}$	Regularization matrix
λ	Regularization parameter
$\boldsymbol{m}$	Magnetic dipole moment
$\boldsymbol{M}$	Magnetic polarizability tensor
N	Number of turns
N_d	Demagnetizing factor
μ_0	Permeability of vacuum
μ_r	Relative permeability
ω	Angular frequency

$\boldsymbol{P}$	Observation point
ρ	Electric charge density
ρ_{wire}	Conductivity of wire
ϕ	Roll angle
ψ	Yaw angle
$\boldsymbol{R}$	Residual value
$\boldsymbol{r}$	Position vector
r	Distance
$\boldsymbol{S}$	Area of a current loop
$S_{receive}$	Area of receiving coil
S_{wire}	Area of wire's cross-section
θ	Pitch angle
V	Voltage
V_0	Voltage cause by primary magnetic field
V_{ind}	Induced voltage
V_{emf}	Induced voltage at marker
X_L, X_C	Inductive and capacitive reactance
Z	Impedance

1. INTRODUCTION

Wireless capsule endoscopy is a technology that has been in development since the first commercial version of it in 2001 [1]. With its promising technology and many useful properties, it can challenge the conventional endoscopy that is constantly used for visualization of human gastrointestinal tract. For example, in diagnosis of diseases that appear in the small intestine, the wireless capsule endoscope (WEC) technology has become the gold standard method because the conventional endoscopy cannot properly reach all parts of the small intestine. [2,3] In general, WECs can be used to visualize the whole gastrointestinal tract and to diagnose various diseases and disorders, such as celiac disease, Crohn's disease, bleeding or different types of cancer. [3,4]

The WEC technology has also many interesting future prospects. The system could be developed into a totally robotic system with possibilities to steer the capsule from outside the body, take biopsy samples from the tissue of the GI tract and do targeted drug-delivery. [3,4] However, the technology is still in the development phase. In order to achieve all of these interesting applications, one of the main challenges that needs to be overcome is localization of the capsule during the procedure. This would also help to accurately localize tumours and other critical findings. [2,3]

The aim of this thesis is to design an electromagnetic coil array system that could be utilized in localization of WECs. Since the WEC technology is constantly developing towards a robotic system that could apply a steering module above the patient's body to modify the orientation and position of the capsule, the aim is to design a system that could be fitted inside a hospital bed, and therefore leave space for the steering module. The localization method is selected based on a literature review, after which several planar localization arrays are designed. The optimal design is selected based on computational modelling and sensitivity analysis of the arrays. Also, the optimal target type to embed into the capsule endoscope is selected by means of finite element method- based modelling and literature. After finding the optimal array and target type, the system is constructed and tested experimentally. Based on measurements taken by the system in different positions and orientations, the possibility to use the system for localization purposes is analysed.

The thesis is structured as follows. In Chapter 2, background of WEC technology is went through, and its advantages and challenges are presented. In addition, the current methods for localization of the capsules are studied based on literature review, and the most optimal method is selected. In Chapter 3, the theories of physics needed in the modelling and measurements of the thesis are presented. Next, methods of both modelling and experiments are introduced in Chapter 4. As four sensor arrays and multiple different marker types are studied to find the optimal ones for practical study, the principles of designing the arrays, sensitivity analysis and target response simulations are presented. In addition, overview of the experimental setup is shown in Chapter 4. In Chapter 5, results of the simulations and experiments are presented and analysed. Based on results of the sensitivity analysis and target response simulations, the selected coil array and marker are built and tested in real life. After presenting the properties of the coil array, markers and electronics, functionality of the system is tested and results of the measurements are compared with modelled values. In Chapter 6, the results and future prospects of the system are discussed. Finally, Chapter 7 concludes findings of the thesis.

2. BACKGROUND OF WIRELESS CAPSULE ENDOSCOPE LOCALIZATION

Wireless capsule endoscope (WEC) is a small, swallowable device that can be used to examine mucosa of gastrointestinal (GI) tract and to diagnose many diseases that appear there. [2] The conventional endoscopy with a rigid tube is currently the primary method to inspect the GI tract but because of their many advantages and future prospects, WECs are becoming more popular. This section presents the principle of using WECs, and their advantages and challenges. In addition, different methods that have been studied in solving the localization challenge are introduced and compared.

2.1 Wireless capsule endoscopy

Wireless capsule endoscopy has many applications in diagnosis of different GI tract diseases. Nowadays, there are different versions of the capsule to be used for different parts of the GI tract. For example, the capsule designed for visualizing the small intestine has become the gold standard method for visualization of that area of GI tract, since the small intestine is rather difficult to reach with the conventional endoscope with wire. [2,5] Next, the general procedure of using WECs is presented.

2.1.1 Principle and structure of WEC

The first capsule endoscope was developed in 2001 by Given Imaging Ltd [1]. It is a small device, approximately in size of 30 mm in length and 13 mm in diameter. It is shaped like a capsule so that the patient can swallow the device after which it travels through the whole GI tract with the help of natural peristaltic contractions. [2] In Figure 1, the principle of WEC procedure is presented.

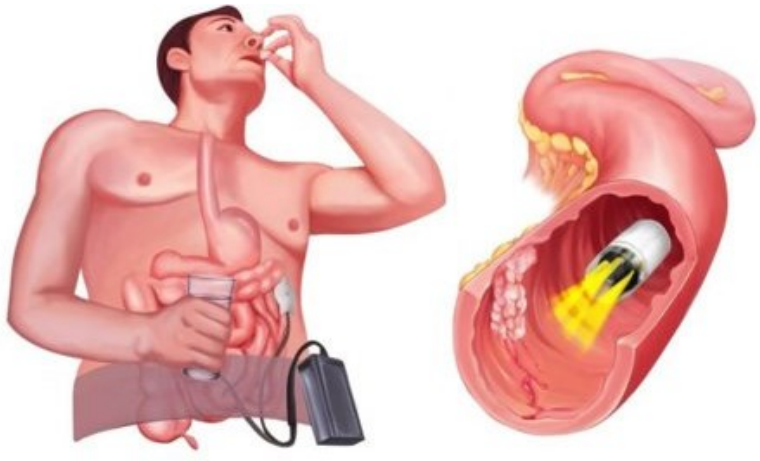

Figure 1. *The principle of wireless capsule endoscopy. Modified from [6].*

The structure of WEC is as follows. The device is coated with polycarbonate that is biologically compatible, and one end of the capsule is left transparent to enable the imaging. The capsule contains an imaging sensor surrounded by light-emitting diodes (LEDs) that are used for illuminating the GI tract mucosa. In addition, the device includes coin batteries for power supply and an antenna unit for radio frequency (RF) transmission. The gathered data is sent from the RF transmitter to receiving unit outside the patient's body. Thus, the images from the GI tract can be visualized on computer screen. After the capsule has exit the body, patient returns the receiving unit to the hospital where that the data can be gone through. [3,7] Some systems contain also a recorder device connected to the sensor belt that can be applied to view the gathered images in real time while the capsule passes the body. [8] The basic structure of WEC is presented in Figure 2, and the receiving belt can be seen from Figure 1.

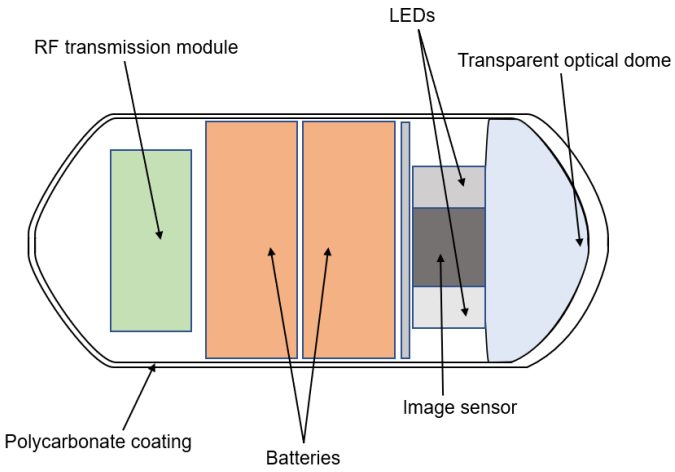

Figure 2. *Structure of a wireless capsule endoscope.*

Nowadays, the capsule may contain additional structures that are utilized in localization, active locomotion, or wireless powering of the device. These can be, for example, different sensors or electromagnetic coils. In addition, the system may have additional structures outside the patient's body, such as magnetic sensor arrays, electromagnetic coils or robot manipulators. [3] The system may include multiple cameras that are facing different directions to provide wider viewing angle or a panoramic view. For example, some WECs contain two imaging units at both ends of the capsule, or four cameras that are perpendicular to each other. [3,4] In Figure 3, different endoscopic capsules available on market are presented.

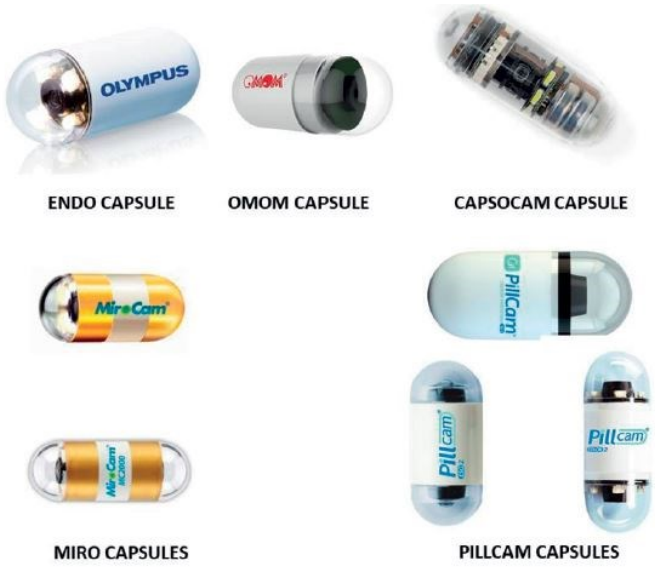

Figure 3. *Endoscopic capsules from different manufacturers. [9]*

As can be seen from Figure 3, the capsule camera may contain multiple imaging units which affect the viewing angle. In addition, the devices provide different frame rate, battery life and depth of view. Variations of the technology make different capsules optimal for different parts of the GI tract. For example, there are capsules that are especially designed for the small intestine, colon, or diagnosis of Crohn's disease. [8,9]

2.1.2 Advantages of WECs

WECs have many advantages compared to conventional endoscopes. Since the conventional endoscope contains a tube that is fed though the GI tract, the procedure may be uncomfortable and even painful for the patient. The conventional setup is presented in Figure 4. The main disadvantage of conventional endoscopy is that it cannot be used to screen the small intestine totally [3]. In addition, the procedure may cause gastroin-

testinal perforation or cross-contamination [10]. WECs overcome these limitations by allowing the imaging of the whole GI tract with reduced discomfort. In addition, the WEC procedure does not require use of sedatives which are usually needed for the conventional endoscopy. [7,11] Additionally to the image gathering, the WEC system is usually capable of measuring pH, temperature, and pressure in the GI tract [7].

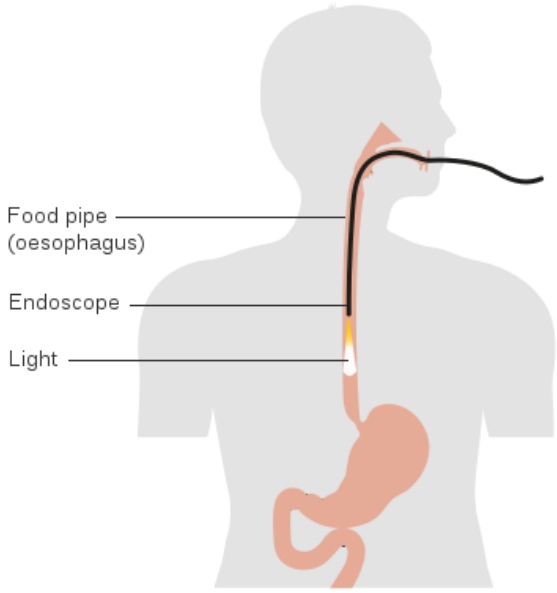

Figure 4. *Conventional endoscope that contains a flexible tube with an imaging module at its end. [12]*

Since WECs can be used to screen the whole GI tract, they have become an important diagnosing method for different diseases that appear in the small intestine. For example, the system can be used to detect celiac disease, Chron's disease, bleeding, inflammatory bowel disease or different cancers. [4,7] In diagnosis of Chron's disease, capsule endoscopy performs better than the conventional endoscopy or other radiological methods [13].

WECs have many interesting future prospects. The system can be possibly applied to take biopsies from the intestine, or to deliver drugs while travelling through the GI tract. In addition, long-term monitoring of the GI tract may be possible in the future. [4,14]

2.1.3 Challenges of WECs

There are still some challenges that need to be studied further to make the WEC system perform better in treatment and diagnostic purposes. One challenge is that the capsule movement cannot be controlled from outside the body. This causes problems if the capsule gets caught in the bowel since it usually cannot be released without a surgical operation. Capsule locomotion system is also needed to modify orientation of the capsule

so that critical parts of the GI tract are not missed by the imaging module. [4,15] In addition, the lack of control of movement and orientation makes screening the upper GI tract challenging. Speed of the capsule is quite high when it transits the esophagus which imposes requirements for the imaging rate and orientation of the imaging sensors. Also, since human stomach is a voluminous organ, it is hard to get the whole stomach imaged with the capsule if it is moved by the natural activity of the GI tract. [4] The movement control system could as well be useful in shortening the time that is required for the procedure. By natural peristalsis, the required time for the WEC to exit the body is about 8 hours. [16] Most of the current capsule endoscopes available on the market have battery life of 8 – 12 hours which limits the time during which the capsule has to pass the GI tract. [9]

Capsule endoscopy usually requires bowel preparation before the procedure. Patient needs to fast and take laxative medicine, and in some cases, antifoaming agents are used to further improve the visibility in the bowel. However, the need for bowel preparation is under research since benefits of the preparation have been debated. [4,17,18] Improving the visibility in the bowel has also been examined by using multiple cameras in the capsule, for example, two or four of them, and using adaptive frame rate and light control. The adaptive frame rate is useful as the speed of the capsule changes when it travels through different parts of the GI tract. Since the limited battery power is one challenge of WECs, the adaptive frame rate helps in saving the battery power when the capsule is moving slowly. [4]

Capsule retention, that is, when the capsule gets caught in the bowel and does not exit in two weeks after the procedure, requires using either surgery or conventional endoscopy to remove the capsule from the body because the stuck capsule can cause obstruction or ulceration in the small intestine. Nowadays, a lactose-body patency capsule is typically used for high-risk groups before the WEC procedure to examine if the small intestine is too narrow to be imaged with the WEC system. [4]

Interpreting the results from the images gathered from the GI tract requires expertise from the physician. Especially, the system that produces panoramic images can be challenging to interpret. In addition, the image quality could still be improved to make evaluation of the images easier and more efficient. Technologies that utilize artificial intelligence (AI) in feature extraction and image classification will probably make the process easier in the future. [4] For now, AI has been studied in detection of polyps, bleeding and

Celiac disease, and it has shown promising results with high sensitivity and distinct decrease in time needed for the analysis. However, further study is needed to embed the detection system into the capsule software. [19,20]

Capsule localization is one of the main challenges of the system. To develop the movement controlling system, capsule's location and orientation should be known with high accuracy. In addition, localization is needed in detection of tumours and other critical findings in the GI tract. An accurate localization system will help in removing the capsule from the body if it gets caught, and to save the battery power by turning off the device in areas of no clinical interest. In addition, localization system may be utilized in wireless powering of the capsule. To achieve the future prospects of the WECs, such as targeted drug-delivery, biopsy or long-term imaging, localization of the capsule is crucial. [3] Advantages and challenges of WECs are concluded in Table 1. Since the localization problem affects also many other challenges and future prospects of the system, the localization problem is studied in this work, and one method for that is chosen to be tested.

Table 1. *Advantages and challenges of WECs.*

Advantages	• Possibility to screen the whole GI tract • Reduced discomfort • No need to use sedatives • Future prospects: targeted drug-delivery, biopsy, continuous monitoring
Challenges	• Localization • Controlling the capsule movement and orientation • Battery power, wireless charging • Capsule retention • Image quality, expertise needed in interpreting the results

2.2 Methods for localization of WECs

Several different methods have been studied and tested in localization of capsule endoscopes. Two most studied categories are electromagnetic wave -based methods and magnetic field strength -based methods. Other methods, such as radiological methods, or hybrid methods that combine at least two different techniques, have also been investigated. In this section, different techniques for WEC localization are presented and compared to select the optimal one for modelling and practical study.

2.2.1 Electromagnetic wave -based localization methods

Electromagnetic (EM) wave -based localization methods can be divided into radio frequency (RF) -based methods and visible waves -based methods. One challenge that the EM-based localization methods face is the attenuation of the fields in human body. The attenuation is higher than with the magnetic field strength -based techniques and causes the localization to have lower accuracy. [7,21] In addition, it is challenging to model how the electromagnetic waves propagate through the tissues because the attenuation is dependent on, for example, the operating frequency and the part of the GI tract to be imaged. [3,22]

The RF-based methods can either utilize the RF-module that is already used for image transmission, or have an additional array for the localization. [3] Methods that do not require additional equipment, are radio frequency identification (RFID)- and received signal strength (RSSI)- based methods. [3] The RFID-based method usually utilizes a transmitting tag inside the capsule and an antenna array around the body, and it is based on detecting the capsule with the closest antennas. [7] The RSSI-based system measures the power of the received signal with the antenna array around the patient's body. Typically, a signal propagation model is utilized to improve accuracy of the localization. For example, in study by Ye et al. [23], the group used a three-dimensional model of the dielectric properties of human tissues and an RSSI-based system to reach position detection error of 45 mm. As comparison, Li et al. [24] reached mean detection error of 80 mm with the RSSI-based localization and a maximum likelihood algorithm.

There are also many examples of studies using RFID technology in localization of biomedical devices. For example, in study by Wille et al. in 2011 [25], they reached accuracy of 2 mm when studying six datasets using support vector regression to solve the location. However, the tag orientation was not studied, and environmental variations were not taken into account. Also, in 2009, Hou et al. [26] used RFID to localize a WEC. The method they were using was based on the ultra-high frequency band (915 MHz) to avoid the use of complicated propagation models of the RF-signals in human body. They were able to reach accuracy of 20 mm with their system.

In addition to RFID- and RSSI-based technologies, there are time of arrival (ToA)- and direction of arrival (DoA)- based methods that have been studied in detection of WECs. The ToA-technology is based on measuring the time difference between transmission and receiving of the RF-signal when the capsule is used as a reflector, and the DoA-method is based on detecting from which direction the waves are propagating with an array of antennas. [3] On average, the aforementioned RFID- or RSSI- based methods

reach detection error approximately of 20 mm to 50 mm, and the ToA- and DoA- based methods from 10 mm to 15 mm. However, the need for additional equipment make ToA- and DoA- based methods more complicated to implement. [3] For example, in study by Khan et al. [27], they compared ToA-based and RSSI-based localization methods, and the detection error for ToA appeared to be 2.5–35 mm, whereas the detection error for RSSI was 10–55 mm. In addition, Nafchi et al. [28] developed a system that could be used both for DoA- and ToA-based localization. With the help of inertial measurement unit and extended Kalman filter, the localization error reached was 10 mm.

Visible waves -based localization methods normally utilize the camera system of the capsule. The localization is done with respect to the surrounding anatomy rather than with respect to an external coordinate system. Usually, a computer vision system with artificial intelligence (AI) is utilized in this type of localization. In addition, the system can contain automatic detection of, for example, polyps in the GI tract. [3] For instance, in study by Boa et al. in 2014 [29], the group used real endoscopic images to calculate the speed in which the capsule is travelling through the bowel. This was done by studying the consecutive images and finding the corresponding feature points from them. When the capsule speed was known, it was possible to solve the distance travelled from certain anatomical point. In the study, the accuracy reached in calculation of the distance was 27 mm.

In [30], a hybrid method combining RF-based localization and optical localization was presented. They used feature point matching for the detection of speed of the capsule, and RSS-based localization to get the location in reference to an external sensor array. Accuracy of the total hybrid localization was 23 mm, when the accuracy reached only with the RF-based localization was 68 mm. However, they claim that by improving the algorithm used, the error level could be lowered. The advantage of this method is that equipment for both localization methods is already found in the WEC system.

2.2.2 Magnetic field strength -based localization methods

Magnetic field strength -methods are based on measuring the magnetic field either by electromagnetic coils or an array of sensors. The systems that utilize electromagnetic coils are called *active* magnetic field strength -based methods, while the systems that use a permanent magnet and array of sensors are called *passive* methods. Sensors that are used to measure the magnetic field in passive localization can be, for example, Hall-effect sensors or magneto-resistive sensors. In addition, the magnetic localization system may be equipped with a magnetic actuation system that is used for controlling the capsule movement. The localization system may be either having an external magnetic

source and sensing element inside the capsule, or utilize external sensors or coil array to receive the field. [3]

The main advantage of using magnetic field strength -based techniques is the ability of magnetic fields to pass the human body without high attenuation because the relative permeability of human tissues is near to the one of air. [7,21] However, the system can be affected by external magnetic fields, like the Earth's magnetic field or fields caused by magnetic objects in the operating room. This causes also a challenge in development of the combined localization and movement control systems since the actuating magnetic field may cause interference in the localization process. [3,7,21]

Active and passive magnetic field strength -based localization techniques can also be compared. A permanent magnet embedded in the capsule generates rather weak magnetic field to be measured which can cause problems when the capsule is travelling far away from the sensor array [31]. For example, in passive method by Son et al., the detected distance where the localization was still effective was only 50 mm [32]. This problem is usually overcome by the use of active magnetic localization, since the fields generated are stronger [31].

As said, the passive magnetic localization methods utilize a permanent magnet and array of sensors for localizing the capsule. For example, in study by Hu et al. in 2010, the group developed a system with permanent magnet inside the capsule and array of sensors around the body that measured the magnetic field caused by the magnet. They were able to solve the capsule position and angle of orientation with accuracy of 1.8 mm and 1.6 degrees [33]. In [34], the same group studied further the use of the system as a wearable array around the body by developing a body movement compensating system. The error reached with the system was 3.82 mm in average. A similar wearable system was developed by Shao et al. in 2019 [35]. One advantage of their system was the possibility of the patient to move around when wearing the array. In addition, in their study, they developed a system that cancels the noise caused by the geomagnetic fields. By doing that, they were able to reach position error of 10 mm and orientation error of 12 degrees.

Another example of passive localization can be found by Natali et al. [36,37], in which the group utilized a slightly different approach where the pose tracking sensors were placed inside the capsule. Hall effect sensors and an accelerometer were used to estimate both the position and orientation of the capsule in reference to an external magnet. The system was developed with intention to be operated together with an actuation system. The reached detection error was below 7 mm for the position of the capsule. Also,

in study by Xu et al. [38], a passive localization system with an array of sensors outside the body and permanent magnet inside the capsule was developed with aim of being used with an actuation system. Since the sensors inside the capsule take space and increase the weight of the capsule, the external sensor array was preferred in their system. With the system that measures the fields caused by the marker and the rotating actuator magnet together, the accuracy achieved was 5.5 mm for position and 5.2 degrees for orientation.

In paper by Taddese et al. [39], a hybrid localization system contained both permanent magnet and electromagnetic coil, in order to produce a field without singularity points, since the magnet and coil were placed perpendicular to each other. Singularity is a problem in any localization system that uses only one excitation source, either magnet or coil. The system was based on papers by Natali et al. [36,37], and with their added coil system, the reached error levels were 5 mm and 6 degrees.

As stated, the active magnetic methods use electromagnetic coils for localization of the capsule. In studies by Hashi et al. [40], localization was based on having transmitting and receiving electromagnetic coils around the patient, and a resonated LC marker with ferrite core as the object to be localized. By measuring the voltage induced to the receiving coil by the marker, they were able to resolve the location with accuracy of 3.8 mm at maximum distance of 200 mm from the receiving array. They also studied optimization of the size of the receiver coils and the marker, and the number of transmitting coils. It was found that the optimum size of the receiver coil is dependent on the marker size [41,42], and that using multiple excitation coils allows exciting the marker in each orientation which is not possible with single transmitting coil [43]. Another example of active magnetic localization is a study by Shao et al. 2020 [16] in which they studied both localization and charging of the capsule with electromagnetic coils. With two coils forming a Helmholtz coil pair, and with the use of in-phase and out-phase excitation, it was possible to combine these two actions by having a receiving coil inside the capsule. Accuracy of the position detection was 1.57 mm, although the system was designed only for 1 dimensional localization. In order to reach 3D localization, the system should contain several transmitting coils in multiple directions. [16]

The active method can also be constructed by having an array of transmitting coils outside the capsule and receiving coil that is built in the capsule, as in study by Liu et al. in 2020 [31]. They reached accuracy of 2.18 mm. However, they assumed that the capsule orientation can be controlled by the actuation system and is therefore known beforehand. In addition, the coil embedded in the capsule was connected to the voltage measurement

system with wires, which is not possible in the actual application. Similar localization approach was utilized in paper by Guo et al. in 2022 [44]. They utilized excitation coils outside the body and a receiver coil inside the capsule. The method was based on exciting multiple external transmitting coils at the same time with different frequencies and receiving the signal with a capsule-mounted receiver coil that converts the signal into electrical form, containing the information about the frequency. However, the mean detection error of the system was only 17 mm.

Several companies have also investigated the use of active magnetic localization with capsule endoscopes. For example, both Olympus and Siemens AG have studied the use of electromagnetic coil array around the body, and either a resonant circuit or a coil inside the capsule to perform both localization and steering simultaneously with slightly different approaches. [45,46] Also, similar technology is used in commercial Aurora tracking system. It utilizes external coils as transmitters and a small coil inside a capsule endoscope, catheter or guidewire to receive the fields. The technology is based on studies by Plotkin et al. [47,48] In addition, similar method has been utilized in other types of detectors, for example, for walk-through metal detectors at airports or other public places, or as handheld metal detectors for searching of metallic objects underground or under water [49,50].

2.2.3 Other localization methods

There are also many other approaches that have been studied in localization of biomedical devices, such as catheters. Some of the methods could also be utilized with WECs, but in some cases, the compatibility with the actuation system might be problematic. However, there are some examples where the methods have been tested with WECs. Possible technologies are, for example, ultrasound, X-rays, or magnetic resonance imaging (MRI) [3].

For example, in study by Carpi et al. [51], the group tested a fluoroscopy-based system for WEC localization. The tests were done with pig intestine. They reported accuracy of 1 mm in the three-dimensional localization with the X-rays. However, they proposed that the localization system could be combined with an RF-based triangular localization to lower the X-ray dose received by the patient. In addition, as the capsule contains metallic components, the localization could be done with lowered radiation level. [51]

Ultrasound can be applied to WEC localization either by using the capsule itself as a reflector and measuring the ToA of the transmitted ultrasound pulse [52], or by attaching an ultrasound transducer to the capsule and receiving the signal with external detectors

[53]. The method in which the transducer is connected to the capsule provides larger signal-to-noise ratio and better detection of the device located, but integrating such component to WEC is challenging because of the high voltage needed for driving the component [3].

In addition, positron emission tomography (PET) has been applied in localization of WECs in paper by Than et al. [54]. In the study, the capsule contained three positron emitters within its case, and the patient was surrounded by gamma ray detectors. They tested two commercial PET scanners in the localization process and reached accuracy of 0.5 mm and 2.4 degrees which is superior compared to many other methods. The marker does not require almost any space from the capsule and does not increase the power consumption of the capsule as some other methods do. In addition, the system would not be affected by an actuation system. However, the method requires the use of radioactive materials which causes exposure for the patient and requires expert labour. In addition, a PET scanner is an expensive equipment to operate which further limits the possibility to use this method for localization. [54]

In paper by Karargyris et al. in 2015 [55], a different approach to localization was presented. They developed a capsule with three legs around the capsule sides. A small wheel was connected to each of the legs, and these wheels acted as small odometers that detected the rotation. From the data gathered by the odometers, the distance travelled by the capsule could be calculated. The group tested the system with a porcine intestine. There were some problems with some of the wheels getting stuck or with the wheels rotating in different pace. Therefore, the system needs further validation before it can be used in localization accurately. [55]

2.2.4 Comparison of different localization methods

Table 2 combines all the different types of WEC localization. In the table, the principle of operation for each method is presented, and advantages and challenges for each localization category are compared.

Table 2. *Comparison of different methods for localization of WECs.*

Localization method		Advantages	Challenges
Electro-magnetic wave -based methods	**RSSI**: Measuring power of the received RF-signal with an external antenna array [23,24,27]	• No need for additional equipment • Not affected by actuating magnetic field • Accuracy of 20-50 mm for RFID- and RSSI- systems • Accuracy of 10-15 mm for ToA- and DoA- systems	• High attenuation of the electromagnetic fields in human tissues • Modelling the propagation of electromagnetic waves through human body
	RFID: Detecting a RFID-tag placed inside the capsule with the closest antennas [25,26]		
	ToA: Measuring the time difference of transmitted and received RF-signals with an antenna array [27,28]		
	DoA: Detecting from which direction the RF-waves are propagating with an antenna array [28]		
	Optical: Localization with respect to surrounding anatomy with the camera module of the WEC system [29]		
Magnetic field strength -based methods	**Passive**: Measuring the magnetic field strength produced by a permanent magnet with a sensor array [32–38]	• Low attenuation of magnetic fields in human body • Possibility to use the system for steering and charging of the capsule • Accuracy of 2-10 mm	• Interfering magnetic fields (Earth, magnetic materials) • Possible conflicts between steering and localization systems • Similar technology already used in commercial applications (capsule endoscopes, catheters, metal detection)
	Active: Measuring the induced voltage caused by a marker with an electromagnetic coil array [16,31,40–44]		
Hybrid methods	Combination of e.g., RF- and optical localization, RF- and magnetic localization, or active and passive magnetic localization [30,39]	• Increased accuracy compared to individual method	• More complex system • Cooperation of the systems
Other methods	Localization with an imaging method (X-rays, ultrasound, MRI, PET) or e.g., by mechanical legs of the capsule [51–55]	• High accuracy (even submillimeter level)	• Use of ionizing radiation • Expensive equipment

As can be seen from Table 2, each method has their advantages and challenges. However, the magnetic field strength -based method with an active electromagnetic array seems to be the most promising one, by means of providing high accuracy and possibility to utilize the system for active locomotion of the capsule. Therefore, it is selected for further study.

2.3 Motivation of the Thesis

Based on the literature review, wireless capsule endoscopes are about to become the gold standard method in visualizing the mucosa of different GI tract parts and replace the conventional endoscopic methods. However, there are still many challenges in the WEC technology, such as the localization and active steering of the capsule. As noticed, multiple different technologies have been tested for the localization purpose but none of them has become a standard method that would be superior compared to the other ones. The magnetic field strength -based method with an active electromagnetic coil array seems to be the most promising one.

However, most of the active magnetic field strength -based localization arrays developed by research groups utilize either a double-sided array or even coils in many different directions. For example, in studies by Hashi et al., where the group was utilizing the active magnetic field strength method, each of their prototypes consisted of coils on two sides of the patient separated by 20–41 cm [40,42,43]. These kind of arrays around the body increase the sensitivity of the localization system, as was found in the conference article written as a part of the thesis [56]. Even if they can be used for regular body sizes, it is appealing to develop a planar, thin system that could effectively perform the localization and could be fitted inside or under the hospital bed where the patient is laying. This is because the active steering system, which is one of the main future prospects of capsule endoscopy, will most probably contain a large module above the patient's body. Hence, a planar localization system would save space for operation of the steering module and provide a fixed coordinate system for both localization and steering of the capsule. Also, this would leave space for the medical staff to carry out their work, and to be able to, for example, modify the posture of the patient easier if needed. Naturally, the system should be able to operate at tens of centimeters from the array, and provide high accuracy in the localization.

3. THEORETICAL BACKGROUND

Localization that is based on electromagnetic tomography includes two parts: forward and inverse problem. The forward problem is the process of measuring or simulating the response given by the system at different positions. On contrast, the inverse problem takes the measured value as an input and estimates the parameters that are needed to get this response. In this work, the forward problem is addressed in more detail by means of electromagnetic induction, and the fundamentals of inverse problem are presented.

3.1 Electromagnetic induction

This section describes the theoretical background for the technology utilized in the thesis. The used localization method can be categorized as an active magnetic field strength -based method, in which the basic principle is electromagnetic induction. At first, the Faraday's law of induction is introduced among other Maxwell equations, and the principle of using electromagnetic induction in a localization system is presented. Next, the Biot-Savart law and its use in calculation of magnetic fields is discussed. As the magnetic dipole approximation is utilized in the localization system, the theoretical basis of magnetic dipole moment and magnetic polarizability tensor are gone through.

3.1.1 Faraday's law of induction

Electromagnetic fields can be described and analysed with a set of four Maxwell equations. They consist of Gauss' Law, Gauss' Law for magnetism, Faraday's Law of induction and Ampere's Circuital Law. The equations are presented as

- Gauss' law: $\nabla \cdot \overline{\boldsymbol{D}} = \rho$ (1)
- Gauss' Law for magnetism: $\nabla \cdot \overline{\boldsymbol{B}} = 0$ (2)
- Faraday's Law of induction: $\nabla \times \overline{\boldsymbol{E}} = -\frac{\partial \overline{\boldsymbol{B}}}{\partial t}$ (3)
- Ampere's Circuital Law: $\nabla \times \overline{\boldsymbol{H}} = \bar{\boldsymbol{J}} + \frac{\partial \overline{\boldsymbol{D}}}{\partial t}$ (4)

where $\boldsymbol{D}$ is the electric displacement field, ρ is the electric charge density, $\boldsymbol{B}$ is the magnetic flux density, $\boldsymbol{E}$ is the electric field strength, $\boldsymbol{H}$ is the magnetic field strength and $\boldsymbol{J}$ is the electric current density [57].

Faraday's Law can be used to describe the phenomenon of a magnetic field being also a cause of an electrical field. The localization system in this thesis is based on electromagnetic induction, which can be explained by the theory of a time-varying magnetic flux generating a voltage in a closed loop. Transmitting and receiving coils are utilized in the localization process. This is illustrated in Figure 5. Current in the transmitting coil *Tx* produces a primary magnetic field B_0. This primary field induces a varying voltage V_0 in the receiving electromagnetic coil *Rx*. When no target is placed in the localization volume, the primary field is the only one coupling to the receiving coil and the induced voltage measured is caused only by that field. [43]

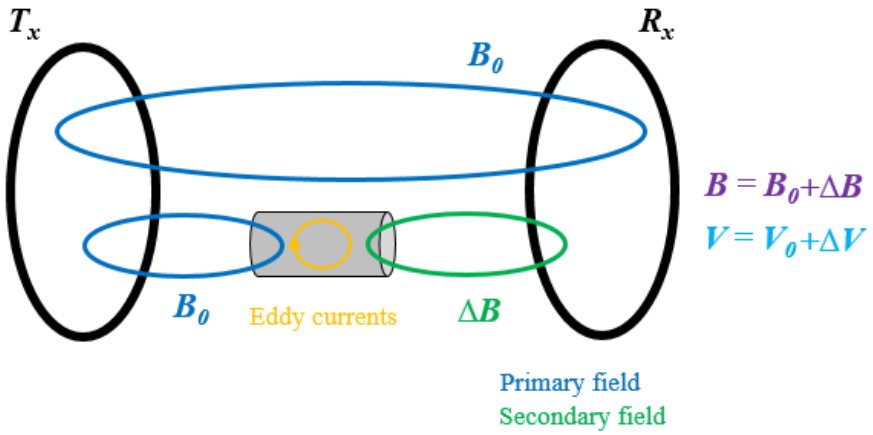

Figure 5. *Principle of electromagnetic induction.*

In general, induced voltage V_{ind} in the receiving coil can be calculated as

$$V_{ind} = \oint_C \bar{\boldsymbol{E}} \cdot \boldsymbol{d\bar{L}}, \tag{5}$$

which is a line integral of the electric field strength along the coil boundary, where ***dL*** is a linear segment of the boundary. [58] When a target, for instance, a ferrite or metal sample or a solenoid, is placed in the target volume of the electromagnetic coil array, the primary magnetic field B_0 produces Eddy currents in the target. These Eddy currents further generate a secondary magnetic field ΔB around the target, which also induces a voltage in the receiving coil. [50] Thus, the total measured voltage in the receiving coil contains both the primary and secondary field components, that is, $V = V_0 + \Delta V$. As the field caused by the target is of interest, it is calculated by vectorially subtracting voltage caused by the primary field from the total voltage. Since the coil array usually consists of multiple coils, this calculation is done for an array of receiving coils to produce a set of

measurements. Hence, the technology used can be seen as electromagnetic tomography, where the target volume is scanned by the system, and an inversion algorithm is used to solve the target location based on the data set. [43,50]

3.1.2 Biot-Savart law

In order to calculate the magnetic field caused by an electromagnetic coil, Biot-Savart law needs to be presented. It is a specific form of Ampere's law, and it can be only applied in free space. It can be presented as follows

$$\bar{\boldsymbol{H}} = \frac{I}{4\pi}\oint \frac{d\bar{\boldsymbol{L}} \times \hat{\boldsymbol{r}}}{r^2} \tag{6}$$

where *I* is a constant electric current, ***dL*** is a vector along the path of the current, and ***r*** is a vector between the conductor element and point ***P*** where the field is calculated. [50] It is possible to utilize the Maxwell equations in calculation of the fields, but as the use of Biot-Savart law simplifies the calculation and reduces the computational power needed, the approximations needed for its use are made. Therefore, it is assumed that the localization coils are filamentary, and that the system exists in vacuum. It is possible to compare the results of Biot-Savart law, for example, with finite element calculation to verify that the results match. [50]

The Biot-Savart law can be used to calculate fields caused by, for example, a straight wire or a circular wire loop. For a finite length straight wire, the law is in form

$$\bar{\boldsymbol{H}} = \frac{I}{4\pi r}(sin\alpha_2 - sin\alpha_1)\hat{\boldsymbol{k}} \tag{7}$$

where α_1 and α_2 are the angles between point ***P*** and points P_1 and P_2, shown in Figure 6, *r* is the Euclidean distance between the observation point ***P*** and the infinitely long line formed along conductor ***dL***, and ***k*** is a vector perpendicular to the plane formed by the observation point ***P*** and the conductor ***dL***. [50]

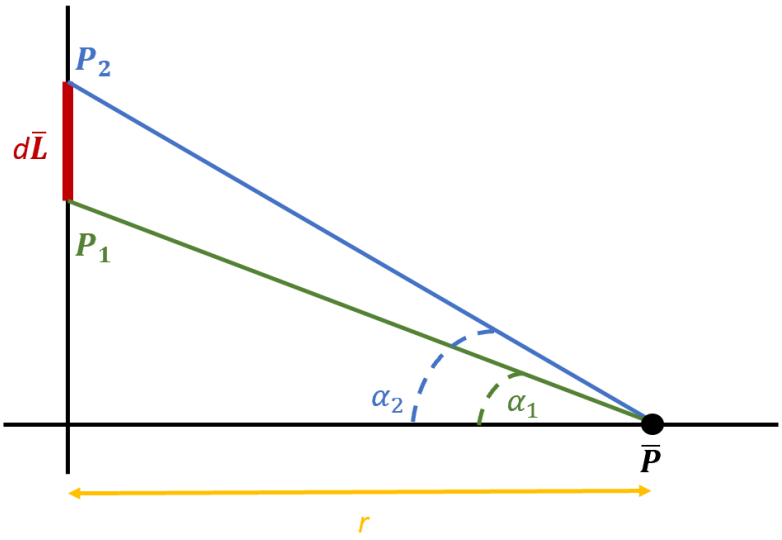

Figure 6. *Illustration of the parameters used in the Biot-Savart law for a finite straight wire.*

The Biot-Savart law for straight line elements can be also utilized in calculation of fields produced by circular coils since they can be constructed from multiple short linear elements. [50,59]

3.1.3 Magnetic dipole moment

Magnetic dipole is a useful quantity in electromagnetic induction. It is commonly applied to describe the magnetic field caused by the Eddy currents in a small metal object that usually is the target. In the theory, the secondary magnetic field caused by the target can be seen similar to the one caused by a small current loop. Magnetic dipole moment of a loop can be defined as

$$\boldsymbol{m} = \frac{1}{2}\int_S \bar{\boldsymbol{r}} \times \bar{\boldsymbol{J}}\, d\bar{\boldsymbol{S}} \tag{8}$$

where ***r*** is the position vector, ***J*** is the current density and ***S*** is the area of the loop. When the current loop is on a plane, the calculated magnetic dipole moment is based on the integral:

$$\boldsymbol{m} = \boldsymbol{S}I \tag{9}$$

where *I* is the current flowing in the loop. The magnetic vector potential ***A*** produced by this dipole moment can be expressed as

$$\bar{\boldsymbol{A}} = \frac{\mu_0}{4\pi}\frac{\boldsymbol{m} \times \bar{\boldsymbol{r}}}{r^2} \tag{10}$$

where μ_0 is permeability of vacuum. [50] Now, it is possible to define the magnetic flux density ***B*** as a function of the magnetic vector potential

$$\bar{\boldsymbol{B}} = \nabla \times \bar{\boldsymbol{A}} \tag{11}$$

By combining the Faraday's law of induction and equation (11) together, it is possible to reformulate the induced voltage as

$$V_{ind} = -\oint_C \frac{\partial \bar{\boldsymbol{A}}}{\partial \mathrm{t}} \cdot d\bar{\boldsymbol{L}} = -\oint_C \mathrm{j}\omega \bar{\boldsymbol{A}} \cdot d\bar{\boldsymbol{L}} \tag{12}$$

where ω is the angular frequency. [50] When equation (10) is placed into equation of the induced voltage (12), the voltage becomes

$$V_{ind} = -\mathrm{j}\omega \oint_C \frac{\mu_0}{4\pi} \frac{\boldsymbol{m} \times \bar{\boldsymbol{r}}}{r^2} \cdot d\bar{\boldsymbol{L}} \approx \frac{j\omega\mu_0}{4\pi} \frac{\boldsymbol{m} \cdot (\overline{\boldsymbol{r} \times d\bar{\boldsymbol{L}}})}{r^2} \tag{13}$$

Now, it is possible to calculate the induced voltage in the receiving coil when the target object is treated as a magnetic dipole. [50]

3.1.4 Magnetic polarizability tensor

When the target is significantly smaller than the size of the localization coil array, the dipole model approximation can be utilized. To use the approximation, an assumption is made that the primary magnetic field is uniform across the target's volume. This requires that the longest dimension of the object, *a,* needs to fulfil the equation $a^3 << r^3$ where *r* is the distance from the target object to the coil array. In addition, secondary field produced by the target is supposed to be similar to one of a magnetic dipole. Based on equation (13) and the Biot-Savart law, when the dipole approximation is used, the induced voltage in the receiving coil can be expressed as

$$V_{ind} \approx K\overrightarrow{\boldsymbol{m}} \cdot \overrightarrow{\boldsymbol{H_R}} \tag{14}$$

where $\boldsymbol{m}$ is the magnetic dipole moment and $\boldsymbol{H_R}$ is the magnetic field strength of the receiver coil. [50] The constant *K* in the equation is

$$K = \frac{j\omega\mu_0}{I_R} \tag{15}$$

where I_R is current of the receiving coil [50]. The magnetic dipole moment can be also calculated by dot product of a magnetic polarizability tensor $\boldsymbol{M}$ and magnetic field strength of the transmitting coil $\boldsymbol{H_T}$. By this modification, the induced voltage becomes [50]

$$V_{ind} = K\overleftrightarrow{\boldsymbol{M}} \cdot \overrightarrow{\boldsymbol{H_T}} \cdot \overrightarrow{\boldsymbol{H_R}} \tag{16}$$

Magnetic polarizability tensor $\boldsymbol{M}$ is a complex, frequency-dependent, two-dimensional 3x3 matrix. It is an important quantity in magnetic induction applications because it contains information about properties of the marker. It can be used to characterize object's size, shape and its material properties, for example, conductivity and permeability. [50,60] The magnetic polarizability tensor is expressed as [50]

$$\overleftrightarrow{\boldsymbol{M}} = \begin{bmatrix} M_{11} + jN_{11} & M_{12} + jN_{12} & M_{13} + jN_{13} \\ M_{21} + jN_{21} & M_{22} + jN_{22} & M_{23} + jN_{23} \\ M_{31} + jN_{31} & M_{32} + jN_{32} & M_{33} + jN_{33} \end{bmatrix} \quad (17)$$

As can be seen, the tensor contains 9 complex values. However, because the tensor is symmetrical, only 6 unique values can be considered in the calculation of it. The complex characteristics of the tensor are based on the target's magnetic and conductive properties. For example, if the target object is only magnetic and not conductive, the tensor contains only real values. This kind of material is, for example, ferrite. If the target object contains also conductive properties, like aluminium, to be able to utilize the Eddy currents and magnetic field caused by those, the tensor consists of complex values. [50]

As said, the tensor is also dependent on the target dimensions. In Figure 7, some special cases for the tensor based on the object shape are presented. [50,60] In the modelling and experiments of the thesis, the target object is shaped as a rod. In Figure 7, the first tensor is for a magnetic rod, in which the field is concentrated along the rod's long dimension in y-direction, making it the main component of the tensor. This is also seen in the second tensor, where the field is concentrated to *x*- and *z*-directions, according to the long dimensions produced by the magnetic disk. However, conductivity of the object changes the situation because the Eddy currents produce a field that is perpendicular to the plane in which they are circulating. This can be observed from the third tensor in Figure 7 because most of the Eddy currents circulate at the large area of the disk, and the currents generate a field mainly in the perpendicular direction to the plane, which also concentrates the tensor to that component. [50]

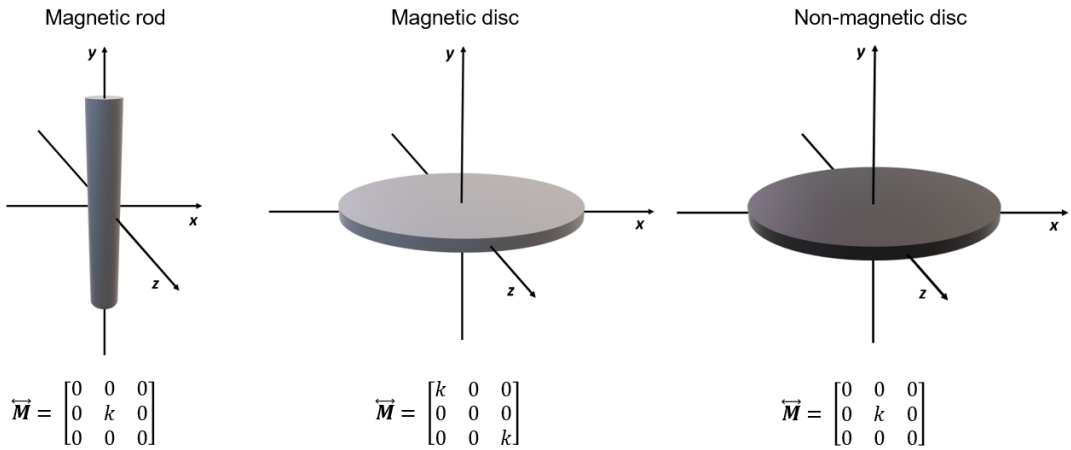

Figure 7. *Magnetic polarizability tensors for different object shapes and conductivities: magnetic rod, magnetic disk, and non-magnetic, conductive disk. Figure based on [50].*

By substituting the equations of the fields and the tensor, the induced voltage in the receiving coil becomes [60]

$$V_{ind} = \frac{j\omega\mu_0}{I_R}\left[H_x^R, H_y^R, H_z^R\right] \cdot \begin{bmatrix} m_{11} & m_{12} & m_{13} \\ m_{21} & m_{22} & m_{23} \\ m_{31} & m_{32} & m_{33} \end{bmatrix} \cdot \left[H_x^T, H_y^T, H_z^T\right]^T \tag{18}$$

Now, there are six field components which can be calculated as

$$\left[H_x^R, H_y^R, H_z^R\right] \cdot \left[H_x^T, H_y^T, H_z^T\right]^T = \underbrace{H_x^T H_x^R}_{hxx} + \underbrace{\left(H_x^T H_y^R + H_x^R H_y^T\right)}_{hxy} +$$

$$\underbrace{\left(H_x^T H_z^R + H_x^R H_z^T\right)}_{hxz} + \underbrace{H_y^T H_y^R}_{hyy} + \underbrace{\left(H_y^T H_z^R + H_y^R H_z^T\right)}_{hyz} + \underbrace{H_z^T H_z^R}_{hzz} \tag{19}$$

As can be seen, there are six unique combinations of the field components because the ones identical to *hxy*, *hxz* and *hyz* can be excluded. [60] And thus, the induced voltage becomes a product of the field vector and the magnetic polarizability tensor:

$$V_{ind} = \frac{j\omega\mu_0}{I_R}[hxx, hxy, hxz, hyy, hyz, hzz] \cdot [m_{11}, m_{12}, m_{13}, m_{22}, m_{23}, m_{33}]^T \tag{20}$$

Since the magnetic polarizability tensor contains information about the target object and its properties, the information on the location and orientation of the object is dependent on the *H* field components. [50,60]

3.2 Inverse problem

When the induced voltage that is caused by the a marker has been simulated or measured, it is possible to solve pose of the marker based on that information. The pose ***P*** consists of three components of position (*x, y, z*) and three components of orientation (*ϕ, θ, ψ*) of the marker:

$$\boldsymbol{P} = (x, y, z, \phi, \theta, \psi), \tag{21}$$

where (*ϕ, θ, ψ*) are roll, pitch and yaw, i.e., orientation of the marker with respect to x, y and z -axes [39]. As mentioned, information about the target's pose is embedded in the dot product of the transmitting and receiving magnetic fields. Since we know geometry of the localization coil array and properties of the marker, it is possible to simulate the values of the magnetic fields in different positions beforehand. In addition, the magnetic polarizability tensor for certain type of marker can be simulated before going into the

experiments. As shown in equation (20), the induced voltage values are then just a multiplication between the field components and the tensor. This is shown as a forward model of the system as [60]

$$f(\boldsymbol{P}, \boldsymbol{M}) = \boldsymbol{P}, \boldsymbol{M} \rightarrow \boldsymbol{V} \tag{22}$$

When the induced voltage caused by the marker is measured, information about the magnetic field values and the tensor can be applied to invert the measured voltage into a certain position and orientation in the target space. Essentially, this means that the pose of the marker is estimated repeatedly, and the calculated dipole model data is fitted into the measured values. This is called the inversion problem. [60] There are many different algorithms available that can be utilized in this type of problems, each having different properties. For example, the algorithm can be either linear or nonlinear, and direct or iterative. [60] Usually, for localization of a capsule endoscope or a similar target, a nonlinear, iterative algorithm is used. This is because the problem of such localization is usually ill-posed and requires regularization. [61] For example, Gauss-Newton and Levenberg-Marquardt are suitable algorithms. [61]

If either the magnetic polarizability tensor or the location is known beforehand, the algorithm becomes linear. However, usually there is at least some stage of uncertainty on these parameters. Therefore, the algorithm requires initial guesses of the location and tensor. For example, the first estimate of the tensor can be either a unity matrix or numerically modelled tensor, and guess of the location can be induced from the target response pattern. [50,60] With the use of these estimates, the dipole moment approximation is fitted to the measured data using the least squares method, and estimates of the location and tensor are updated:

$$\arg\min(\|\boldsymbol{V} - f(\boldsymbol{P}, \boldsymbol{M})\|^2) \tag{23}$$

For example, when Levenberg-Marquardt algorithm is used, it is in form

$$\left[\overleftarrow{\boldsymbol{M}}\,\boldsymbol{P}\right] = (\boldsymbol{J}^T\boldsymbol{J} + \lambda\boldsymbol{L}^T\boldsymbol{L})^{-1}\boldsymbol{J}^T\boldsymbol{R} \tag{24}$$

Where $\boldsymbol{L}$ is a regularization matrix and λ is a regularization parameter. [50,61] $\boldsymbol{J}$ in the equation is a Jacobian matrix that is a partial derivative of the forward model $\boldsymbol{F}$ with respect to the unknown parameter. In reference to the location this is

$$\boldsymbol{J} = \frac{\partial \boldsymbol{F}}{\partial \boldsymbol{P}} = \frac{\boldsymbol{F}(\boldsymbol{P} + \Delta\boldsymbol{P}) - \boldsymbol{F}(\boldsymbol{P})}{\Delta\boldsymbol{P}}. \tag{25}$$

$\boldsymbol{R}$ in the equation is a residual value. [60] It is used to determine the stopping criterion for the iteration process as

$$\boldsymbol{R} = \boldsymbol{V} - f\left(\boldsymbol{P}, \overleftrightarrow{\boldsymbol{M}}\right) \tag{26}$$

The residual value is calculated repeatedly, and the iteration process is terminated if its value begins to increase. [50]

4. METHODS

This Chapter introduces methods that are used in the design of electromagnetic coil arrays and evaluation of them by means of computational modelling. In addition, a general overview of the experimental setup and the measurement procedure are presented.

4.1 Modelling of novel sensor arrays and markers

In order to simulate the magnetic fields produced by the coils, both finite element method (FEM) -based modelling and MATLAB are utilized. In addition, principles of generating the coil array candidates, and a method to evaluate their sensitivities needs to be introduced. FEM-based modelling is also applied in target response simulations, and in calculation of magnetic polarizability tensors. Also, as resonance is utilized both in simulations and experiments, the principle of using the phenomenon is presented.

4.1.1 Field calculator

In order to find the optimal coil array for WEC localization, several different coil arrays are modelled using COMSOL Multiphysics software and analysed with MATLAB. COMSOL Multiphysics is used to model the fields produced by the coil arrays in order to calculate and visualize the sensitivity of the arrays. COMSOL is a FEM-based software in which the modelled geometry is discretized, and divided into small elements which is called meshing of the system. Differential equations that need to be solved in the model are calculated at each node of the meshed system, making the calculation numerical. The models can contain complex geometries and different materials, and the problem can be either steady state or time dependent. This makes FEM-based calculation good for simulating and visualizing different electromagnetic phenomena applied in the localization system. [62] However, the FEM-models with fine mesh and multiple channels in the coil array consume rather much time and computational power. Therefore, the Biot-Savart law, presented in section 3.1.2., is utilized and a magnetic field calculator is produced. The MATLAB program for the field calculator is presented in Appendix 1. It analyses the geometry of desired electromagnetic coil array based on its coordinates, calculates magnetic fields of linear coil edges and combines the information for both transmitting and receiving coils. This calculation of the magnetic fields is further utilized in the sensitivity analysis.

4.1.2 Principles of designing the sensor arrays

One main principle that is used in the design of the modelled coil arrays is that the coils within the array should be large in size. In the conference paper which was written as a part of the thesis, one of the main conclusions was that the bigger coil size leads to increased sensitivity of the array. [56] In addition, using large coils makes it possible to perform the localization further away from the array since the fields produced by large coils reach further than the one produced by a small coil. [49] Other point that needs to be considered in the design process is the number of measurement channels in the array. The more measurements we get with the array, the more information there is to use in the inversion of the pose. That is why multiple transmitting and receiving coils are utilized in most of the arrays.

In addition, it is encouraging to use many transmitters in the design because of so-called dead-angle challenge. It is a situation where the localized marker turns to be perpendicular to the exciting magnetic field. Thus, the magnetic field cannot properly excite the marker. If multiple different transmitters are used, it is possible to produce exciting fields in different directions. Another possibility would be to use a marker that is composed of three parts that are perpendicular to each other. However, this increases the size and weight of the marker, making it challenging to embed into the capsule design. [43]

So-called *gradiometer* coils or *differential* coils are utilized in all of the modelled systems. [60,63] Differential coils are commonly used, for example, in metal detection systems. They can be used to null the primary voltage produced by the transmitting field and improve the signal-to-noise ratio of the system. This can be done by having a receiving coil that is constructed of two equal halves in series and winding the halves to opposite directions. This way, the differential voltage measured with the receiving coil becomes zero when there is only the primary field to be measured. [49,60] Differential winding reduces the electromagnetic interference coupled to the receiving coils. By nulling the system properly, it does not pick up electromagnetic noise coming from, for instance, distant power lines, radio sources or geomagnetic fields. Similarly, differential winding in transmitter coils minimizes the electromagnetic interference caused by the coils themselves. Also, the field directions can be modified by having both differential and non-differential coils in the design. Even if it is possible to do the localization with a non-differential array, the benefit of nulling the primary field from the receiving coils and measuring only the voltage caused by the target object makes the differential arrangement appealing to utilize. [49,63]

4.1.3 Sensitivity analysis

As information about the target's pose is contained within the magnetic fields, *sensitivity* of the localization coil array can be studied by the dot product of transmitting and receiving magnetic fields, H_T and H_R, as shown in equation (19). If the calculated sensitivity components for the localization array are large in multiple directions, it is easier to determine the marker location and orientation. By analysing the sensitivity components within the target space, it can be evaluated whether a coil array is suitable for localization, and which areas of the array or orientations of the marker may cause challenges in the localization process. [56,60]

As the endoscopic capsule travels through the complex-shaped GI tract, the orientation and location of it are constantly changed during its travel. To be able to use the method for patients with different body types, four different coil array designs with large cross-sectional area, 60 cm by 60 cm, are modelled and evaluated. The sensitivity patterns of them are compared on a plane at 30 cm from the array, since the localization system should be able to perform its purpose also this far away from the array. With the planar array, this might be one of the main challenges compared to the double-sided or three-dimensional ones that could scan the target volume from many different directions. The designs are went through one by one, after which the information is concluded in order to select the most promising design for practical implementation.

4.1.4 Modelling of markers

COMSOL Multiphysics is utilized to simulate response of an array to different types of markers. In the target response simulations, the voltage induced to a receiving coil is first simulated with the marker positioned within the target space, after which the voltage is simulated with no target in the model. The voltage difference between these two situations is caused only by the marker, and therefore it is studied. The markers that are simulated are: solenoid with ferrite rod as a core, solenoid with air core and just a ferrite rod. In multiple studies, solenoid with a ferrite core has been used as a target [16,41–43]. However, a ferrite sample and an air-cored solenoid are modelled in order to justify whether the ferrite-cored one is the best fit for the purpose. In addition, the effect of using a resonant circuit as a part of the marker's solenoid is studied.

Size of the ferrite rod is 3 mm in diameter and 10 mm in height in each simulation, to enable inserting the marker inside a regular-sized capsule endoscope. The solenoid with 486 turns is wound around the ferrite sample in the simulations. Permeability of the ferrite

is 3000 in each simulation. Two different physics interfaces are used in COMSOL Multiphysics in target response simulations: Magnetic fields and Electrical circuits. The relative tolerance used in the simulations is 10^{-6} to ensure proper convergence of the solution. An iterative solver FGMRES is utilized in most of the simulations, and SSOR is used as a pre-conditioner. For simulations that study the resonance phenomenon, a direct solver, PARDISO, is applied. The models contain air as material of the target space because it is assumed that the magnetic fields can pass the human tissues with low attenuation.

4.1.5 Modelling and calculation of tensor

As mentioned, magnetic polarizability tensor is one of the main parameters for electromagnetic tomography applications. Therefore, tensors of two simple targets are modelled numerically. In order to calculate tensors for a ferrite rod and a solenoid target, they are modelled within a three-dimensional Helmholtz coil array in COMSOL Multiphysics. The geometry is visualized in Figure 8. The target is placed at the center of the array, so that it is aligned with the z-axis. In the Helmholtz-array, the coils opposing each other are excited simultaneously to produce a homogenous field that excites the marker. Similar configuration has been used for tensor computation in multiple studies, either as a numerical model or as an experimental measurement of the tensor [59,60].

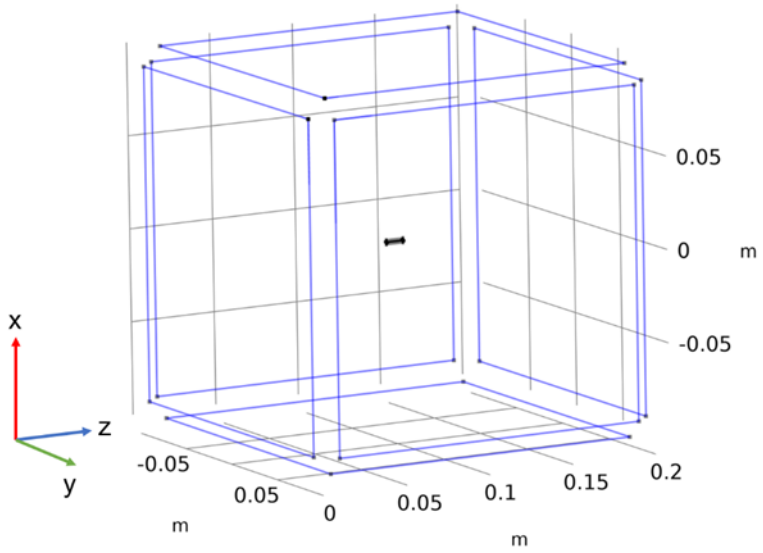

Figure 8. *Simulated three-axial Helmholtz coil array for calculation of magnetic polarizability tensor of ferrite samples.*

By calculating the sensitivity components at the location of the marker by the dot product of the magnetic fields, and simulating the voltage difference that is caused by the marker, it is possible to use equation (20), and calculate the magnetic polarizability tensor of the marker.

4.1.6 Resonance and RLC circuit

A phenomenon called resonance is commonly utilized in electromagnetic applications. An electrical resonance circuit contains a resistive element, an inductive element, and a capacitive element. The parameters of the inductive and capacitive components are dependent on the used frequency which can be utilized to reach a desired response of the whole circuit. [64]

The inductive element is made from a conductive material that is wound into a coil. The coil can either be air-cored or have ferromagnetic material as a core to modify the inductance of it. Inductive reactance is a parameter that explains how the inductor resists current in AC circuit, in similar way that resistance does for current in DC circuit. The inductive reactance is defined as

$$X_L = 2\pi f L = \omega L \tag{27}$$

where *f* is the frequency, *L* is the inductance of the coil and *ω* is the angular frequency. [64] As can be seen from the equation, inductive reactance is proportional to the frequency, so its value increases linearly as the frequency increases. This is visualized in Figure 9. Similarly than inductive reactance, capacitive reactance can be defined in terms of frequency as

$$X_C = \frac{1}{2\pi f C} = \frac{1}{\omega C} \tag{28}$$

where C is the capacitance. [64] Capacitive reactance explains the resistive phenomenon when the capacitor is charged and discharged and current flows through the circuit. As can be noticed, relation between the capacitive reactance and frequency is different from the inductive reactance. They are inversely proportional, so as the frequency increases, the value of the capacitive reactance decreases, shown in Figure 9 [64].

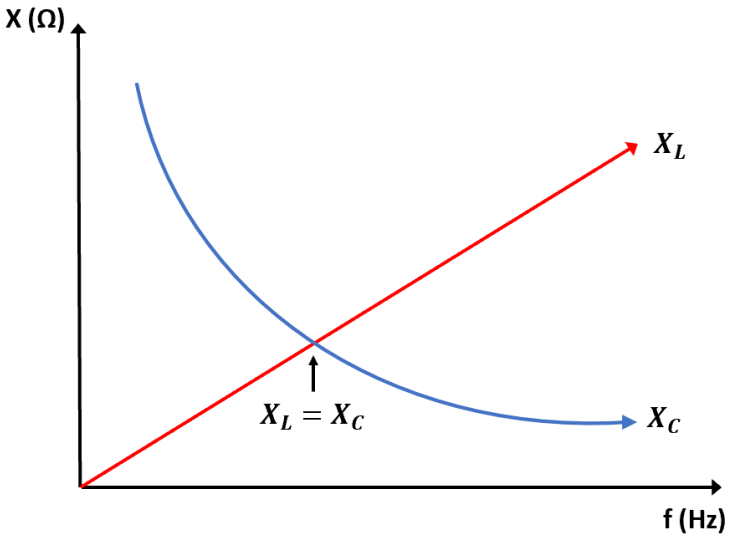

Figure 9. *Capacitive and inductive reactances as a function of frequency.*

The frequency-dependency of the reactances can be utilized in RLC (resistor-inductor-capacitor) -circuit, which can be either series or parallel circuit. For the series RLC-circuit, the reactances cancel each other out at a certain frequency which minimizes the impedance of the circuit, leading to a high current flowing through it. Similarly, for the parallel RLC-circuit, the reactances cancel out, and this leads to the maximum impedance of the circuit. [64] In both cases, the impedance at resonance is only dependent on the resistive component of the circuit, and the resonant frequency f_{res} is expressed as

$$f_{res} = \frac{1}{2\pi\sqrt{LC}} \tag{29}$$

Both the series and parallel RLC-circuits have many applications, for instance, as tuned circuits, filters or voltage multipliers. For example, it is possible to use an LC-circuit as a marker in electromagnetic localization system. In that case, the resistance of a series RLC-circuit is reduced to the smallest possible. This type of a circuit can pick up a particular frequency from a signal. [43,64] In addition, at the resonant frequency, the marker produces the largest voltage which is both seen in the measured voltage of the localization array, and as increased values of the tensor components. Another example of utilizing the resonance phenomenon in electromagnetic localization is to resonate the coils that produce the excitation field. By having a series resonance circuit, current flowing in the excitation coil can be maximized which results in stronger magnetic field produced by it.

4.1.7 Effective magnetic field

The magnetic dipole moment of a target can be formulated using the formulation shown in section 3.1.3. In the theory, the target is treated as a single current loop. However, as the marker in the electromagnetic localization system may contain multiple loops and be constructed to a solenoid form, number of turns in the solenoid is taken into account in the formulation:

$$\overrightarrow{\boldsymbol{m}} = NIS = N\frac{V_{emf}}{Z}S \tag{30}$$

where *N* is the number of turns of the marker, *I* is the current exciting the marker, *S* is area of the current loop around the marker, V_{emf} is the induced voltage at the marker and *Z* is impedance of it [43]. At resonance, this impedance is defined by the coil resistance, as presented in section 4.1.6. The induced voltage at the marker can be calculated as

$$V_{emf} = \mu_0\mu_r\omega NSH_{eff} \tag{31}$$

where μ_r is the relative permeability of the ferrite core and H_{eff} is the effective magnetic field that is actually exciting the marker when *demagnetizing factor* of the ferrite, N_d, is taken into account. [43] When the solenoid target comprises a ferrite core inside it, the magnetic properties of the ferrite produce a demagnetizing field that reduces the total magnetic field at that point. The effective field can be calculated from the exciting magnetic field H_{ex} as

$$H_{eff} = \frac{1}{1 + N_d\mu_r}H_{ex}\cos(\alpha) \tag{32}$$

where α is the angle between the exciting magnetic field and the dominant dimension of the marker. [43] There are multiple different ways to determine the demagnetizing factor for different shapes of cores. Usually, the effect of demagnetizing field is rather challenging to take into account and requires finite element method -based numerical calculation, even for objects with simple shapes. However, an ellipsoid is a form where the effect of demagnetization has been calculated to be dependent on a constant called demagnetizing factor. The same formulation has been utilized to estimate the factor in case of different shapes, for example, a cylinder. However, the factor is dependent on many properties of the target, for example, the length-diameter ratio and the direction of the exciting field. Therefore, many researchers have formulated their own estimation of the factor for a cylinder, and validated their results numerically or experimentally. [65–68] In our case, a simple expression of the demagnetizing factor N_d of the core is selected:

$$N_d = \frac{1.7(0.5F)^{0.13}}{d^3}\left(\frac{1}{F}\right)^2\left[\ln\left(\frac{1+d}{1-d}\right) - 2d\right] \tag{33}$$

where $F = l_{core}/r_{core}$, and constant d is formulated as a function of F as

$$d = \left[1 - \left(\frac{2}{F}\right)^2\right]^{\frac{1}{2}} \tag{34}$$

Thus, the value for demagnetizing factor for a ferrite sample with length of 10 mm and diameter of 3 mm would be 0.0948. [65,69] Now, the magnetic dipole moment of the marker $\boldsymbol{m}$ can be utilized to calculate induced voltage in the receiving coil as

$$V_{ind} = \boldsymbol{B}_{cal} S_{receive} \omega = \frac{\mu_0}{4\pi}\left(-\frac{\vec{\boldsymbol{m}}}{r^3} + \frac{3(\vec{\boldsymbol{m}} \cdot \boldsymbol{r}) \cdot \boldsymbol{r}}{r^5}\right) S_{receive} \omega \tag{35}$$

where $\boldsymbol{B}_{cal}$ is an approximate magnetic field caused by the marker when it is treated as a magnetic dipole, $S_{receive}$ is area of the receiver, $\boldsymbol{r}$ is position of the marker and r is distance between the marker and the receiver coil. Now, it can be noticed that there are two different formulations for the induced voltage in the receiving coil, (14) and (35). Therefore, these two formulations are compared with each other and with FEM-based modelling, in order to study whether one of the formulations could replace the computationally costly FEM.

4.2 Overview of the measurement system

Based on the sensitivity analysis, one of the modelled coil arrays is selected for construction, and measurement devices are connected to the array. In addition, the target type is chosen based on the target response simulations. The measurement system contains a few essential parts which are shown in Figure 10. The transmitting coil (Tx) is excited with a sine signal from function generator (Keysight 33500B Series Waveform Generator) with frequency of 103 kHz and peak-to-peak amplitude of 8 V. The sine signal is fed through a power amplifier (Texas Instruments OPA549) in order to drive the transmitting coils with high current and voltage. The transmitting coils are resonated near the function generator frequency to further increase amplitude of the signal. In addition, current in the transmitting coil is monitored with a current sensing power resistor.

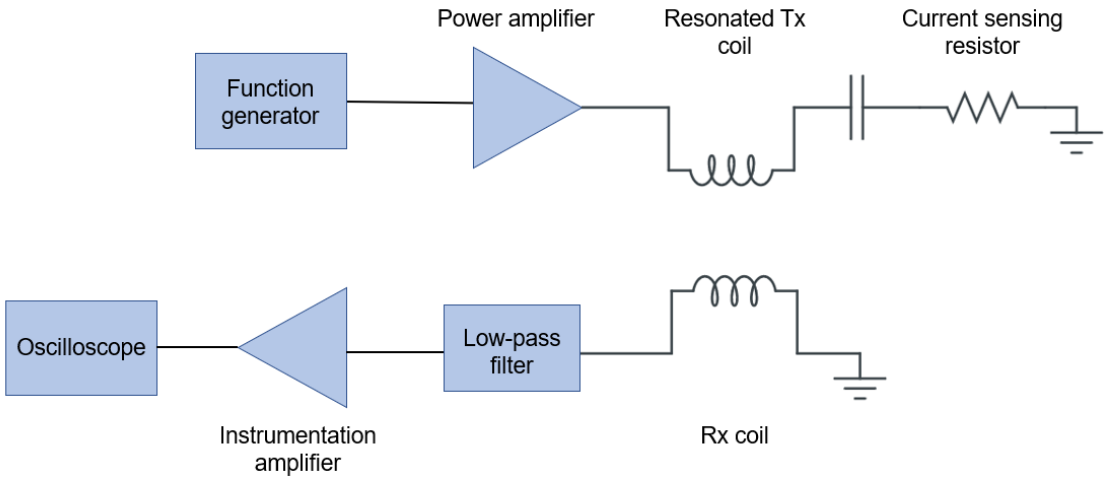

Figure 10. *Schematic of the measurement system.*

The receiving coil (Rx) is connected to a passive low-pass filter. This is because otherwise the natural resonant frequency of the receiving coil could couple to it, causing noise and making nulling of the receiving coil voltage difficult. After filtering, the signal is fed through an instrumentation amplifier (Texas Instruments INA103) to amplify the measured voltage and to reduce the common mode noise coupled to the signal. Both the power amplifier and the instrumentation amplifier are powered with a DC voltage source (Tenma 72-8690) with voltage of ± 21 V. Figure 11 shows the measurement setup.

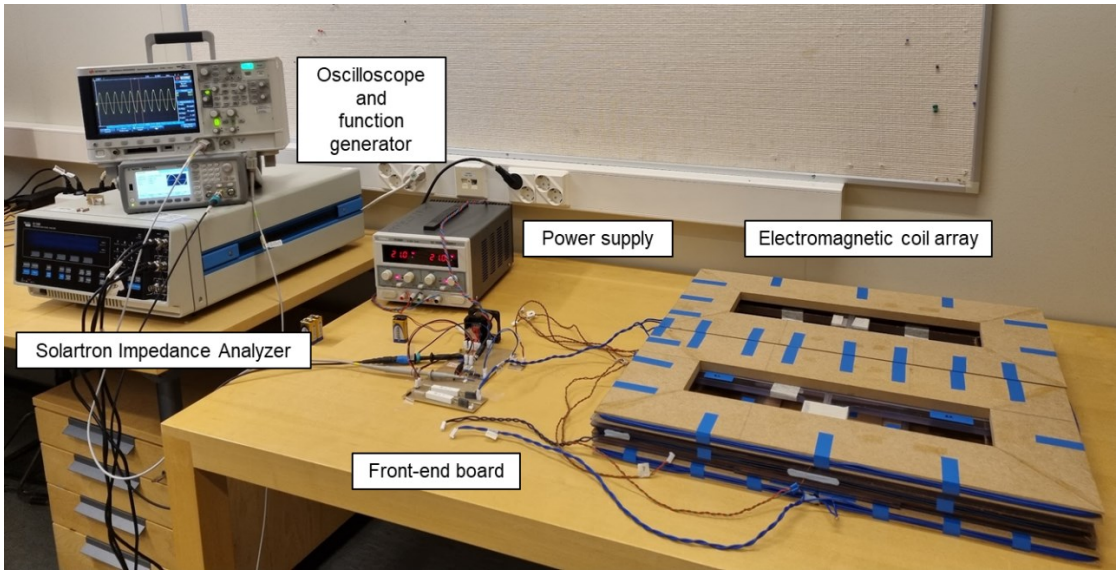

Figure 11. *A picture of the measurement system.*

In addition to the measurement devices presented in Figure 10, an impedance analyzer (Ametek Solartron SI 1260A) is applied to measure the impedance curves of both transmitting, receiving and marker coils as a function of frequency. This is done to study the resonance point of each coil. The device is shown in Figure 11.

As can be seen from Figure 11, all of the measurements are performed on a table with no metallic components, and as far away from the power lines as possible. The system can easily be affected by metallic objects if they are brought into the target space of the array. However, as the coils are being nulled before the experiments, the system becomes resistant to electromagnetic noise coming from sources that are far away [49]. In addition, all coils are wound around non-metallic frames: transmitting coils are made of medium-density fibreboard and bakelite, and the receiving coil frames are made of polycarbonate.

As the final coil array and target type are selected based on the modelling results, final design of the measurement system is explained in more detail in section 5.2. There, spesifications of the transmitting and receiving coils and the marker are measured and presented, and electronics needed for the system are introduced. After constructing the system, functionality of it is tested by positioning the marker at different positions in reference to the array, and voltage induced by the marker is measured at the receiving coil. In addition, the effect of changing marker's orientation with respect to the array is studied.

5. RESULTS

In this Chapter, results of modelling and experiments are gone through. The modelling results contain designs of the coil array candidates, their sensitivities, and selection of the optimal target. Based on the modelling results, the experimental setup is finished by measuring the properties of different parts of the coil array and by selecting the electronics for the system. Finally, functionality of the system is tested by using one of the receiving coils and measuring response of the system with different positions and orientations of the marker. The measured values are also compared to simulated ones.

5.1 Results of modelling

Based on the modelling principles, four different coil arrays designs are selected for analysis with COMSOL Multiphysics and MATLAB. Sensitivity of them is visualized and discussed. In addition, different target types: ferrite sample, air cored solenoid and ferrite cored solenoid, are modelled in order to find the optimal target for experimental study. As a part of the target design, the effect of resonance is studied. In addition, tensors of different ferrite samples are modelled and calculated.

5.1.1 Sensitivity of coil design 1

The first coil design is an array with three transmitters, from which two are differential coils. In addition, the design contains six differential receiver coils. The design is presented in Figure 12. There are totally 12 measurement channels in the design, since all of the receivers can be used with the square-shaped transmitting coil but there is a challenge with the differential transmitters. For example, if the upper differential transmitter *Tx2* is used as an excitation source, the upper receivers act correctly as differential coils since the halves of a single receiver are in identical fields, resulting as a zero voltage at the empty situation. However, the bottom receivers cannot be used with this transmitter because the halves are placed on fields that are in opposite directions.

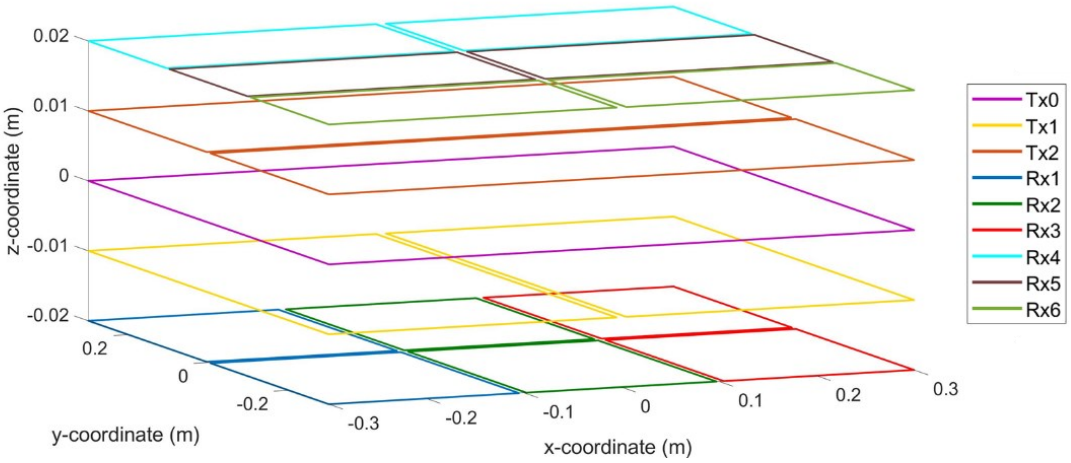

Figure 12. *Geometry of coil design 1.*

The advantage of adding differential transmitters to the design is demonstrated in Figure 13. In figure 13 a), direction of magnetic field produced by a square-shaped coil is shown as arrows on an xz-plane in the middle of the array. Also, a contour map of the field magnitude is included in the figure, showing that the fields are concentrated around the coil edges. As can be seen, the field is mostly oriented 90 degrees with respect to the plane where the coil is placed almost in the whole target area. The field direction is differing only near the coil edges. On the contrast, field produced by a differential transmitter, which is seen in Figure 13 b), is oriented differently at different parts of the target space because the coils are wound to opposite directions. By having both types of transmitters in the design, the marker can be excited from many directions which helps the localization process.

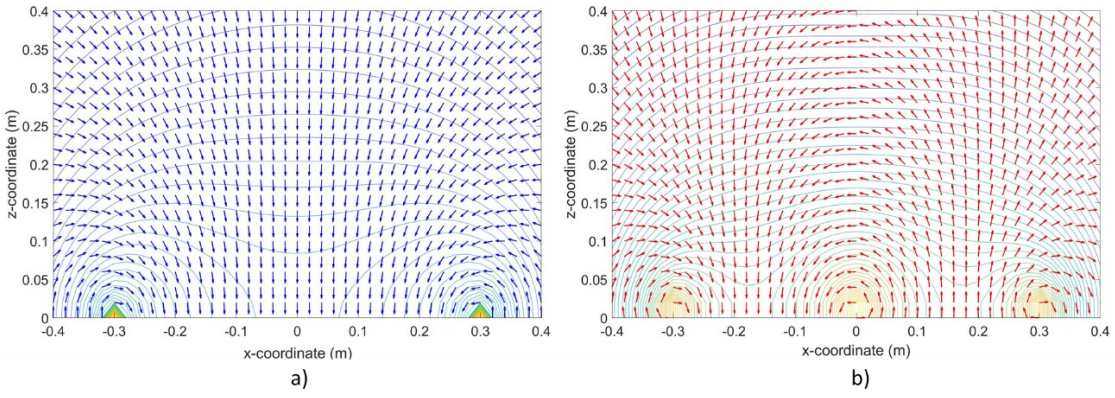

Figure 13. *Directions of magnetic field produced by a) square-shaped coil and b) a differential coil on a xz-plane orthogonal to the coils.*

Sensitivity of the coil design 1 is visualized on an xy-plane at height of 30 cm from the coil array. It is shown in Figure 14. By using the dipole model formulation and dot product of the magnetic fields, six sensitivity components have been calculated for the design.

The size of the xy-plane is 80 cm by 80 cm, and components for all channels are calculated on each point of the plane with resolution of 1 cm. The sensitivity magnitudes are calculated and visualized by taking an average of all transmit-receive channels. The maximum value of all of the components, shown at bottom right of the figure, is used as normalization factor for the maps. In addition, the maximum value of each component is shown above the corresponding map.

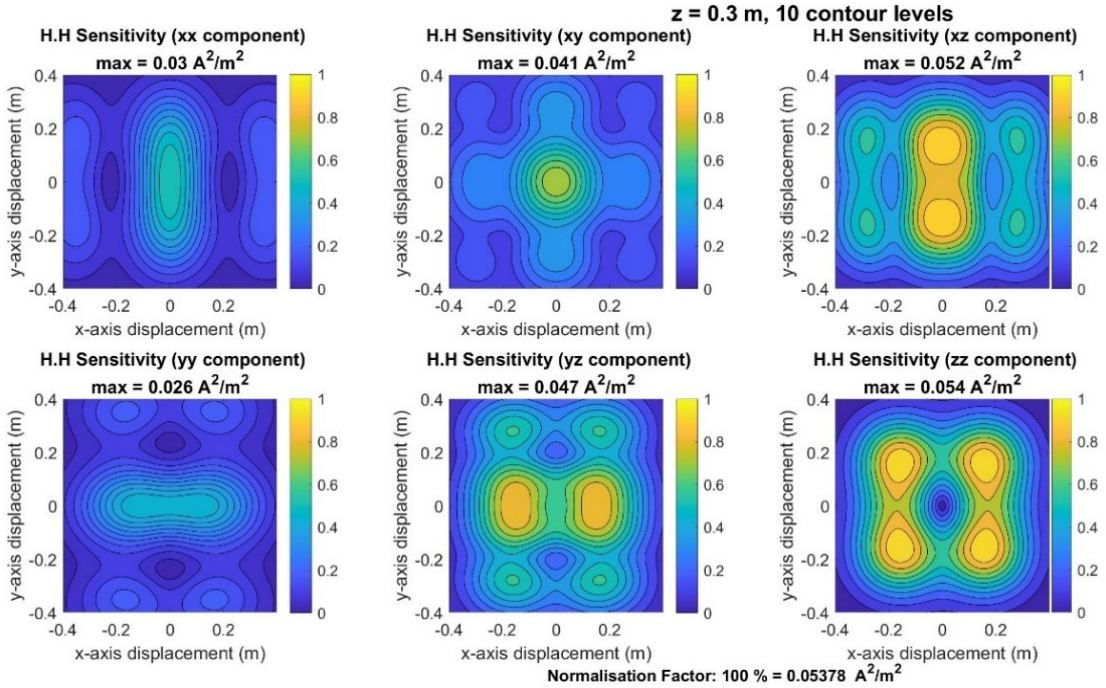

Figure 14. *Sensitivity maps of coil design 1, on xy-plane at height of 30 cm from the coil array. The components are calculated using the dipole model approximation.*

It can be noticed from the figure that the maximum sensitivity is found from the zz-component. It is reasonable, since the H_T and H_R fields are mostly oriented along the z-axis. However, also the xz- and yz-components have high sensitivity areas because of the differential arrangement of the coils. It can be observed that the zz-direction sensitivity has a minimum point in the middle of the array because most of the differential coils have a crossing point there, and therefore, the fields are not oriented along the z-axis. The opposite phenomenon is seen in the xx- and yy-components, as there the maximum sensitivity area is seen along differential coil crossing point. As the xx- and yy- components contain quite large areas with smaller sensitivity that the other components, they could be further improved to enhance functionality of the system.

5.1.2 Sensitivity of coil design 2

The second coil design is similar to the first one, only the receiving coils are split to three parts. They still work as differential receivers the same way than in coil design 1, since the first and third part of the receiving coil are wound to opposite direction with the middle one, and coil parts at both ends produce together equal area with the middle one. The design is shown in Figure 15.

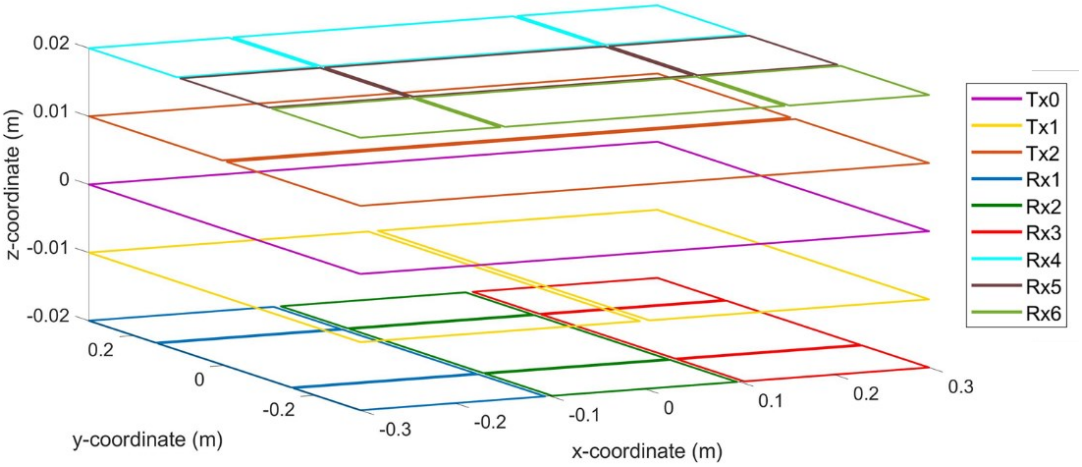

Figure 15. *Geometry of coil design 2.*

Sensitivity components of coil design 2 are visualized on the xy-plane at 30 cm distance from the coils. They can be seen from Figure 16.

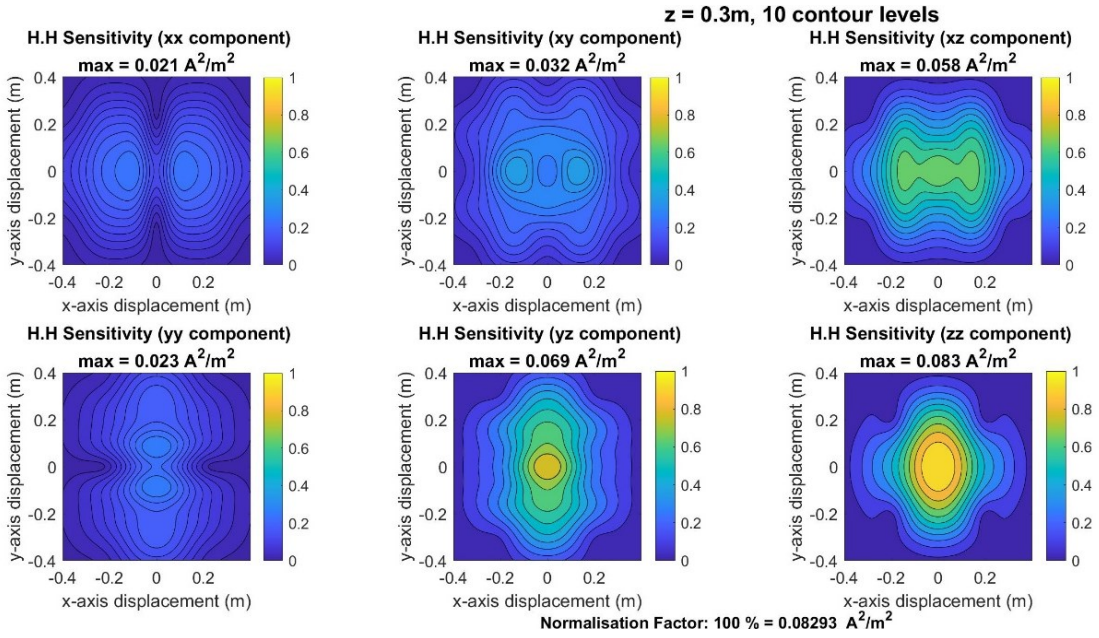

Figure 16. *Sensitivity maps of coil design 2, on xy-plane at height of 30 cm from the coil array. The components are calculated using the dipole model approximation.*

As can be seen from the figure, the maximum sensitivity of the array at the *zz*-direction is larger than for coil design 1. However, size of the high sensitivity areas is quite small compared to the previous design, and the *zz*-component comprises large areas with very small sensitivity at the corners. In addition, maps that do not contain impact of the z-component (*xx*, *yy* and *xy*) seem quite homogenous with small sensitivity values. Also, one challenge of the design is that balancing of the coils becomes more challenging when the differential coils are more complex.

5.1.3 Sensitivity of coil design 3

The third proposed coil design contains one non-differential transmitting coil, *Tx0*. In addition, there are 9 square-shaped differential receiving coils in the design. They are arranged so that one half of a receiver is placed on top of the transmitter and the other half is placed below the transmitter, so that the measured voltage is nulled when only the primary field is on. Coil design 3 is visualized in Figure 17.

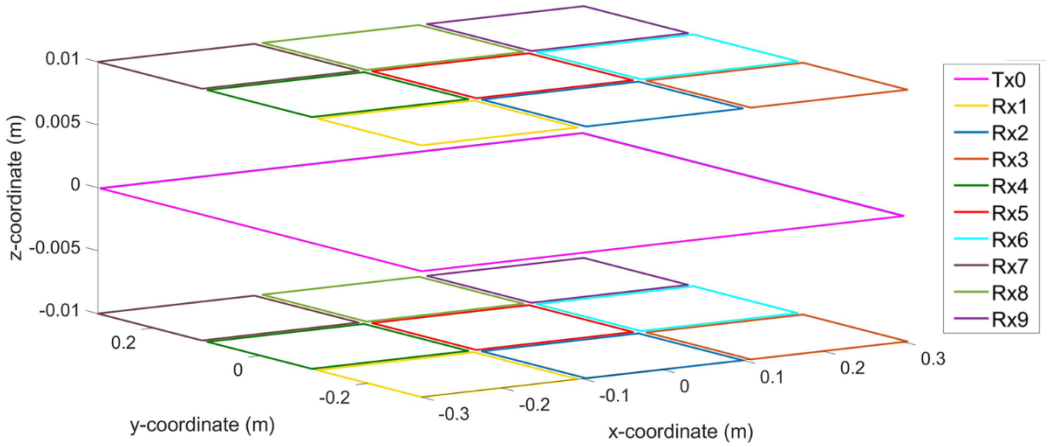

Figure 17. *Geometry of coil design 3.*

Sensitivity maps of coil design 3 are displayed in Figure 18, showing that the maximum sensitivity reached is approximately ten times smaller than for the previous two designs. This is probably caused by use of smaller receivers compared to the coil designs 1 and 2. As the sensitivity is dependent both on the transmitting and receiving magnetic fields, and a smaller coil produces also smaller magnetic field in magnitude, this is seen in the sensitivity patterns. However, maps that include the z-component show large areas that have relatively high sensitivity. Also, one advantage of the design is that the receivers are placed so that they fill up the transmitter area evenly and all of them are at the same

level. With coil designs 1 and 2, there are two levels of transmitters and receivers and not all of them can be used with each other.

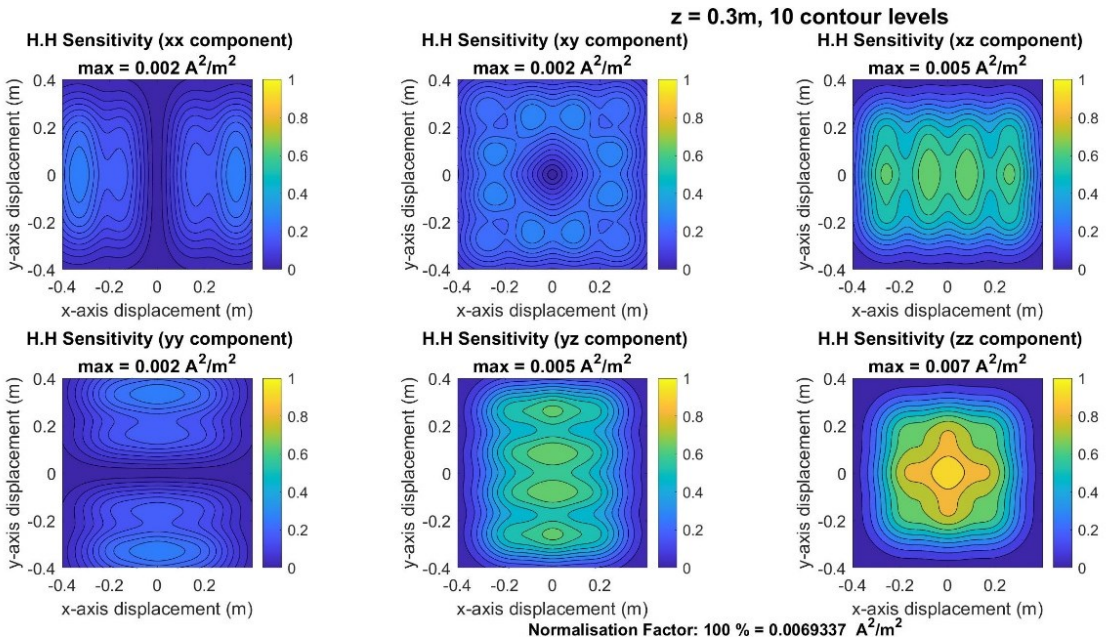

Figure 18. *Sensitivity maps of coil design 3, on xy-plane at height of 30 cm from the coil array. The components are calculated using the dipole model approximation.*

Number of channels in this design, 9, is smaller than for the previous two arrays. This reduces the number of measurements than can be used for inverting the location and orientation. However, similar designs have been successfully used for metal detection purposes where estimation of the target location is rather imprecise. [49] There, the main purpose is to study whether any metallic target is within the target space of the sensor. As regards of localization of a biomedical sensor, it is good to have many measurements and high sensitivity. Therefore, Coil design 3 does not seem to be appropriate for the purpose.

5.1.4 Sensitivity of coil design 4

Coil design 4 is a modified version of the third one, with one additional transmitting coil, *Tx1*, at the center of the large *Tx0* coil. The system can been seen from Figure 19. When the inner transmitting coil is wound to opposite direction with the outer one and they are excited at the same time, produced magnetic field is curled from inner coil to the outer one. Hence, the large transmitting coil can be first excited on its own, after which both of the transmitting coils are excited at the same time. This increases the number of Rx-Tx measurement channels to 18 and diversifies the excitation field vector directions.

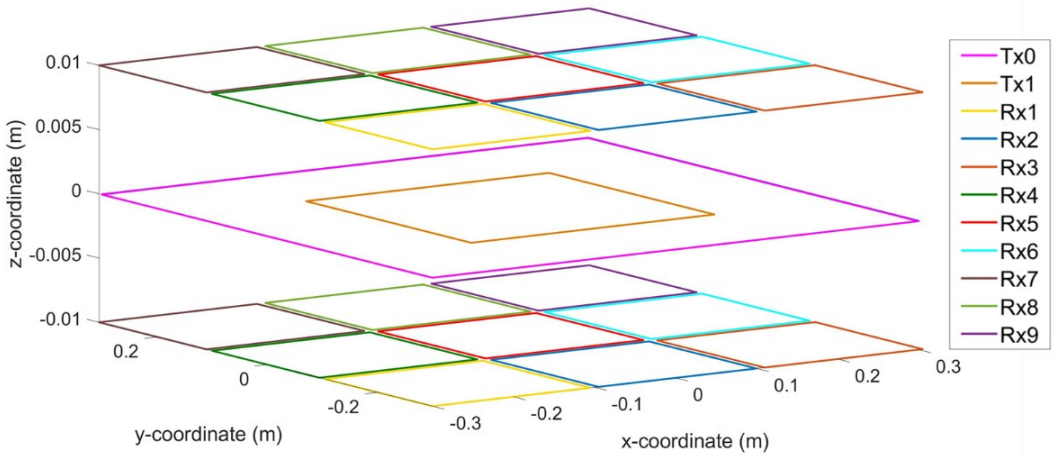

Figure 19. *Geometry of coil design 4.*

Effect of the inner transmitter coil is presented in Figure 20, where the magnetic field directions are visualized as arrows on a xz-plane in the middle of the array. In the design, the inner transmitter is excited with double the current of the outer transmitter, that is, when the outer transmitter *Tx0* is excited with 1 A, the inner *Tx1* is excited with 2 A to opposite direction. By modifying the ratio of currents in the coils, the field directions can be modified further.

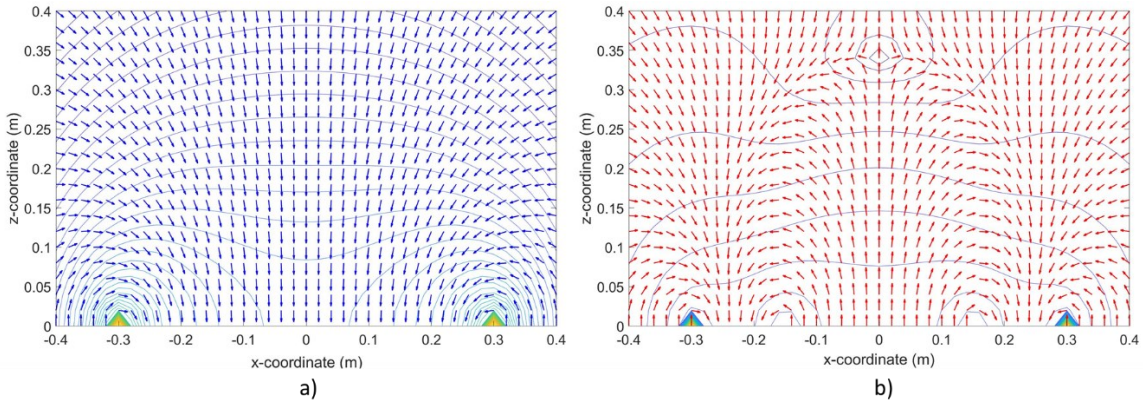

Figure 20. *Directions of magnetic field produced by a) square-shaped transmitting coil Tx0, and b) square-shaped coil Tx0 with an inner transmitter Tx1 on a xz-plane orthogonal to the coils.*

Finally, the sensitivity components of coil design 4 are found from Figure 21. Patterns within the maps are nearly similar with the previous design. However, maximum values of the components are smaller than for coil design 3, which is probably caused by the curled excitation field at height of 30 cm. This is also shown in Figure 20 of the field directions.

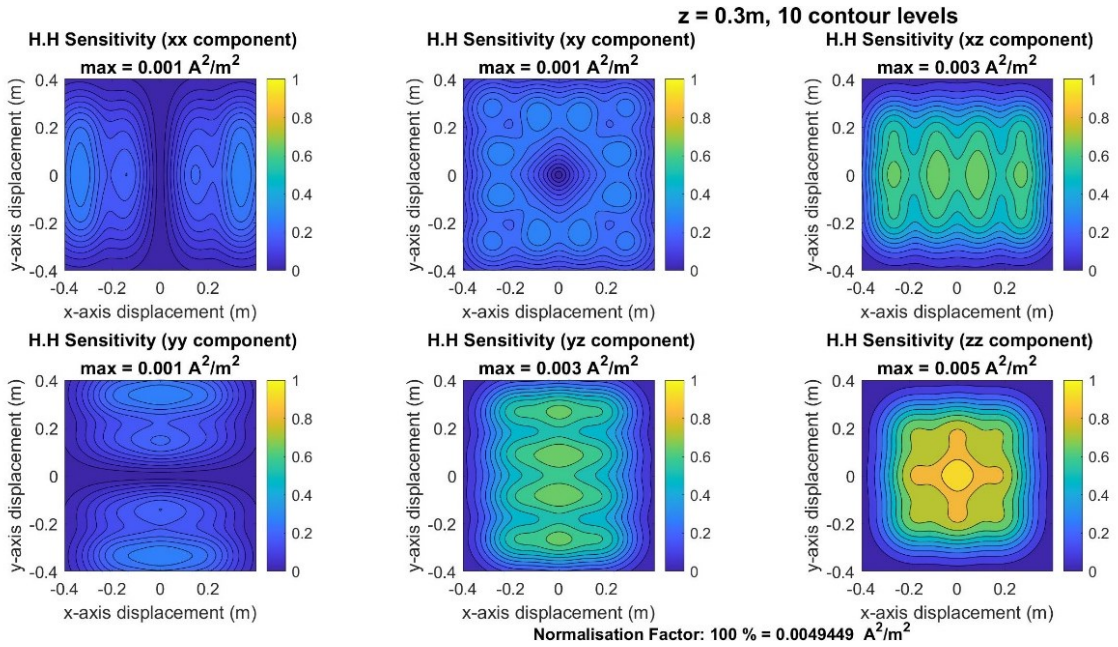

Figure 21. *Sensitivity maps of coil design 4, on xy-plane at height of 30 cm from the coil array. The components are calculated using the dipole model approximation.*

It would be possible to modify the sensitivity patterns of coil design 4 by adjusting the current amplitudes in the transmitting coils. However, the sensitivities seem rather small compared to the designs 1 and 2. To produce sensitivity amplitudes comparable to the designs 1 and 2, the coils should be excited with much larger current than the first two arrays. In addition, the system becomes quite challenging to put together and balance with the inner and outer transmitting coils. Therefore, it does not seem justifiable to modify the field parameters.

5.1.5 Comparison of the coil arrays

Information about the coil array designs is concluded in Table 4. The table contains the number of transmitting and receiving coils in the arrays, the number of measurement channels in the systems and the maximum sensitivity of the analyzed sensitivity patterns at height of 30 cm. Height of 30 cm was selected for the analysis because it is appealing to produce a system that could perform at that large distance in order to use the technology for many body types. The maximum sensitivity of each array was found from the zz-component.

All of the designs have their advantages and challenges. For example, coil designs 3 and 4 have smaller sensitivity at 30 cm height than the other two arrays. However, by adding the inner transmitting coil, it is possible to easily modify the shape of the excitation

field. For instance, if the number of turns in the inner transmitting coil is increased compared to the outer transmitter, the field geometry changes. However, quite similar effect can be achieved with the differential transmitting coils of coil designs 1 and 2. Coil design 4 contains the highest number of channels, 18, but also the first two designs end up with rather many channels with higher sensitivity.

Table 3. *Comparison of the four different coil arrays, and their sensitivity at 30 cm height.*

Coil array	Number of Tx	Number of Rx	Number of Channels	Maximum sensitivity (A^2/m^2) at 30 cm height
Design 1	3	6	12	0.054
Design 2	3	6	12	0.083
Design 3	1	9	9	0.007
Design 4	2	9	18	0.005

Based on the sensitivity analysis, coil design 1 seems to be the most optimal one for the purpose. It produces high sensitivity in multiple directions, includes rather many measurement channels and seems to be easier to balance compared to coil design 2, where the receiving coils are separated to three pieces. Therefore, coil design 1 is selected for a practical implementation.

5.1.6 Results of target response simulations

To study which kind of marker would be the most optimal one to be placed inside the WEC for localization, three different markers are simulated in COMSOL Multiphysics. The simulation is done using one channel of coil design 3. In the simulation, the transmitting coil is excited, and receiving coil at the center of the array, Rx5, is used to measure the voltage. The marker is placed at the center of the receiver, and it is moved further away from the array, from 10 cm to 30 cm. The marker is oriented along the receiving coil's axis. To get the voltage caused only by the marker, the simulation is first run with the marker and then without it, and the voltage difference between the situations is plotted. Results of the simulations are shown in Figure 22.

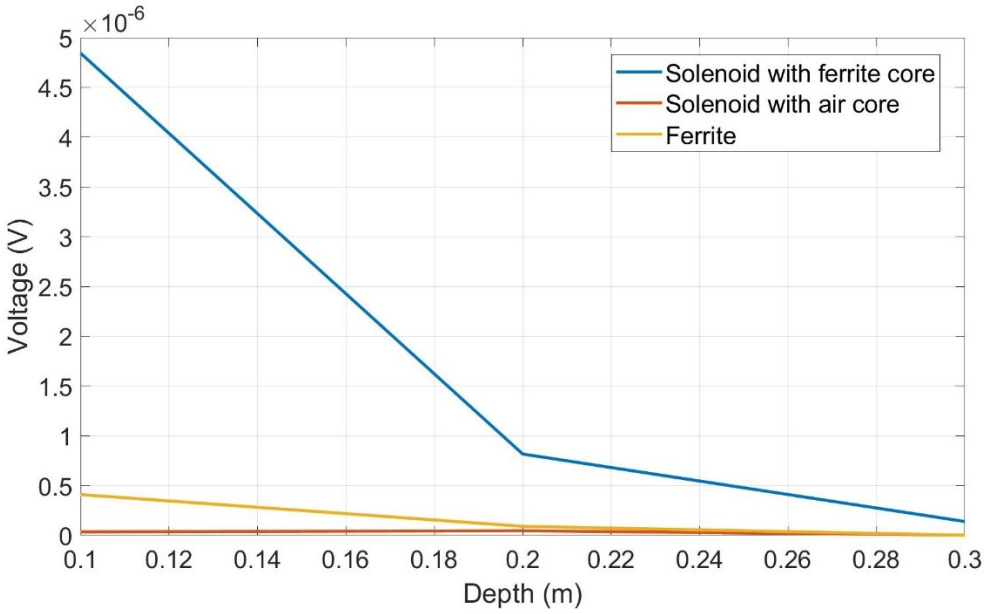

Figure 22. *Comparison of different marker types. The marker is positioned on the receiver axis from depth of 10 cm to 30 cm from the coil array. The simulation is done using channel Tx0-Rx5 of coil design 3.*

As can be noticed from Figure 22, marker with a ferrite core inside a solenoid gives the largest response compared to the other two. The smallest response is caused by the solenoid with air core which is reasonable since the solenoid is rather small and the effect of induction in the solenoid does not alone cause a large voltage. Therefore, it is justified to use a ferrite-cored solenoid as a marker. However, it is also possible to resonate the marker and further improve the measured voltage values.

Next, a resonant circuit is added as a part of the solenoid around the ferrite rod. By adding a capacitor of 1.12 nF in series with the solenoid, the marker becomes resonated at 100 kHz. This test is done with one channel of coil design 1: Tx0 is used as transmitter and Rx5 as receiver. Now, the marker is kept at one point in the middle of one half of a receiving coil at distance of 20 cm, and the excitation frequency of the square-shaped transmitting coil is varied. In Figure 23, the measured voltage at the receiving coil is clearly showing the effect of resonance. The measured voltage becomes more than ten times larger at the resonant frequency compared to ±10 kHz away from the resonance point.

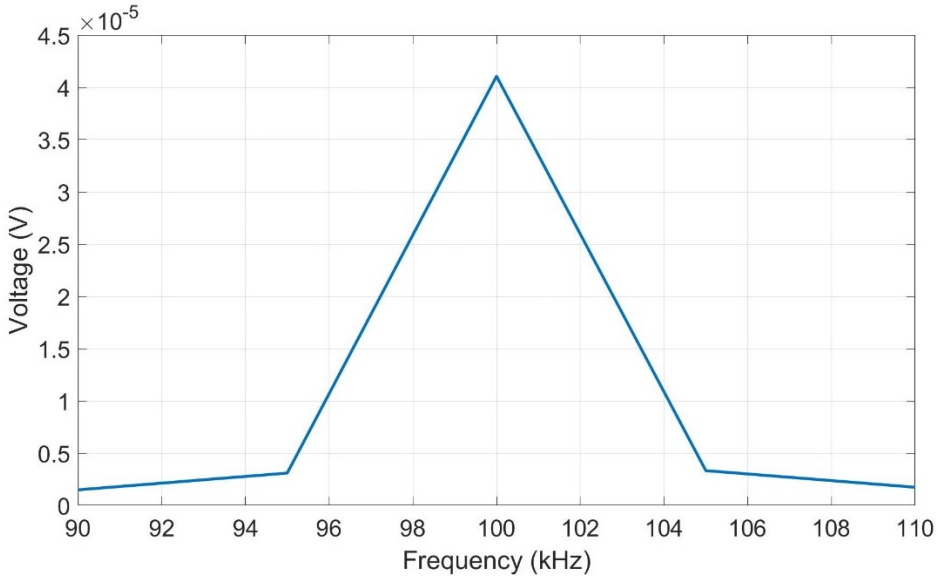

Figure 23. *The effect of resonance. A solenoid target with ferrite core is kept at one position, and the excitation frequency of the transmitter is changed. The simulation is done using channel Tx0-Rx5 of coil design 1.*

The effect of resonance can also be seen from Figure 24, where the marker is swept across the receiving coil Rx5 at height of 20 cm, and the voltage is measured in every 10 cm. Voltage at the receiving coil is shown as an absolute value. As can be noticed, with resonance, the measured voltage is clearly larger than with a ferrite-cored solenoid target with no resonant capacitor added. However, both cases show a reasonable shape of the voltage graph as it has been measured with a differential receiver.

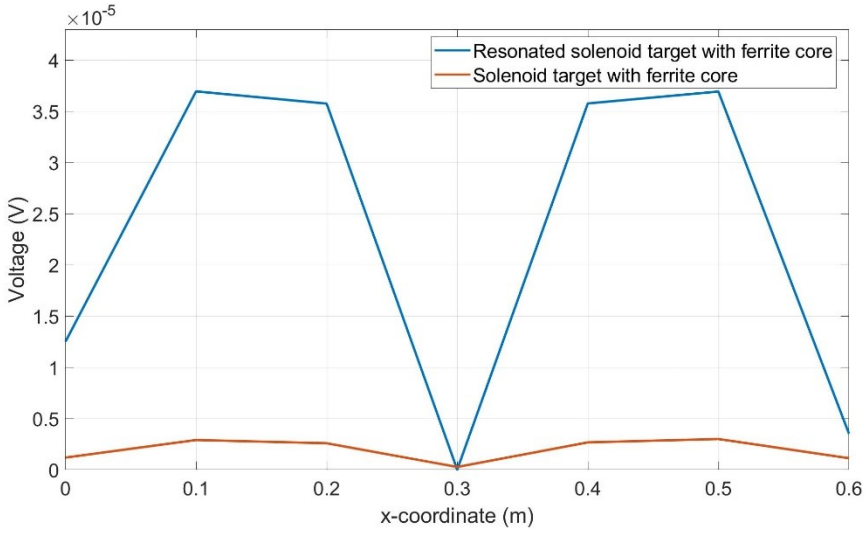

Figure 24. *Voltage caused by resonated and non-resonated solenoid targets with ferrite core, when the target is swept across a differential receiver coil. The simulation is done using channel Tx0-Rx5 of coil design 1.*

Based on the target simulations, it is justified to use a resonated solenoid marker with ferrite core as a marker in the measurements.

5.1.7 Magnetic polarizability tensors of targets

Tensors of different ferrite samples are modelled using the three-axial Helmholtz coil configuration in COMSOL Multiphysics. In Table 4, magnetic polarizability tensor of a ferrite rod with diameter of 3 mm and length of 10 mm is presented. The relative permeability used in the simulation is 3000, and the frequency is 100 kHz. As can be seen, values on the diagonal of the matrix are significantly larger than the other values. Thus, the other components can be considered as zeroes. All of the values contain only a real component, which is expected for magnetic material that is not conductive. The largest value of the tensor is found from the zz-component which is reasonable, as the dominant dimension of the rod is aligned with the z-axis. If the diameter of the rod was relatively smaller compared to the length of the rod, the xx- and yy-components would most probably become smaller too. If the permeability of the ferrite is changed, the values on the diagonal change as well. For example, if the permeability is decreased from 3000 to 200, the xx and yy- components decrease 1.2 % and the zz-component decreases 5.7 %.

Table 4. *Magnetic polarizability tensor of a ferrite rod with relative permeability of 3000 at frequency of 100 kHz.*

	x	*y*	*z*
x	1.67×10^{-7}	8.06×10^{-12}	1.27×10^{-11}
y	2.65×10^{-12}	1.67×10^{-7}	2.47×10^{-11}
z	1.90×10^{-11}	2.46×10^{-11}	8.55×10^{-7}

Tensor of a solenoid target with ferrite core is presented in Table 5. Now, all of the components have an imaginary part in them because of the conductivity of the solenoid wire. In the simulation, the marker with 486 turns is resonated at 100 kHz, and the relative permeability for the core is 3000. Now, the zz-component is significantly larger than any other value in the tensor which is caused by the effective excitation of the solenoid at that direction. The other components are not that large because the magnetic field needs to be at 90 degrees angle to the solenoid cross-sectional area in order to effectively induce a voltage in it. However, effect of the ferrite core is seen as larger real parts of xx- and yy-components compared to the other ones, as explained for the ferrite tensor.

Table 5. *Magnetic polarizability tensor of a resonated solenoid with a ferrite core with relative permeability of 3000 and resonant frequency of 100 kHz.*

	x	y	z
x	$1.67 \times 10^{-7} - 3.06 \times 10^{-12}j$	$-2.18 \times 10^{-11} + 6.18 \times 10^{-14}j$	$-1.69 \times 10^{-9} + 2.97 \times 10^{-9}j$
y	$1.77 \times 10^{-12} - 5.56 \times 10^{-15}j$	$1.67 \times 10^{-7} - 3.01 \times 10^{-12}j$	$-2.18 \times 10^{-10} + 3.66 \times 10^{-10}j$
z	$-7.72 \times 10^{-10} + 1.35 \times 10^{-9}j$	$1.13 \times 10^{-9} - 1.95 \times 10^{-9}j$	$5.44 \times 10^{-5} - 9.40 \times 10^{-5}j$

The presented tensors seem also to be in accordance with the simulated voltages. For example, the zz-component of the resonated solenoid is approximately 10^{-4} in magnitude. The corresponding component for the ferrite sample is approximately 100 times smaller. The same phenomenon is detected from the simulated voltages, as the voltage caused by the ferrite marker at 20 cm height is in range of 10^{-7}, as the voltage caused by the resonated solenoid is in range of 10^{-5}. In general, composition of the tensors seem to be aligned with the theory. Thus, it is shown that COMSOL Multiphysics can be used to simulate the tensor which can be further used as a parameter of the inversion algorithm.

5.1.8 Simulation of effective magnetic field

Induced voltage at the receiving coil can be calculated from the magnetic dipole moment ***m*** according to equation (14). This takes into account the magnetic field produced by the receiving coils, and exact coordinates of them. As comparison, the induced voltage calculated by (35) utilizes only the average coordinates of the receiving coil and its area, and uses this information to estimate the voltage caused by the small magnetic dipole. This is visualized in Table 6, where induced voltages at differently sized receivers are calculated based on these two formulations, and the relative difference between the two is shown in percents. All of the values are generated by having the following parameters: a transmitter in size of 60 cm by 60 cm is used to generate a field, and a resonated solenoid marker is placed at 30 cm distance from it. The receiver is placed at the same position with the transmitter, and the area of it is changed. The marker has relative permeability of 3000, length of 1 cm and diameter of 3 mm, and it is resonated at 100 kHz by having a capacitor of 1.1243 nF in series with it. The marker has 486 turns of wire with diameter of 0.1016 mm in it. In order to analyze the resonance of the marker, the same situation is modelled in COMSOL Multiphysics. When the transmitter is excited by current of 1 A, the marker inductance based on the COMSOL simulation is 0.002253 H.

Therefore, at frequency of 100 kHz, the inductive and capacitive reactances cancel each other out, and impedance of the marker is calculated based on the wire properties

$$R = \frac{l_{wire}}{\rho_{wire} S_{wire}} = \frac{2\pi \cdot 0.015\, m \cdot 486}{6 \cdot 10^7 \cdot \pi \cdot (0.0508 \cdot 10^{-3})^2} = 9.42\, \Omega \quad (36)$$

where l_{wire} is length of the wire around the solenoid, ρ_{wire} is conductivity of the wire and S_{wire} is the cross-sectional area of it. The same phenomenon is seen at the numerical model.

Table 6. *Induced voltage at differently sized receivers calculated based on two formulations, and the relative difference between them.*

$S_{receive}$	Equation 14	Equation 35	Difference
0.6 * 0.6 m²	3.0831e-6	1.0680e-5	71 %
0.3 * 0.3 m²	1.7441e-6	2.6701e-6	35 %
0.04 * 0.04 m²	4.7049e-8	4.7468e-8	0.9 %
0.01 * 0.01 m²	2.9651e-9	2.9667e-9	0.06 %

As can be seen from Table 6, the approximate calculation of the induced voltage with equation (35) becomes different from the dipole model -based result when size of the receiver is increased. When the values are compared to simulated results from COMSOL, it is noticed that the value of voltage at the marker, V_{emf}, differs from the COMSOL result only by 0.29 %. However, neither of the equations is giving the same value for induced voltage at the receiving coil than COMSOL. Therefore, the dipole model approximation only works from the transmitting coil to the marker but not from there to the receiver if the receiver is placed close to the marker and is large in size. Hence, numerical calculation by COMSOL Multiphysics software is used as simulation tool, as it can take the voluminous properties of the marker properly into account.

5.2 Final design of the experimental setup

To test the feasibility of the technology, one of the modelled coil array designs is selected for experimental part: Coil design 1. In this section, different parts of the design are gone through in more detail: the transmitting and receiving coils of the selected design, construction of the whole array, electronics needed for the front-end board and markers that are used for the localization. After constructing the system, it is tested with the selected marker. System's response level at different positions and orientations of the marker is

discussed, and the possibility of using the system for real-life localization with inversion algorithm is estimated.

5.2.1 Transmitting coils

There are two different types of transmitting coils in the selected localization system. There is one square-shaped transmitting coil in size of 60 cm by 60 cm in the middle of the array stack. This coil is a non-differential one with 18 turns of 2.3 mm diameter stranded wire. Impedance of the coil as a function of frequency, measured by Solartron SI 1260A, is presented in Figure 25. As can be noticed, the natural resonant frequency of the transmitting coil itself is around 700-800 kHz. However, as the transmitter needs to be driven with high current and voltage to produce a strong magnetic field, a series resonance phenomenon is utilized in the transmitter. Figure 25 illustrates the effect of adding a power capacitor in series with the transmitting coil. As mentioned, series resonance causes the impedance to reach its minimum at the resonant frequency, leading to high current flowing through the transmitting coil [64]. From linear part of the impedance graph of the transmitter, it is possible to calculate the coil inductance as

$$L = \frac{Z}{2\pi f} = 564\ \mu H \tag{37}$$

By adding a power capacitor of 4.7 nF in series with the coil, the circuit can be resonated approximately at 97 kHz, which is seen from Figure 25 as a downward peak.

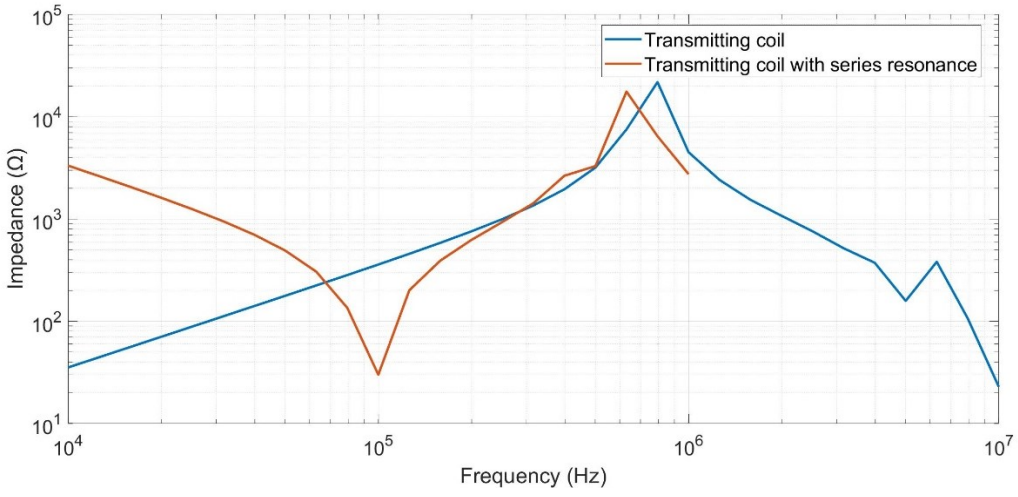

Figure 25. *Impedance of the non-differential transmitting coil as a function of frequency.*

The other two transmitting coils in the system are differential, consisting of two halves in size of 60 cm by 30 cm. They are wound with similar stranded wire than the non-differ-

ential transmitter, with outer diameter of 2.35 mm and 17 turns. Impedances of the differential transmitting coils are measured to be approximately 897 µH, and with power capacitor of 2.7 nF in series, the coils are resonated at 101 kHz. Information about each of the transmitting coils is concluded in Table 7. In the table, *Tx0* refers to the non-differential transmitting coil, while *Tx1* and *Tx2* refer to the differential transmitters. As the transmitting coils have power resistors of 0.1 Ω in series with them, it is possible to measure the voltage over the resistor at the measurement frequency 103 kHz and calculate the current flowing in the transmitting coil, which is also presented in Table 7.

Table 7. *Resonant frequencies of the transmitting coils and exciting current in them at the measurement frequency of 103 kHz.*

	$f_{resonance}$	**Current (RMS) at 103 kHz**
Tx0	97 kHz	0.5 A
Tx1	101 kHz	1.25 A
Tx2	101 kHz	1.25 A

As can be seen from Table 7, all of the transmitting coils are driven with a large current. However, the current could be increased further by tuning the resonant frequency of the transmitting coils to be closer to the measurement frequency, 103 kHz. This is also why the differential transmitters are driven with larger current than *Tx0*, as the frequency used is closer to their peak value.

5.2.2 Receiving coils

There are 6 differential receiving coils in the system. All of them consist of two halves in size of 30 cm by 20 cm, and they are wound with an enamel wire with diameter of 0.2 mm. The coils contain 15 turns of wire, in order to increase the natural resonant frequency of them to about 1 MHz. Selecting the number of turns in the transmitting and receiving coils is rather challenging. Adding more turns increases the induced voltage in the coil, which is a desired situation. However, with more turns in the coil, the natural resonant frequency of the coil decreases. That is why for the receiving coils, it is needed to optimize the resonant frequency to be large, in other words, far away from the measurement frequency 103 kHz. This is also seen from Figure 26, where impedance of one of the receiving coils is presented. The measurement frequency 103 kHz is within the linear region of the impedance curve where response of the system is inductive, and therefore suitable for measurements. Impedance curves of the other receiving coils are nearly identical to this one.

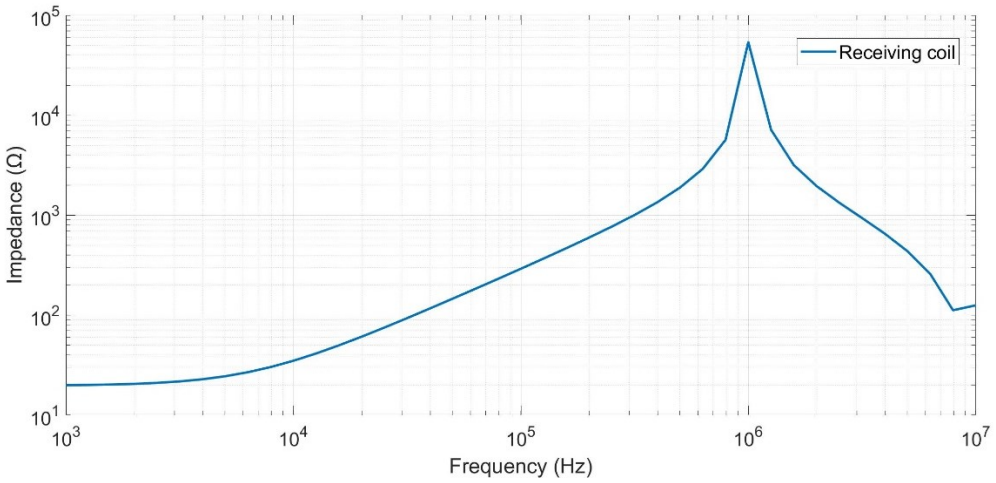

Figure 26. *Impedance of one of the differential receiving coils as a function of frequency. The measurement frequency 103 kHz is located at the linear region of the impedance graph.*

Now, as the natural resonant frequency of the receiver much higher than the used measurement frequency, it is possible to connect the receiver to a low-pass filter and reduce the amount of noise coupling to the receiver. This is further explained in section 5.2.4.

5.2.3 Final coil array

After winding both the transmitting and receiving coils and studying their resonant characteristics, the total coil array is put together. The coils are placed above each other, as demonstrated in Figure 27, with the difference that places of the differential transmitters and receivers are switched on the top and bottom of the array.

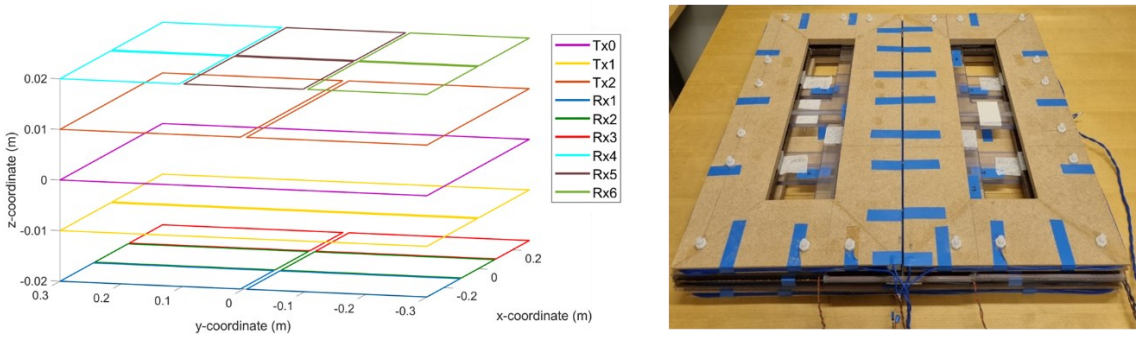

Figure 27. *A schematic of the final coil array and a picture of the constructed system.*

Changing the order of the transmitters and receivers is done to help the balancing process of the system. As mentioned, differential receiving coils are placed so that the “empty voltage” is as near as zero as possible. Since the coils are wound by hand, and may have some small differences in shape, they need to be moved slightly to find the position where nulling of the transmitting field takes place. However, as the receiving

coils need to be balanced both in reference to the non-differential transmitting coil and the differential transmitting coil, the challenge is to find a position where both cases are nulled as well as possible. In Table 8, voltages measured by the receiving coils when no marker is within the target space are presented.

Table 8. *Balanced voltages of the receiving coils when different transmitting coils are excited, and no marker is placed near the array.*

Receiver	Tx0	Tx1 (differential)	Tx2 (differential)
Rx1	0.64 V	6.75 V	-
Rx2	3.02 V	5.99 V	-
Rx3	2.49 V	12.8 V	-
Rx4	1.81 V	-	6.95 V
Rx5	1.19 V	-	7.50 V
Rx6	1.55 V	-	8.80 V

As can be seen from Table 8, the balanced voltages, when the differential transmitters are used, are larger than the ones with the non-differential transmitter. This is due to the resonance points of the Tx coils. Since the differential transmitters are driven with larger current, a larger voltage is measured with the receiving coils. The values that are missing from the table are coming from the coils that cannot be used as differential receivers with certain differential transmitting coils, as explained in section 5.1.1.

Another difference from the theoretical coil model is that because of the thick wires used, and properties of the materials of the coil frames, thickness of the whole coil array is approximately 6.5 cm. In the simulated model, thickness of the total system is only 4 cm because the coils do not have any volumetric properties. However, this should not have a large effect on the measurements. When the whole array is put together, the coils are connected to each other with plastic screws.

5.2.4 Electronics

As mentioned in the overview of the system, the main electronic parts, in addition to the coils themselves, are a power amplifier, an instrumentation amplifier, and a low-pass filter in the receiving end of the system. The total constructed front-end board can be seen from Figure 28.

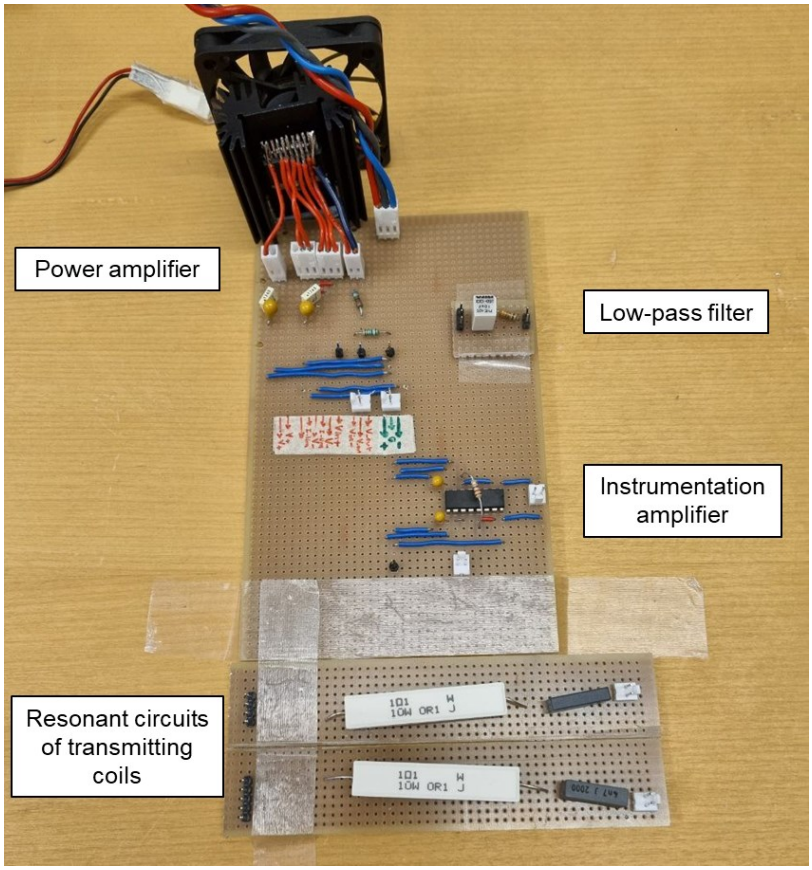

Figure 28. *Electronics of the localization system.*

The power amplifier, OPA549 from Texas Instruments, is selected for the system because of its capability of driving large current (8 A). In addition, the large slew rate (9 V/µs) makes it possible to use high frequency, 103 kHz, and still provide large exciting voltage for the transmitting coils. A schematic for the power amplifier circuit is presented in Figure 29.

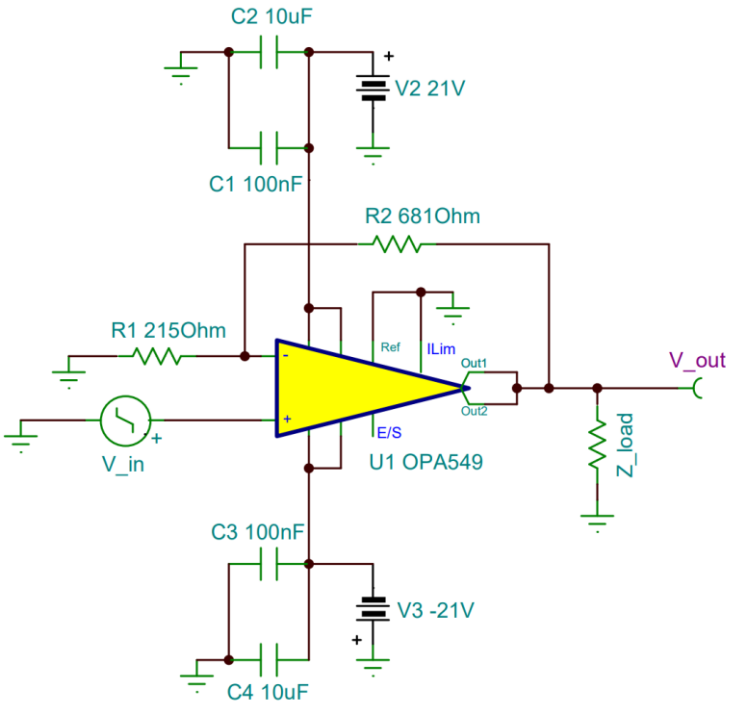

Figure 29. *Schematic of the power amplifier (OPA549).*

The power amplifier is connected to a heat sink to ensure that the component is not broken by too high temperature. In addition, a small fan is used to increase the heat transfer. The heat transfer system can be seen from Figure 28. There is a possibility to limit the output current of OPA549 with an external resistor, but in our system, the amplifier is driven to the maximum output current that it can provide for the transmitting coils with the selected frequency and gain. In the system, the power amplifier gain is set to

$$G = 1 + \frac{R_3}{R_2} = 1 + \frac{681\ \Omega}{215\ \Omega} \approx 4.17. \tag{38}$$

Hence, with the input voltage of 8 V peak-to-peak and supply voltage of ± 21 V, the output voltage provided is approximately 33 V peak-to-peak.

At the receiving end of the system, the first part of the electronics is the passive low-pass filter. It consists of a resistor of 33.8 Ω and a capacitor of 10 nF. As the natural resonant frequency of the receiving coil is approximately 1 MHz, the coil may pick up signals at this frequency. To prevent that, the cut-off frequency of the low-pass filter is set to 470 kHz. By using the filter, the signal of interest at 103 kHz is not attenuated, and the noise at higher frequencies is filtered out from the measured signal.

After filtering, the next part is the instrumentation amplifier, INA103 from Texas Instruments. It is a component with low noise level (1 nV/√Hz) , high slew rate (15 V/µs) and

large enough supply range (±9 V to ±25 V) to be able to measure the signals if the balancing of the coils is not perfect. Figure 30 shows schematic of the instrumentation amplifier.

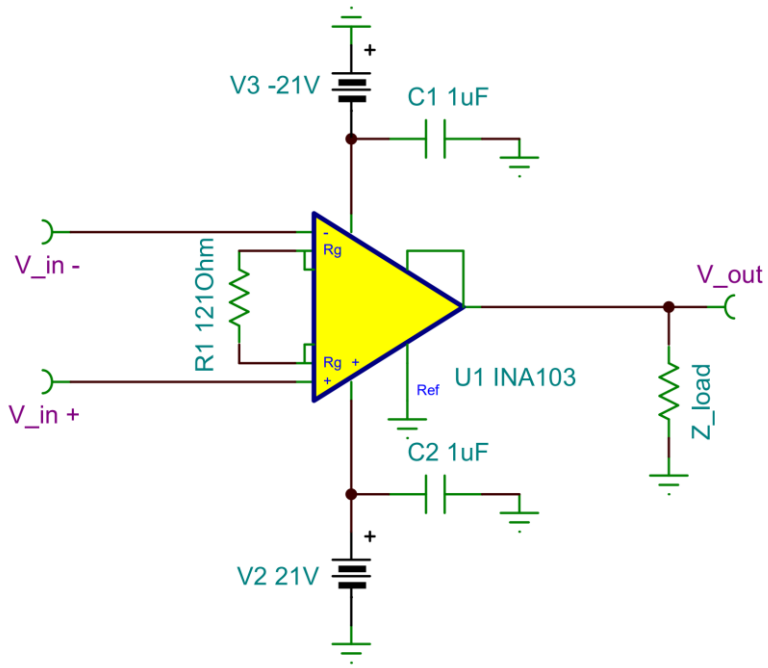

Figure 30. *Schematic of the instrumentation amplifier (INA103).*

Gain of the instrumentation amplifier is set with an external resistor. Value of the gain is

$$G = 1 + \frac{6\ k\Omega}{R_G} = 1 + \frac{6\ k\Omega}{121\ \Omega} \approx 51. \tag{39}$$

As shown in Table 8, the measured receiver voltages are around 0.6–13 V peak-to-peak when the gain of 51 is used. Hence, without the instrumentation amplifier, the measured voltages would be rather small, that is, in range of tens of millivolts. In addition, the instrumentation amplifier helps to reject the amount of common-mode signals coupling to the system. The instrumentation amplifier's output is monitored with the oscilloscope.

5.2.5 Marker

It is possible to detect different metallic objects with the system. For example, a metallic plate, large screws and large ferrite rods were first used to test if the system is giving any response. However, as the endoscopic capsule is small in size, small ferrite rods with resonant circuit around them are used as markers in the study. There are three markers that were successfully wound with enamel wire with diameter of 0.1 mm. The size of the ferrite rod used in two of the markers is 3 mm in diameter and 15 mm in length, and the initial permeability of the ferrite is 250. One of the markers, marker 3, is wound around

ferrite with diameter of 2 mm, length of 15 mm and permeability of 2300. Size of the marker should be small enough to be able to fit inside a regular endoscopic capsule. Figure 31 contains a picture of one of the markers, a schematic of the marker and the equivalent circuit of it.

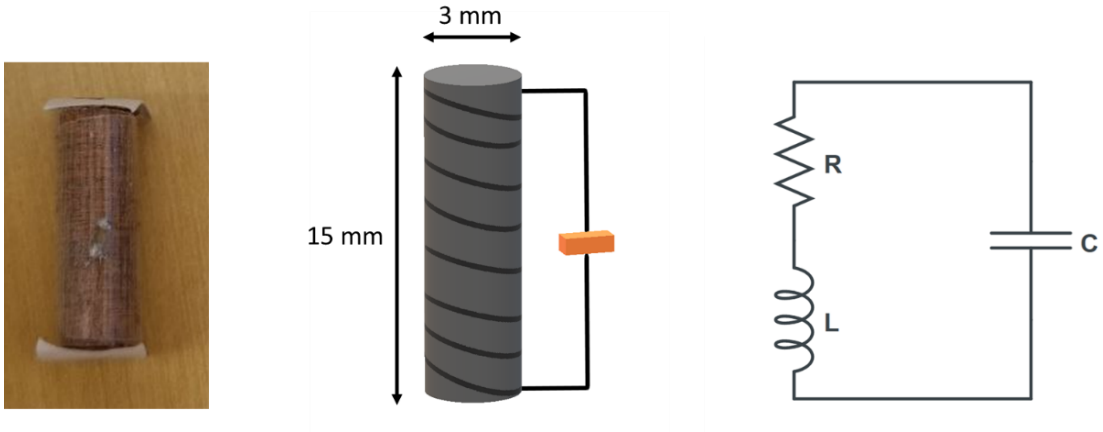

Figure 31. *A picture of a resonant LC marker, a schematic, and an equivalent circuit of that.*

The number of turns in each three markers and the resonant frequencies of them are seen from Table 9. As markers 1 and 2 are wound on different ferrite core than marker 3, the resonant frequencies of them are also varying and not only dependent on the number of turns. In general, the ones wound on the larger ferrite core turned out to be more durable and easier to handle.

Table 9. *Specifications of the LC markers.*

	Number of turns	$\mathbf{f_{resonance}}$
Marker 1	413	103 kHz
Marker 2	288	104 kHz
Marker 3	315	105 kHz

The markers are resonated by adding a capacitor in series with the coil that is wound around the ferrite rod. As can be seen from Table 9, marker 1 has resonant frequency that is closest to the ones of the transmitting coils (97 kHz and 101 kHz). In addition, it has the largest number of turns in it. Therefore, the experiments are performed with marker 1.

5.3 Results of the experiments

After connecting the coil array, electronics and measurement devices together, functionality of the system is tested with different positions and orientations of the marker, and the results are compared with simulated values. In Figure 32, the principles of positioning the marker with respect to the array are presented. At first, it is tested how the system works when the marker is positioned further away from the array, visualized as line a) in Figure 32. This way, the possibility to use the system for real life localization with different body sizes and types can be analyzed. Second, the marker is swept through one of the receiving coils at different depths from the array, according to line b), and the voltage is measured at each position. One receiving coil, *Rx4*, is selected for the measurements, and it is tested both with the non-differential and differential transmitters. In addition, the marker angle with respect to the array is changed during the measurements so that response of the system can be compared with the sensitivity analysis, and practicability of it in real life localization can be analyzed.

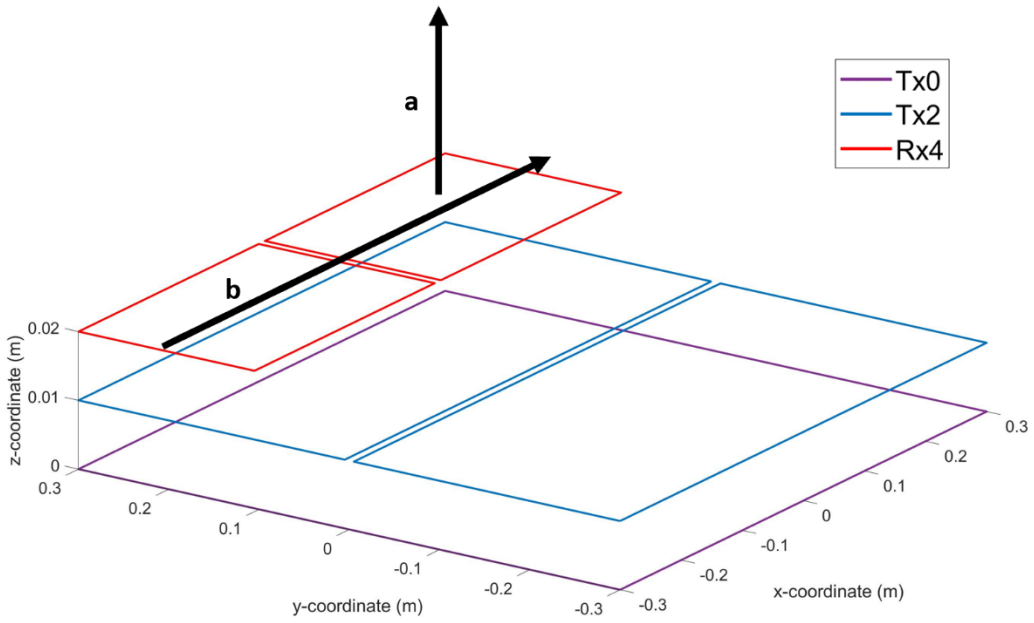

Figure 32. *Visualization of the basic measurements that are taken with the array: a) Positioning the marker further away from the array at certain xy-position and b) Sweeping the marker through a receiving coil at certain distances from the array. At each position, voltage at the receiving coil is measured.*

The depth measurement is done in the middle of one receiver half, starting from 5 cm from the array and moving to 25 cm depth from the array. In the measurements, the marker is aligned with the z-axis. This is the angle where the system should provide the maximum voltage, since the primary magnetic field is flowing though the solenoid cross-sectional area. The transmitting coil used is the differential *Tx2*. Figure 33 a) shows the

voltage difference signals caused by the marker. A moving average filter with span of 30 data points is used to smooth the signals. As can be seen, the amplitude of the voltage decreases as the marker is moved away from the array, as expected. When the distance is increased to 25 cm, the signal amplitude is decreased to approximately 0.05 V, and noise level of the signal is increased. This can be seen as a small deformation of the signal compared to the other ones. There is no phase difference in the measured sine waves, which is expected, because in the simulation of similar situation, phase of the voltage difference signal remained constant at 90 degrees.

In Figure 33 b), mean of the voltage amplitude is plotted against the depth. As can be seen, the signal follows quite well the modelled depth simulations seen in section 5.1.6. If distance of the marker from the array was further increased, measured voltage difference signal would probably become even more noisy, and the localization would get harder. Still, it is possible to measure voltage even at 25 cm which is supporting practicability of the system. However, this is achieved when the marker is in optimal angle with respect to the array.

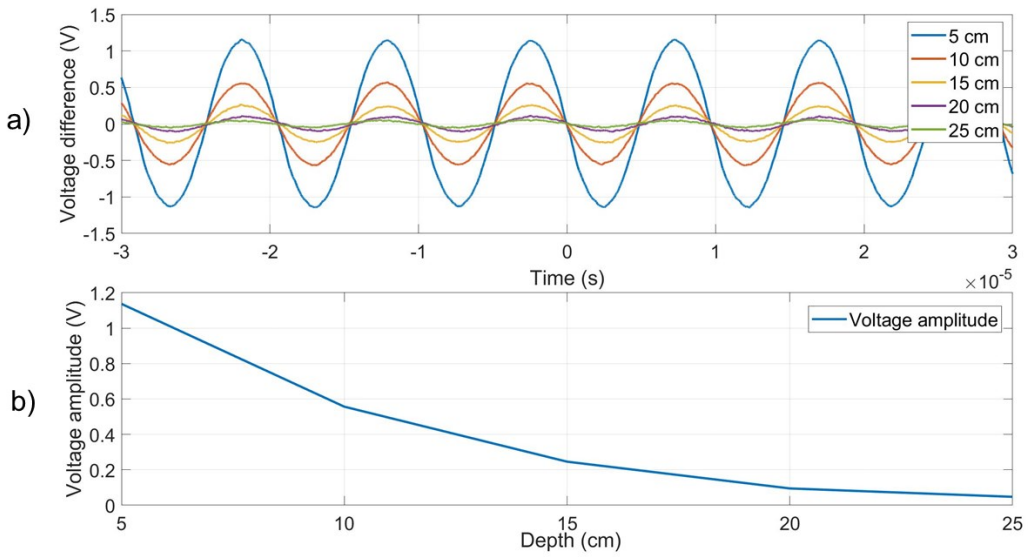

Figure 33. *Depth measurement with differential transmitter Tx2. The marker is moved away from the array at certain xy-position, and the voltage is measured at each point. a) Signals measured at depths from 5 cm to 25 cm from the array, b) Average amplitude of the signal as a function of depth.*

In Figure 34 a), the marker is swept across receiver *Rx4* at heights of 10 cm and 20 cm, and the voltage is measured at each position. The marker is again aligned with the z-axis. As can be seen, amplitudes of the signals support the results of the depth measurement. In addition, shape of the graph is typical for a differential coil: voltage reaches its maximum at the centers of coil halves, and in the middle of the coil, the voltage be-

comes zero. At 20 cm distance, the amplitude is decreased but the pattern is still noticeable. A similar graph is seen in Figure 34 b), where the same values are simulated with COMSOL. As can be seen, the simulated values are in range of millivolts, when the non-volumetric differential transmitting coil is excited with current of 1 A in the model. If the simulated values are multiplied by all of the factors that affect the induced voltage, they seem slightly large compared to the measured ones. Parameters that affect the induced voltage are: number of turns in the transmitting coil N_T, number of turns in the receiving coil N_R, excitation current of the transmitting coil I_T and gain used in the instrumentation amplifier G. For example, at 20 cm distance from the coil edge and depth of 10 cm, the simulated value converted into measured value would be

$$V_{measured} = V_{simulated} * N_T * N_R * I_T * G = 4.6 * 10^{-4}\, V * 17 * 15 * \frac{1.25}{\sqrt{2}} * 51 = 5.29\, V$$

As can be seen, the value seems to be approximately 10 times larger than the measured one. Multiple different factors could be causing this difference. First, the transmitting coil and the marker are not optimally resonated in the measurements, since the measurement frequency is differing from their resonant frequencies. In addition, properties of the marker differ from each other. The real-life marker has relative permeability of 250 and number of turns of 413, while the simulated marker has permeability of 3000 and 468 turns. Use of ferrite with larger permeability and more turns results in larger induced voltage. Also, the depth used in the measurements is determined from the surface of the topmost coil, making the actual depth approximately 13 cm. Based on the depth measurement, change of a few centimeters in depth causes the voltage to decrease significantly. By taking all of these factors into account, the measured values seem reasonable both in magnitude and sign.

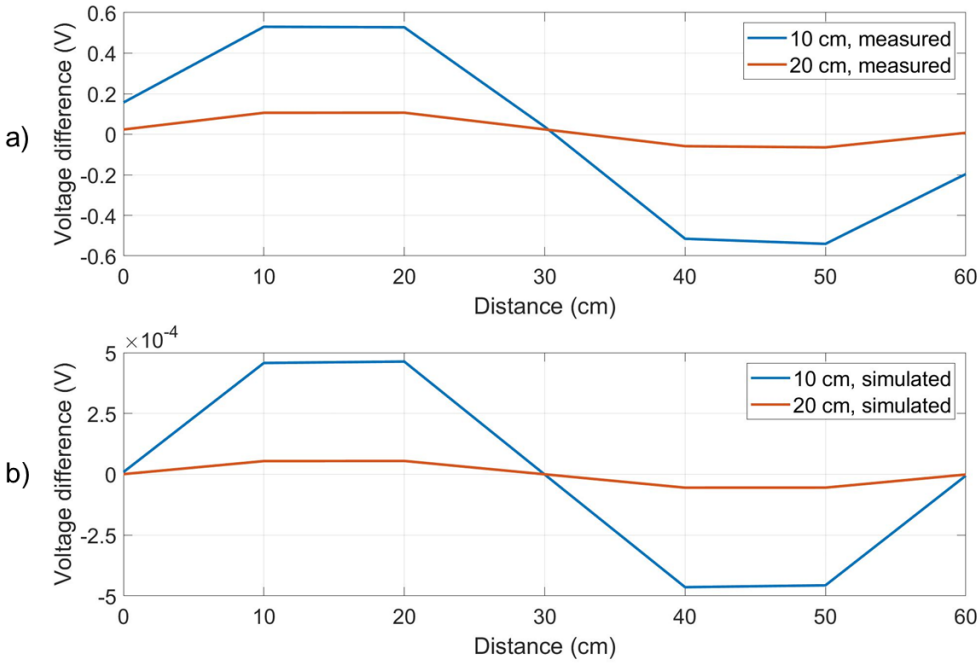

Figure 34. *a) Measured and b) simulated voltages caused by a marker that is placed at different positions across a receiving coil at two depths. The marker is oriented along the z-axis.*

Now, the marker angle with respect to the array is changed and the differential transmitter *Tx2* is still used as an excitation source. In Figure 35 a), the marker is swept across *Rx4* at 10 cm height, and the marker is kept at 45 degrees angle to x- and y-axes, and 90 degrees to z-axis. When the marker is placed in 90 degrees angle to z-axis, excitation of the marker becomes challenging because of the dead angle problem. However, the use of differential arrangement both in Tx and Rx should help the situation by producing fields in multiple directions. Figure 35 b) shows the simulated voltage for comparison. Some differences between the two can be noticed. The built system gives the largest response at the edges of the array because the field is twisted around the coil edges there. The response is rather symmetrical, and small voltages are also seen at 10 cm, 40 cm and 50 cm points. However, even the largest values seen on the edges are smaller than the ones for marker aligned with the z-axis, shown in Figure 34. This is because of the non-optimal orientation of the marker compared to the fields. The simulation shows near symmetrical response of the halves, but some small differences are seen there also. This might be caused by non-optimal meshing of the simulated space.

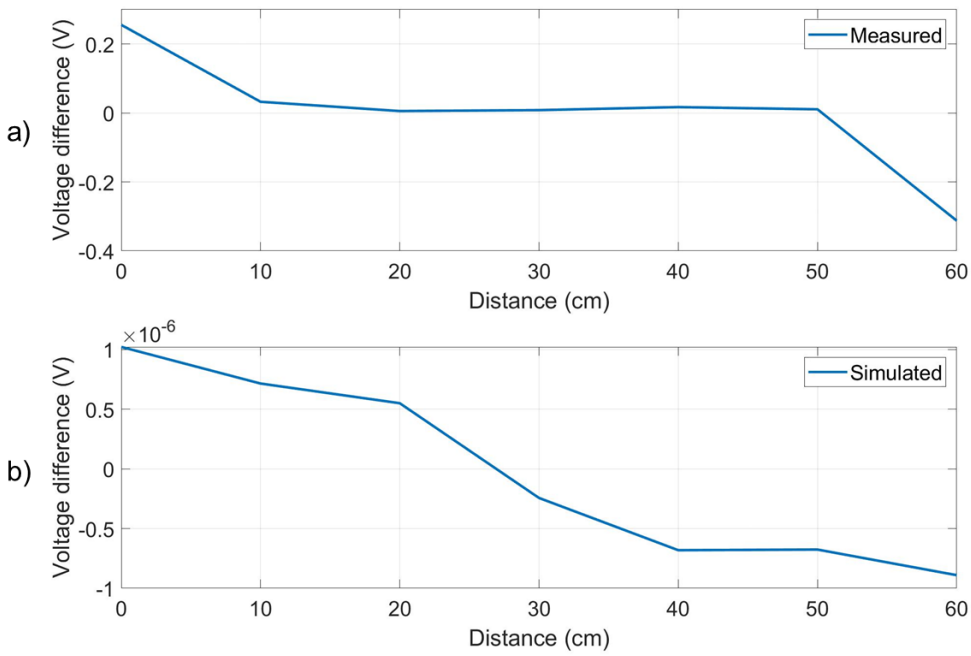

Figure 35. *a) Measured and b) simulated voltages caused by a marker that is placed at different positions across a receiving coil at depth of 10 cm. The marker is oriented 45 degrees to x- and y-axes, and 90 degrees to z-axis.*

Now, the marker is aligned with the y-axis and placed 90 degrees with respect to the z-axis, and the same sweeping measurement is performed at 10 cm height. This should make the localization even harder than with the previous 45 degrees angle. Figure 36 a) and b) show the measured and simulated voltages. The simulated values show a similar phenomenon that was seen in Figure 34 which is expected for a differential receiver coil. Similar shape can be also noticed from the measured values. However, amplitudes are rather small compared to the previous measurements, and the graph is not crossing zero at any point as it should, based on the simulated values, i.e., there is an offset. As the marker is aligned with the y-axis, it is probably excited somehow efficiently based on field figures shown in section 5.1.1. The problem may be caused by the production of secondary field from the marker, and the way it is coupling to the receiving coil, as the marker is now aligned with the y-axis, which is also orientation of the receiving coil's crossing line. Therefore, the voltage difference signal becomes noisy and cannot be analyzed correctly.

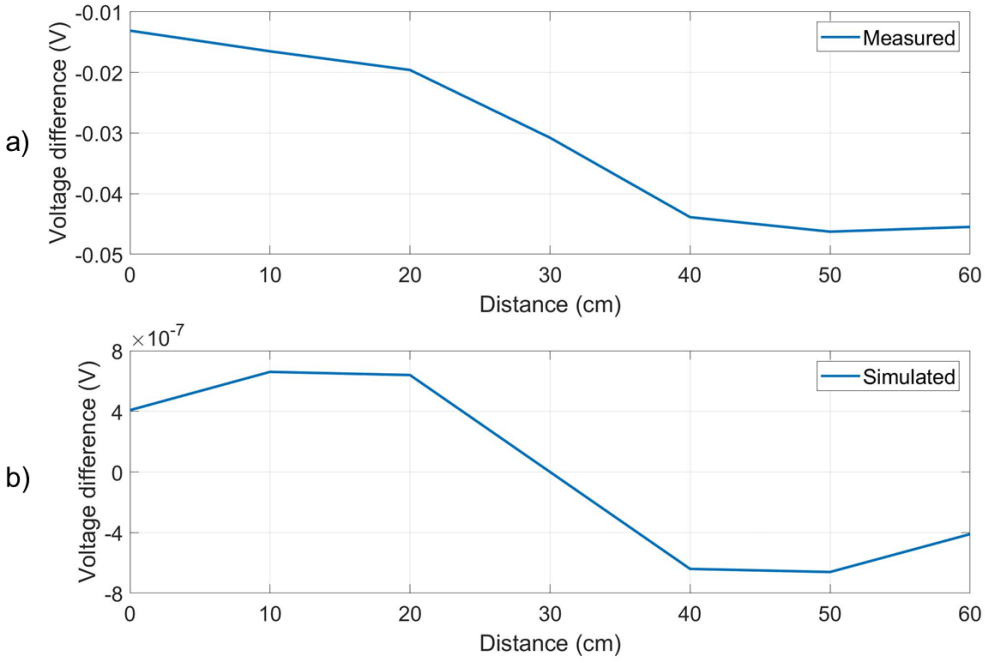

Figure 36. *a) Measured and b) simulated voltages caused by a marker that is placed at different positions across a receiving coil at depth of 10 cm. The marker is oriented along the y-axis, and 90 degrees to z-axis.*

Reason for the small measured voltage values when the marker is aligned with the y-axis can be also noticed from the sensitivity plot of the array at 10 cm height, shown in Figure 37. Now, the interesting component is *xx* because the field flowing through the marker should be at this direction to properly excite the marker. There is a large area with approximately zero sensitivity in the xx-component at this depth. This area is also aligned with the path along which the marker is positioned, making the localization evenly challenging at each position of its tract.

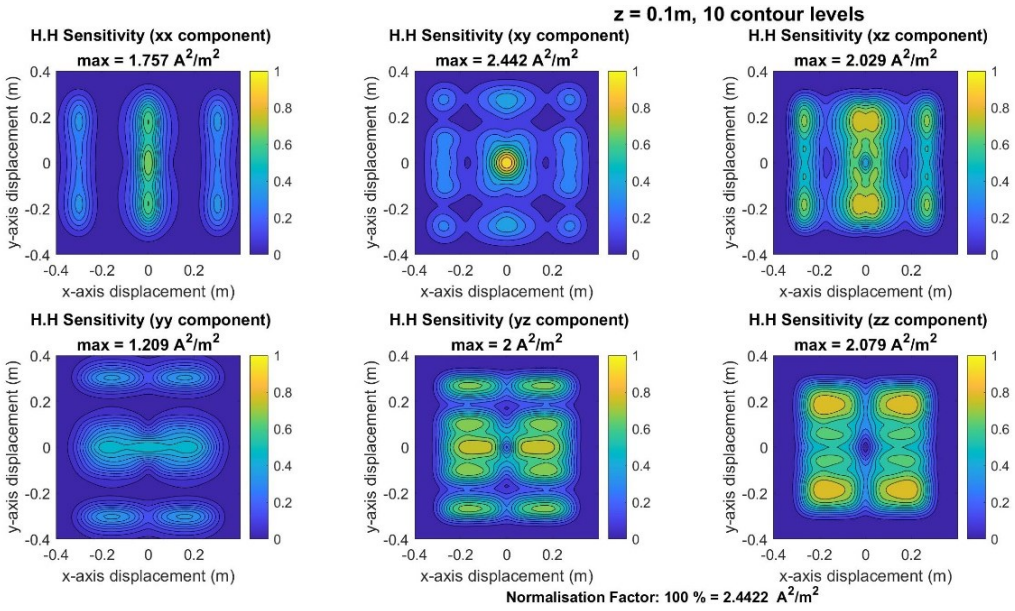

Figure 37. *Sensitivity maps of the coil array, on xy-plane at height of 10 cm from the coil array. The components are calculated using the dipole model approximation.*

The last tested orientation of the marker is aligned with the x-axis, and laying 90 degrees to the z-axis. The array is giving a large response on the edges of the array which can be seen from Figure 38 a). The graph is not crossing zero correctly in the middle of the array either in this measurement set. However, a voltage difference between the receiving coil halves can be noticed from the graph, and the voltages seem quite symmetrical also in the middle of the array. However, amplitudes of the voltage are rather small in the middle of the array.

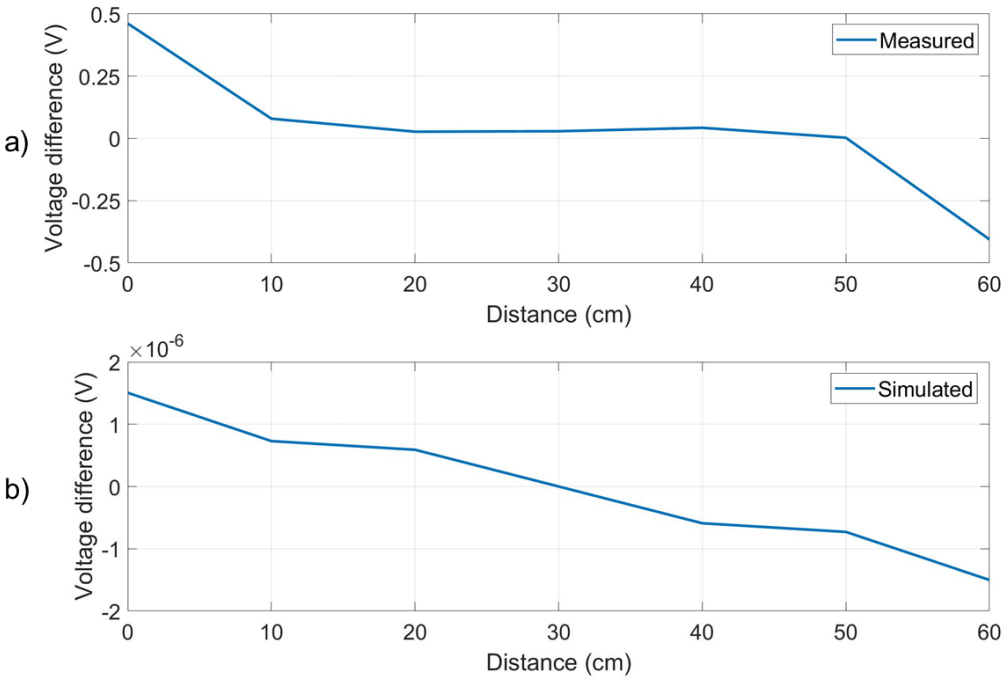

Figure 38. *a) Measured and b) simulated voltages caused by a marker that is placed at different positions across a receiving coil at depth of 10 cm. The marker is oriented along the x-axis, and 90 degrees to z-axis.*

The simulated values in Figure 38 b) are again symmetrical. Values on the edges of the array are simulated to be approximately 1.5 times larger than the corresponding values in Figure 35 where the marker was oriented 45 degrees to both x- and y-axes. Similar phenomenon can be seen from the measured values. The reason for this is that the curled magnetic field of the Tx coil edge is directed mostly along the x-axis at this distance from the coil array, causing more efficient excitation of the marker than with the 45 degrees situation.

To show the effect of using multiple transmitting coils, a few example measurements are performed with the non-differential *Tx0*. When the depth measurement and sweeping

across the receiver measurements are performed with *Tx0,* the measured voltages are smaller, as expected, based on the smaller exciting current of the non-differential *Tx0*. The depth measurement is visualized in Figure 39 a). As the current-ratio between the differential and non-differential coils is 1.25 A/0.5 A = 2.5, it can be noticed that the measured voltage amplitudes follow this ratio rather well. It can be seen that the measured signals are noisier than with the differential *Tx2* because of the weaker magnetic field produced by *Tx0.* In Figure 39 b), measured signals at 20 cm and 25 cm distances from the array are shown in larger scale, and it is noticed that they are rather noisy. However, the sinusoidal signal is still seen in both of them.

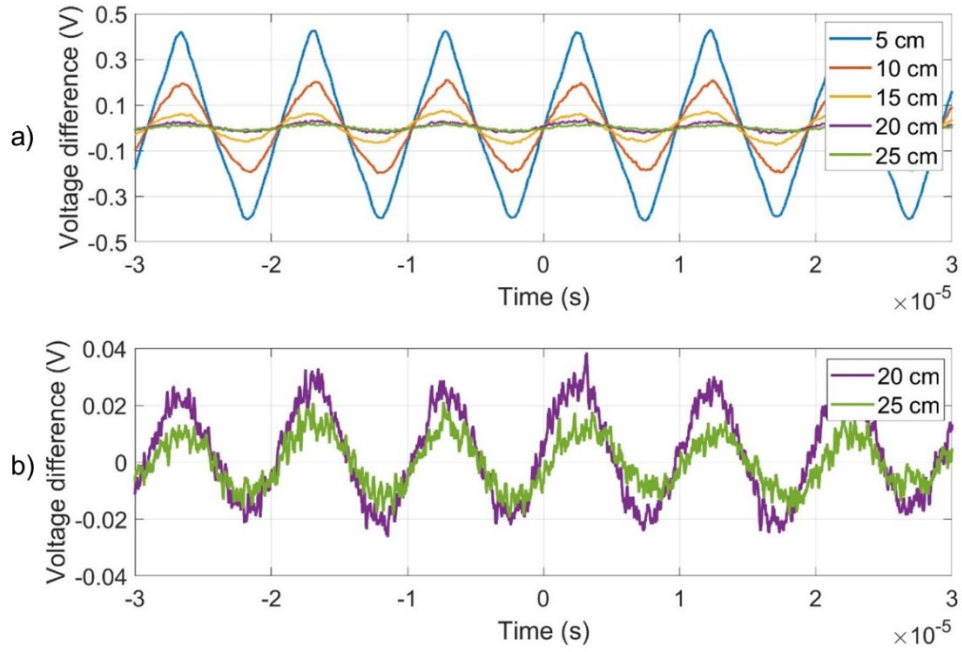

Figure 39. *Depth measurement with the non-differential transmitter Tx0. The marker is placed at different depths from the array at certain xy-position, and the voltage is measured at each point. The marker is oriented along the z-axis. a) Signals at depths from 5 cm to 25 cm. b) Enlarged version of the 20 cm and 25 cm signals.*

In Figure 40 a) and b), examples of two other measurements with *Tx0* are shown. In figure 40 a), the marker is swept across receiver *Rx4* at two depths, and voltage is measured at each position while the marker is aligned with the z-axis. In Figure 40 b), the marker is swept across receiver *Rx4* at 10 cm depth, and it is oriented along the x-axis and 90 degrees to z-axis.

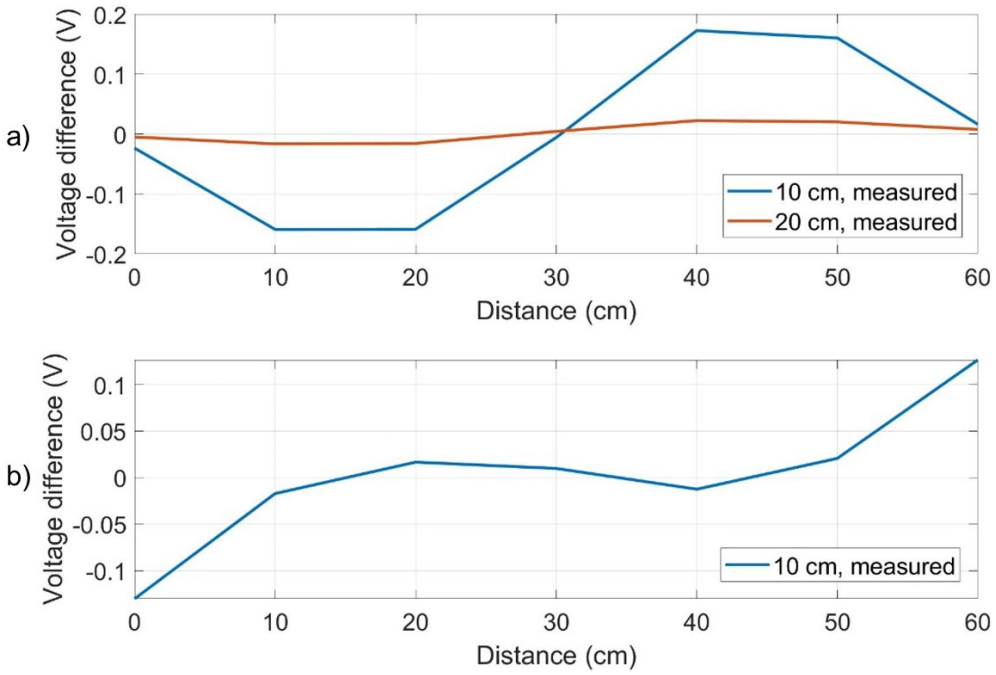

Figure 40. *Measured signals when the non-differential transmitter Tx0 is used. a) Marker is placed at positions across a receiving coil at depths of 10 cm and 20 cm. The marker is aligned with the z-axis. b) Marker is placed at positions across a receiving coil at depth of 10 cm, while it is oriented along x-axis and 90 degrees to z-axis.*

As can be seen from Figure 40 a), the signals have again the expected shape for a differential receiver, and the amplitudes are in line with the depth measurement. In Figure 40 b), the effect of using multiple transmitters is shown. The measured signal is rather symmetrical and shows reasonable voltages. As the amplitudes of measured voltages with the differential transmitter *Tx2* and this orientation of the marker were quite small, it is possile use information gathered from the other measurement channels for the inversion.

6. DISCUSSION

In this thesis, the aim was to design an electromagnetic coil array for wireless capsule endoscope (WEC) localization. Magnetic field strength -based localization method was found to be the most promising one based on a literature review. The method applies electromagnetic induction and use of coils for detecting the capsule's location and orientation. To design a system that could be placed inside a hospital bed and used together with capsule steering system in the future, four planar coil arrays were designed and compared by means of modelling and sensitivity analysis, and one of them was selected for experimental study. Additionally, an optimal target type to place inside a capsule endoscope was found by FEM-based modelling: a resonated solenoid with ferrite core. The system was built and equipped with electronics and measurement devices, and two channels of the system were utilized for testing, that is, measured voltages at different positions and orientations of the marker were compared with simulated results. Now, the experimental results, used methods and ways to improve the system are discussed.

In general, the measured values seem to be consistent with the simulated ones. Similar symmetrical patterns can be seen from both, and amplitudes of the values are increasing and decreasing approximately with the same ratio. When the non-differential transmitting coil is used, the measured values are showing similar phenomenon than with the differential transmitter. It is possible to use different combinations of the receiving and transmitting coils to help the inversion at different positions and orientations.

Clear voltage signals can be measured when the marker is aligned with the axis of the coils, that is, when the exciting primary field can penetrate the LC marker's solenoid optimally. In our case, this is when the marker is aligned with the z-axis. This was also seen from the sensitivity analysis. When the marker is placed in 90 degrees angle with respect of the z-axis, the situation is different. [39,43] This is the most challenging orientation for the system, and that is why it was tested. Three different variants of this orientation show that the measured voltages get rather small, especially in the middle of the array, where the patient would potentially be located. However, the system shows some measurable voltages at the distance of 10 cm from the array. The only orientation that does not show reasonable values is the one with marker aligned with the y-axis. If the distance of the marker from the array was further increased, the measured voltage would decrease and probably become not detectable with this first prototype of the system.

Based on the analysed sensitivity maps of the design, especially the xx- and yy-components have large areas with very small sensitivity, and therefore they should be further improved. This should also increase the measured voltages at challenging orientations.

There are multiple ways how the current system could be improved. For instance, the system could have even more channels to make sure that there are as many successful measurements to use in the inversion as possible. For example, if balancing of some of the coils was poorer than in others, there would be additional measurements to use. The current balancing of the coils was done carefully, by moving a receiver coil slightly and measuring how it affects the empty voltages in reference to each of the transmitters. However, the balancing could be improved by continuing this process, or by adding turns of wire to some of the coils to balance the fields. One differential receiving coil at the edge of the array, *Rx4,* was selected to perform as an example measurement coil in the experiments. As shown in Table 8, some receivers were balanced better than the others. Balanced voltages of *Rx4* are approximately on the average level of all receivers which makes it a good example channel. If the balancing was further improved, the dynamic range of the measurement devices could be devoted to only measure the voltage caused by the marker and not the one coupling from the transmitting coils. Therefore, the system's operation could be enhanced.

Another way to improve performance of the system is to match the resonant frequencies better. In this prototype of the system, it was possible to resonate the transmitters at 97 kHz and 101 kHz, and the marker at 103 kHz. By modifying the resonant capacitor values or by taking a few turns of from the marker, it is possible to resonate all three coils at the same frequency. This way, also the transmitting coils would be excited at their resonance point, and therefore with larger current. This would improve the systems performance because the magnetic fields generated would be larger in magnitude and reach deeper in the target space.

In addition, resonance of the receiving coils is one option to utilize in the system. During the development of this version of the system, the receiving coils were tested to be resonated the same way as the marker, with parallel resonance. It was noticed that the generated voltages were increased, and no low-pass filter was needed after the receiving end because the receivers pick out only their resonant frequency. However, to match both the receiver's resonant frequency and aforementioned transmitter's and marker's resonant frequencies would get rather challenging. In addition, as there may be small differences in the inductances of the six receivers, resonating all of them at the same

frequency would possibly be quite difficult. Therefore, resonance of the receivers was left out from this version of the design.

Three different solenoid markers were successfully wound in the building phase of the system. The one selected had resonant frequency closest to the ones of transmitters, and the most turns in it. However, it would be possible to produce more efficient marker that would have even more turns in it or different type of core. For instance, properties of the marker could be modified by increasing the permeability of the ferrite.

One advantage of the built system is that it does not require any special equipment. All measurements were performed with basic measurement devices, and electronics contained amplifiers that are common in many medical applications. If the prototype was developed into a continuous localization system, there would still be a few things that need to be considered. Firstly, an automatic data acquisition needs to be connected to the array so that processes like switching between receivers and excited transmitters, signal conditioning and data processing would become automatic. Secondly, the system requires an inversion algorithm that estimates location of the marker based on the measured voltage values. There are multiple algorithms available that have been tested in similar applications [61]. In order to invert the marker position and orientation even at large depths and problematic angles seen in the measurements, the signal conditioning system should be rather effective. Additionally, as the power amplifier generates heat when it excites the transmitters, and movement of the endoscopic capsule through the GI-tract takes hours, the heat transfer system should be more effective if the process became continuous. However, that affects only the electronics and does not cause heating of the patient or the bed. Also, as the system is to be used with steering module in the future, that will decrease also the time required for the procedure.

When the system has been tested with an inversion algorithm, some challenges may arise from embedding of the marker into a WEC since the capsule itself contains metallic parts inside it. Therefore, cooperation of functions of the capsule and localization should be ensured. Also, one possibility is to use the RF-module of the capsule to roughly solve the location and orientation, and to use this information as initial estimated values for the inversion algorithm. The designed prototype could be also harnessed to charge the capsule wirelessly, or similar system could be even used for the active locomotion. The discussed advantages, challenges and possible improvements are concluded in Table 10.

Table 10. *Summary of the advantages, challenges and possible improvements of the system.*

Advantages	• Planar geometry of the array • Relatively high sensitivity • Use of differential coils: Better utilization of dynamic range of the measurement devices, ability to resist distant noise sources • Small target that could be fit inside a capsule • When aligned with the exciting fields, the system gives a measurable response even at depth of 25 cm from the array
Challenges	• Balancing of the receivers • Dead angle challenge • Effect of embedding the marker inside the capsule is unknown
Possible improvements	• Improving balance of the receivers • Matching of the resonant frequencies of transmitters and marker • Exciting the transmitters with larger current • Resonating the receiving coils • Marker: Increasing the number of turns, using ferrite with larger permeability • Parts to add to the measurement system: Channel switching unit, data acquisition, inversion algorithm, signal conditioning, heat transfer unit

If an elevated version of this type of localization system was operated in hospital environment, interference from magnetic materials and different medical devices should be investigated properly. For example, the system should probably be used with a hospital bed without any metallic components. Rather expensive possibility would be to isolate the system from the hospital environment, for example, by using shielding around the device and the target space. Another point that needs to be taken into account when developing the system is the competition with conventional endoscopy and currently used capsule endoscopy without any additional localization functions. The conventional procedure is rather quick and easy, and during capsule endoscopy, the patient can usually go home and continue their day normally. Localization system incorporated into a hospital bed would require the patient to lay down for several hours if the capsule's speed cannot be increased robotically. However, one possibility is that the patient would visit the localization center when the capsule is estimated to be close to the area of interest in the GI tract. Also, when technology of the steering modules developes, the duration of capsule endoscopy is decreased. Therefore, the main application of this design is to be used together with the steering module.

7. CONCLUSIONS

In this thesis, the possibility to use electromagnetic tomography in localization of wireless capsule endoscopes (WECs) was studied. The aim was to model and develop an electromagnetic coil array that could be utilized for the localization purposes. As was noticed based on a literature review, a few challenges are still preventing the technology of WECs to reach its future prospects, one of the most essential challenge being the determination of the capsule's pose. Therefore, the current state of art in WEC localization was studied and analysed. Based on comparison of different techniques, active magnetic field strength -based localization method was selected for modelling and practical testing. It provides high accuracy and does not suffer from weakening of the fields when passing through a human body. A table comparing the methods and their advantages and limitations is found from section 2.2.4.

Four different planar electromagnetic coil arrays were designed and modelled both in COMSOL Multiphysics and MATLAB. The aim was to design such an array that could be placed inside a hospital bed, and possibly be used together with a steering system in the future. By using the sensitivity formulation that utilizes dot product of the magnetic fields, one of the four modelled coil arrays was selected for building and testing. In addition to the coil arrays, different markers that could be fitted inside a capsule were modelled in COMSOL Multiphysics, and the one providing the largest response was implemented in real life. In addition, the whole coil array system with the coils themselves, electronics and measurement devices was constructed.

The coil array system was designed and demonstrated to be able to operate with the small, resonated, ferrite cored solenoid sample. It was possible to measure clear voltage signal caused by the marker even at depth of 25 cm from the system when the marker was oriented along the excitation field. Some difficulties were noticed when the marker's orientation became challenging for the excitation fields to reach. Though, it seems that the system would be able to solve location of the capsule if the orientation of it remained somehow aligned with the field's direction. In order to make the system operational at each orientation of the marker, some improvements are needed. However, the system contains many channels, and the measurements from other channels can help to estimate the voltage caused by the marker even at the challenging orientations seen in the results section. In addition, the system requires an inversion algorithm that estimates the capsule's pose based on the measured voltages.

REFERENCES

1. Iddan G, Meron G, Glukhovsky A, Swain P. Wireless capsule endoscopy. Nature (London). 2000, Vol. 405(6785), p. 417.

2. Shamsudhin N, Zverev VI, Keller H, Pane S, Egolf PW, Nelson BJ, et al. Magnetically guided capsule endoscopy: Medical Physics. 2017, Vol. 44(8), pp. 91–111.

3. Bianchi F, Masaracchia A, Shojaei Barjuei E, Menciassi A, Arezzo A, Koulaouzidis A, et al. Localization strategies for robotic endoscopic capsules: a review. Expert review of medical devices. 2019, Vol. 16(5), pp. 381–403.

4. Chetcuti Zammit S, Sidhu R. Capsule endoscopy - Recent developments and future directions. Expert review of gastroenterology & hepatology. 2021, Vol. 15(2), pp. 127–137.

5. Medtronic. PillCam™ Capsule Endoscopy Platform [Internet]. [cited 2023 Jan 5]. Available from: https://endoscopyonair.com/wp-content/uploads/2021/06/PillCam-Capsule-Endoscopy-Platform.pdf

6. Video Capsule Endoscopy [Internet]. [cited 2022 Jan 5]. Available from: https://www.gutworks.com.au/video-capsule-endoscopy-murdoch-perth/

7. Umay I, Fidan B, Barshan B. Localization and tracking of implantable biomedical sensors. Sensors (Switzerland). 2017, Vol. 17(3), p. 583.

8. Given Imaging. PillCamTM Capsule Endoscopy, User Manual [Internet]. 2016 [cited 2023 Jan 6]. Available from: https://www.pillcamcrohnscapsule.eu/assets/pdf/DOC-2928-02-PillCam-Desktop-SWv9UMEN.pdf

9. Rînja E, Ilie M, Șandru V, Diaconu I, Hortopan A, Constantinescu G. The role of capsule endoscopy in the diagnosis of digestive haemorrhage. Archives of the Balkan Medical Union: the official journal of the Balkan Medical Union. 2018, Vol. 53(3), pp. 434–438.

10. Lohsiriwat V. Colonoscopic perforation: Incidence, risk factors, management and outcome. World journal of gastroenterology. 2010, Vol. 16(4), pp. 425–430.

11. Wiggins TF, Khan AS, Winstead NS. Sedation, Analgesia, and Monitoring. Clinics in colon and rectal surgery. 2010, Vol. 23(1), pp. 14–20.

12. Cancer Research UK. Diagram showing an endoscopy. [Internet]. 2014 [cited 2023 Jan 5]. Available from: https://commons.wikimedia.org/wiki/File:Diagram_showing_an_endoscopy_CRUK_098.svg

13. Limpias Kamiya KJL, Hosoe N, Hayashi Y, Kawaguchi T, Takabayashi K, Ogata H, et al. Video capsule endoscopy in inflammatory bowel disease. DEN open. 2022, Vol. 2(1), p. 26.

14. Valdivia PC, Robertson AR, De Boer NKH, Marlicz W, Koulaouzidis A. An overview of robotic capsules for drug delivery to the gastrointestinal tract. Journal of clinical medicine. 2021, Vol. 10(24), p. 5791.

15. Furumoto Y, Araki A, Matsumoto T, Nozaka T, Yauchi M, Kobayashi K, et al. Experience of disruption of capsule endoscopy after prolonged retention. DEN open. 2022, Vol. 2(1), p. 57.

16. Shao G, Guo YX. Hybrid Wireless Positioning and Charging With Switched Field Helmholtz Coils for Wireless Capsule Endoscopy. IEEE transactions on microwave theory and techniques. 2020, Vol. 68(3), pp. 904–913.

17. Pennazio M, Spada C, Eliakim R, Keuchel M, May A, Mulder CJJ, et al. Small-bowel capsule endoscopy and device-assisted enteroscopy for diagnosis and treatment of small-bowel disorders: European Society of Gastrointestinal Endoscopy (ESGE) Clinical Guideline. Endoscopy. 2015, Vol. 47(4), pp. 352–376.

18. Rondonotti E, Spada C, Adler S, May A, Despott EJ, Koulaouzidis A, et al. Small-bowel capsule endoscopy and device-assisted enteroscopy for diagnosis and treatment of small-bowel disorders: European Society of Gastrointestinal Endoscopy (ESGE) Technical Review. Endoscopy. 2018, Vol. 50(4), pp. 423–446.

19. Soffer S, Klang E, Shimon O, Nachmias N, Eliakim R, Ben-Horin S, et al. Deep learning for wireless capsule endoscopy: a systematic review and meta-analysis. Gastrointestinal endoscopy. 2020, Vol. 92(4), pp. 831–839.

20. Ding Z, Shi H, Zhang H, Meng L, Fan M, Han C, et al. Gastroenterologist-Level Identification of Small-Bowel Diseases and Normal Variants by Capsule Endoscopy Using a Deep-Learning Model. Gastroenterology (New York, NY 1943). 2019, Vol. 157(4), pp. 1044–1054.

21. Mateen H, Basar R, Ahmed AU, Ahmad MY. Localization of Wireless Capsule Endoscope: A Systematic Review. IEEE Sensors Journal. 2017, Vol. 17(5), pp. 1197–1206.

22. Liu X, Liu Z, Li Y, Zhao P, Wang J. Research on Direct 3D Electromagnetic Tomography Technique. IEEE Sensors Journal. 2020, Vol. 20(9), pp. 4758–4767.

23. Ye Y, Swar P, Pahlavan K, Ghaboosi K. Accuracy of RSS-Based RF Localization in Multi-capsule Endoscopy. International journal of wireless information networks. 2012, Vol. 19(3), pp. 229–238.

24. Li S, Geng Y, He J, Pahlavan K. Analysis of three-dimensional maximum likelihood algorithm for capsule endoscopy localization. In: 2012 5th International Conference on BioMedical Engineering and Informatics. IEEE; 2012, pp. 721–725.

25. Wille A, Broll M, Winter S. Phase difference based RFID navigation for medical applications. In: 2011 IEEE International Conference on RFID. IEEE; 2011, pp. 98–105.

26. Hou J, Zhu Y, Zhang L, Fu Y, Zhao F, Yang L, et al. Design and Implementation of a High Resolution Localization System for In-Vivo Capsule Endoscopy. In: 2009 Eighth IEEE International Conference on Dependable, Autonomic and Secure Computing. IEEE; 2009, pp. 209–214.

27. Khan UI, Pahlavan K, Makarov S. Comparison of TOA and RSS based techniques for RF localization inside human tissue. In: 2011 Annual International Conference of the IEEE Engineering in Medicine and Biology Society. United States: IEEE; 2011, pp. 5602–5607.

28. Nafchi AR, Goh ST, Reza Zekavat SA. Circular Arrays and Inertial Measurement Unit for DOA/TOA/TDOA-Based Endoscopy Capsule Localization: Performance and Complexity Investigation. IEEE sensors journal. 2014, Vol. 14(11), pp. 3791–3799.

29. Bao G, Mi L, Geng Y, Zhou M, Pahlavan K. A video-based speed estimation technique for localizing the wireless capsule endoscope inside gastrointestinal tract. In: 2014 36th Annual International Conference of the IEEE Engineering in Medicine and Biology Society (EMBC). New York: IEEE; 2014, pp. 5615–5618.

30. Bao G, Pahlavan K, Mi L. Hybrid Localization of Microrobotic Endoscopic Capsule Inside Small Intestine by Data Fusion of Vision and RF Sensors. IEEE sensors journal. 2015, Vol. 15(5), pp. 2669–2678.

31. Liu SL, Kim J, Kang B, Choi E, Hong A, Park JO, et al. Three Dimensional Position Recognition of a Magnetic Capsule Endoscope by using Alternative Magnetic Signal. In: 2020 8th IEEE RAS/EMBS International Conference for Biomedical Robotics and Biomechatronics (BioRob). IEEE; 2020, pp. 316–321.

32. Son D, Yim S, Sitti M. A 5-D Localization Method for a Magnetically Manipulated Untethered Robot Using a 2-D Array of Hall-Effect Sensors. IEEE/ASME transactions on mechatronics. 2016, Vol. 21(2), pp. 708–716.

33. Hu C, Li M, Song S, Yang W, Zhang R, Meng MQH. A Cubic 3-Axis Magnetic Sensor Array for Wirelessly Tracking Magnet Position and Orientation. IEEE Sensors Journal. 2010, Vol. 10(5), pp. 903–913.

34. Hu C, Ren Y, You X, Yang W, Song S, Xiang S, et al. Locating Intra-Body Capsule Object by Three-Magnet Sensing System. IEEE sensors journal. 2016, Vol. 16(13), pp. 5167–5176.

35. Shao G, Tang Y, Tang L, Dai Q, Guo YX. A Novel Passive Magnetic Localization Wearable System for Wireless Capsule Endoscopy. IEEE sensors journal. 2019, Vol. 19(9), pp. 3462–3472.

36. Di Natali C, Beccani M, Valdastri P. Real-Time Pose Detection for Magnetic Medical Devices. IEEE transactions on magnetics. 2013, Vol. 49(7), pp. 3524–3527.

37. Di Natali C, Beccani M, Simaan N, Valdastri P. Jacobian-Based Iterative Method for Magnetic Localization in Robotic Capsule Endoscopy. IEEE transactions on robotics. 2016, Vol. 32(2), pp. 327–338.

38. Xu Y, Li K, Zhao Z, Meng MQH. A Novel System for Closed-Loop Simultaneous Magnetic Actuation and Localization of WCE Based on External Sensors and Rotating Actuation. IEEE transactions on automation science and engineering. 2021, Vol. 18(4), pp. 1640–1652.

39. Taddese AZ, Slawinski PR, Pirotta M, De Momi E, Obstein KL, Valdastri P. Enhanced real-time pose estimation for closed-loop robotic manipulation of magnetically actuated capsule endoscopes. The International Journal of Robotics Research. 2018, Vol. 37(8), pp. 890–911.

40. Hashi S, Tokunaga Y, Yabukami S, Toyoda M, Ishiyama K, Okazaki Y, et al. Development of real-time and highly accurate wireless motion capture system utilizing soft magnetic core. In: IEEE Transactions on Magnetics. 2005, pp. 4191–4193.

41. Hashi S, Yabukami S, Kanetaka H, Ishiyama K, Arai KI. Numerical Study on the Improvement of Detection Accuracy for a Wireless Motion Capture System. IEEE transactions on magnetics. 2009, Vol. 45(6), pp. 2736–2739.

42. Hashi S, Yabukami S, Kanetaka H, Ishiyama K, Arai KI. Wireless Magnetic Position-Sensing System Using Optimized Pickup Coils for Higher Accuracy. IEEE transactions on magnetics. 2011, Vol. 47(10), pp. 3542–3545.

43. Osaki Y, Hashi S, Yabukami S, Kanetaka H, Ishiyama K. Wireless Magnetic Position-Detection System With Four Excitation Coils. IEEE sensors journal. 2017, Vol. 17(14), pp. 4412–4419.

44. Guo X, Li S, Hao Y, Luo Z, Yan X. Pose tracking method using magnetic excitations with frequency division for robotic endoscopic capsules. Biomedical microdevices. 2022, Vol. 24(1), p. 9.

45. Aoki I, Uchiyama A, Arai K, Ishiyama K, Yabukami S. Detecting system of position and posture of capsule medical device. US20050216231A1, 2005.

46. Graumann R. Cable-free endoscopy method and system for determining in vivo position and orientation of an endoscopy capsule. US20050187479A1, 2005.

47. Plotkin A, Paperno E. 3-D magnetic tracking of a single subminiature coil with a large 2-D array of uniaxial transmitters. IEEE Transactions on Magnetics. 2003, Vol. 39(5), pp. 3295–3297.

48. Plotkin A, Kucher V, Horen Y, Paperno E. A New Calibration Procedure for Magnetic Tracking Systems. IEEE Transactions on Magnetics. 2008, Vol. 44(11), pp. 4525–4528.

49. Huang H, SanFilipo B, Oren A, Won IJ. Coaxial coil towed EMI sensor array for UXO detection and characterization. Journal of applied geophysics. 2007, Vol. 61(3), pp. 217–226.

50. Marsh LA, Ktistis C, Järvi A, Armitage DW, Peyton AJ. Three-dimensional object location and inversion of the magnetic polarizability tensor at a single frequency using a walk-through metal detector. Measurement Science and Technology. 2013, Vol. 24(4), pp. 45102-1–13.

51. Carpi F, Kastelein N, Talcott M, Pappone C. Magnetically Controllable Gastrointestinal Steering of Video Capsules. IEEE transactions on biomedical engineering. 2011, Vol. 58(2), pp. 231–234.

52. Arshak K, Adepoju F. Capsule tracking in the GI tract: a novel microcontroller based solution. In: Proceedings of the 2006 IEEE Sensors Applications Symposium, 2006, pp. 186–191.

53. Fluckiger M, Nelson BJ. Ultrasound Emitter Localization in Heterogeneous Media. In: 2007 29th Annual International Conference of the IEEE Engineering in Medicine and Biology Society. United States: IEEE; 2007, pp. 2867–2870.

54. Than TD, Alici G, Harvey S, O'Keefe G, Zhou H, Li W, et al. An Effective Localization Method for Robotic Endoscopic Capsules Using Multiple Positron Emission Markers. IEEE transactions on robotics. 2014, Vol. 30(5), pp. 1174–1186.

55. Karargyris A, Koulaouzidis A. OdoCapsule: Next-Generation Wireless Capsule Endoscopy With Accurate Lesion Localization and Video Stabilization Capabilities. IEEE transactions on biomedical engineering. 2015, Vol. 62(1), pp. 352–360.

56. Jokela J, Peyton AJ, Hyttinen J, Dekdouk B. A method for evaluating sensitivity of electromagnetic localization systems for wireless capsule endoscopes. In: 2022 44th Annual International Conference of the IEEE Engineering in Medicine and Biology Society (EMBC). Glasgow: IEEE; 2022, pp. 4872–4876.

57. Kwang MH, Yoon SO. Electromagnetic Fields. 1st ed. New York: Nova Science Publishers, Incorporated; 2013. 448 p.

58. Kraus JD. Electromagnetics with applications. 5th ed. Fleisch DA, Russ SH, editors. Boston (MA): McGraw-Hill; 1999. 617 p.

59. Ozdeger T, Davidson JL, van Verre W, Marsh LA, Lionheart WRB, Peyton AJ. Measuring the Magnetic Polarizability Tensor Using an Axial Multi-Coil Geometry. IEEE sensors journal. 2021, Vol. 21(17), pp. 19322–19333.

60. Dekdouk B, Ktistis C, Marsh LA, Armitage DW, Peyton AJ. Towards metal detection and identification for humanitarian demining using magnetic polarizability tensor spectroscopy. Measurement Science and Technology. 2015, Vol. 26(11), pp. 115501-1–17.

61. Dekdouk B, Ktistis C, Armitage DW, Peyton AJ. Absolute Imaging of Low Conductivity Material Distributions Using Nonlinear Reconstruction Methods in Magnetic Induction Tomography. Progress In Electromagnetics Research. 2016, Vol. 155, pp. 1–18.

62. Zienkiewicz OC, Taylor RL, Zhu JZ. The Finite Element Method: Its Basis and Fundamentals: Its Basis and Fundamentals. 7th ed. Oxford, United Kingdom: Elsevier Science & Technology; 2013, 753 p.

63. Marsh LA, Abdel Rehim OA, Tan YM, O'Toole MD, Armitage DW, Peyton AJ. Design of electromagnetic sensor arrays optimised for inversion of the magnetic polarisability tensor. In: 2015 IEEE Sensors Applications Symposium (SAS). IEEE; 2015, pp. 1–4.

64. Wang M. Understandable Electric Circuits. 1st ed. Vol. 23. Stevenage, United Kingdom: Institution of Engineering & Technology; 2010, 385 p.

65. Theilmann PT, Asbeck PM. An Analytical Model for Inductively Coupled Implantable Biomedical Devices With Ferrite Rods. IEEE Transactions on Biomedical Circuits and Systems. 2009, Vol. 3(1), pp. 43–52.

66. Caciagli A, Baars RJ, Philipse AP, Kuipers BWM. Exact expression for the magnetic field of a finite cylinder with arbitrary uniform magnetization. Journal of Magnetism and Magnetic Materials. 2018, Vol. 456, pp. 423–432.

67. Kaverine E, Palud S, Colombel F, Himdi M. Investigation on an Effective Magnetic Permeability of the Rod-Shaped Ferrites. Progress In Electromagnetics Research Letters. 2017, Vol. 65, pp. 43–48.

68. Sato M, Ishii Y. Simple and approximate expressions of demagnetizing factors of uniformly magnetized rectangular rod and cylinder. Journal of Applied Physics. 1989, Vol. 66(2), pp. 983–985.

69. Wang M, Feng J, Shi Y, Shen M. Demagnetization Weakening and Magnetic Field Concentration With Ferrite Core Characterization for Efficient Wireless Power Transfer. IEEE Transactions on Industrial Electronics. 2019, Vol. 66(3), pp. 1842–1851.

APPENDIX 1: MATLAB CODES FOR FIELD CALCULATOR

```
%
% Defines the model parameters for field calculator
% Takes a text file with coil coordinates as an input
% Jonna Jokela, 16/03/2022

%   USAGE           Model()
%
%   INPUT           Requests a text file as input
%                       - Transmit coils first in the file
%                       - Coils defined in the direction of current
%                       - Column 1: Number indicating the transmit/receive coil number
%                       - Column 2: n (Number indicating the order of the points in one coil)
%                       - Column 3: x-coordinate
%                       - Column 4: y-coordinate
%                       - Column 5: z-coordinate
%
%   OUTPUT          A structure with 11 fields:
%                       c           <-  coordinates of the coils
%                       coils       <-  Number of coils in the file
%                       RowIdx      <-  Starting and finishing rows of one coil
%                       corners     <-  Number of corners in each coil
%                       points      <-  Number of points in each coil
%                       maxlength   <-  Maximum length of a coil in the file
%                       A           <-  Coordinates of the coil corners
%                       AB          <-  Vectors formed by adjacent corners
%                       Lia         <-  Locigal vector to check for quadrupole coils
%                       NumRx       <-  Number of receive coils
%                       NumTx       <-  Number of transmit coils

function m = Model_calc2()

% Getting the coordinates from a text file
    file = uigetfile('*txt');
    c = readmatrix(file);
    c(any(isnan(c),2),:)=[];                    % Deleting the rows with string characters
    RxTx = find(c(:,1)==1,1,'last');
    ones = find(c(:,2)==1);                     % Identifying the number of coils in the file
    NumTx = find(ones(:,1)<RxTx,1,'last')-1;    % Number of transmit coils
    NumRx = length(ones)-NumTx;                 % Number of receive coils
    ratio = c(:,6);
    c = c(:,[3 4 5]);                           % Deleting the column with the order numbers

% Finding identical rows in the coordinates (= starting and finishing
% coordinates of one coil)
    s = 1;
    un = unique(c,'rows','stable'); % Unique rows in the coordinate matrix
    coils = length(c) - length(un); % Number of coils in the file, including the halves of a quadrupole coil
    RowIdx = zeros(2,coils);

        % Indices of the coil starting and finishing points
        for i = 1:coils
            RowIdx(:,i) = find(ismember(c(:,[1 2 3]), c(s,[1 2 3]),'rows'));
            s = s +RowIdx(2,i)-RowIdx(1,i)+1;
        end

    corners = RowIdx(2,:) - RowIdx(1,:);        % Number of corners in each coil
    points = corners + 1;                       % Number of points in each coil
    maxlength = max(RowIdx(2,:)-RowIdx(1,:));   % Maximum length of a coil in the file

% Checking if number of coils given by user is the same as the number
% calculated by starting and finishing points (logical vector indicating that)
    Lia = ismember(RowIdx(1,:),ones);

% Result matrices
    A = zeros(maxlength+1,3,coils);   % Coordinates of the corner points of the coil
    AB = zeros(maxlength,3,coils);    % Vectors formed by adjacent corners

for j = 1:coils

    % Define the limits of the wires of the coil in calculation
    for i = RowIdx(1,j):RowIdx(2,j)
        A(i-RowIdx(1,j)+1,:,j) = c(i,[1 2 3]);
    end
```

```
74
75          % Vectors formed by adjacent corners of the coil
76          for i = 1:corners(j)
77              AB(i,:,j) = A(i,:,j) - A(i+1,:,j);
78          end
79      end
80
81      % Structure containing all important parameters
82      m.c = c;
83      m.coils = coils;
84      m.RowIdx = RowIdx;
85      m.corners = corners;
86      m.points = points;
87      m.maxlength = maxlength;
88      m.A = A;
89      m.AB = AB;
90      m.Lia = Lia;
91      m.NumRx = NumRx;
92      m.NumTx = NumTx;
93      m.ratio = ratio;
94
```

Program 1. *Matlab code that defines the model parameters for field calculator.*

```
1   %
2   % Calculating the H-field using Biot-Savart law
3   % Takes coordinates of the coils as a text-file as an input
4   % H(P) = I/(4*pi*ro)*(sin(alfa2)-sin(alfa1))
5   % Jonna Jokela, 27/2/2022
6
7   %   USAGE           Field_calculator_matlab(Model, P)
8   %
9   %   INPUT           Model       <-      Matlab-model of a localization coil system
10  %                   P           <-      Coordinates of the points in ROI
11  %
12  %   OUTPUT          HxR         <-      x-component of the H-field of receive coils
13  %                   HyR         <-      y-component of the H-field of receive coils
14  %                   HzR         <-      z-component of the H-field of receive coils
15  %
16  %                   HxT         <-      x-component of the H-field of transmit coils
17  %                   HyT         <-      y-component of the H-field of transmit coils
18  %                   HzT         <-      z-component of the H-field of transmit coils
19
20  function [HxR,HyR,HzR,HxT,HyT,HzT] = Field_calculator_matlab_v5(m,P)
21
22  coils = m.coils;            % Number of coils, including halves of quadrupole coil
23  maxlength = m.maxlength;    % Maximum length of a coil
24
25  % The ROI where the field is calculated
26     %x_axis = -0.4:0.01:0.4;
27     %y_axis = -0.4:0.01:0.4;
28     %z_axis = 0.3;
29     %[x,y,z] = meshgrid(x_axis,y_axis,z_axis);
30     %P = [x(:),y(:),z(:)];
31
32  % Result matrices
33
34      % H_AB_d is H-field for straight wire, n is normal unit vector of the
35      % plane, p is projection and r is rejection
36      [H_AB_d, n, p, r] = deal(zeros(height(P),3,maxlength,coils));
37
38      AP = zeros(height(P),3,maxlength+1,coils);  % Vectors formed by corner points and point P
39      H_AB = zeros(height(P),1,maxlength,coils);  % The field magnitude for straight wire
40      ro = zeros(height(P),1,maxlength,coils);    % Distance from point p to the coil line
41      [alfa1, alfa2] = deal(zeros(height(P),maxlength,coils));    % Angles alfa1 and alfa2
42      H_d = zeros(height(P),3,coils);             % Total H-field of a coil
43
44
```

```
RowIdx = m.RowIdx;      % Starting and ending points of coils
corners = m.corners;    % Number of corners in the coils
points = m.points;      % Number of points in the coils
A = m.A;                % Coordinates of the coil corners
AB = m.AB;              % Vectors formed by adjacent corners
ratio = m.ratio;        % Ratio indicating the "current value"

ratio_index = ratio(RowIdx(1,:),:);

% Calculates the H-field for each coil of the system at each point of ROI
for j = 1:coils

    I = ratio_index(j)*(-1); % Current

    % Vectors formed by the corner points and point P
    for i = 1:height(P)
        for k = 1:points(j)
            AP(i,:,k,j) = A(k,:,j) - P(i,:);
        end
    end

    % Normal unit vector of the plane formed by three points (two corners and point P)
    for i = 1:height(P)
        for k = 1:corners(j)
            n(i,:,k,j) = cross(AP(i,:,k,j),AP(i,:,k+1,j))/norm(cross(AP(i,:,k,j),AP(i,:,k+1,j)));
        end
    end

    % Field by a straight wire
    % (for each straight wire in the coil, calculated at each point of ROI)
    for i = 1:height(P)
        for h = 1:corners(j)
            % Calculating the distance between point P and the line defined by adjacent
            % corner points
            ro(i,:,h,j) = norm(cross(AB(h,:,j),AP(i,:,h+1,j)))/norm(AB(h,:,j));

            % Calculating projection of AP on AB
            p(i,:,h,j) = dot(AP(i,:,h,j),AB(h,:,j))/(norm(AB(h,:,j))^2)*AB(h,:,j);

            % Rejection of AP from AB
            r(i,:,h,j) = AP(i,:,h,j) - p(i,:,h,j);

            % Calculating angles alfa1 and alfa2 and determining their sign
            alfa1(i,h,j) = sign(dot(cross(AP(i,:,h,j),r(i,:,h,j)),n(i,:,h,j)))*...
                acos(dot(AP(i,:,h,j),r(i,:,h,j))/(sqrt(sum(AP(i,:,h,j).^2)*sum(r(i,:,h,j).^2))));
            alfa2(i,h,j) = sign(dot(cross(AP(i,:,h+1,j),r(i,:,h,j)),n(i,:,h,j)))*...
                acos(dot(AP(i,:,h+1,j),r(i,:,h,j))/(sqrt(sum(AP(i,:,h+1,j).^2)*sum(r(i,:,h,j).^2))));

            % Calculating the field magnitude for a straight wire
            H_AB(i,:,h,j) = I/(4*pi*ro(i,:,h,j))*(sin(alfa2(i,h,j))-sin(alfa1(i,h,j)));

            % H-field with direction for a straight wire
            H_AB_d(i,:,h,j) = H_AB(i,:,h,j).*n(i,:,h,j);
        end
    end

    % Total field of one coil as a sum of straight wire fields
    for i = 1:corners(j)
        H_d(:,:,j) = H_d(:,:,j) + H_AB_d(:,:,i,j);
    end

end

NumTx = m.NumTx;    % Number of transmit coils
NumRx = m.NumRx;    % Number of receive coils

% Goes trough the field matrices and combines the fields for quadrupole
% coils

    % Result matrix
    H_d_corrected = zeros(height(P),3,NumRx+NumTx);

    Lia = m.Lia;    % Logical vector to check for quadrupole coils
```

```
118
119         % Sums up the fields of halves of quadrupole coils
120         j = 1;
121         for i = 1:coils
122             % If the coil belongs to the same group with the previous coil, its field is added to
123             % the field of the previous coil
124             if Lia(i) == 1
125                 H_d_corrected(:,:,j) = H_d(:,:,i);
126             elseif Lia(i) == 0
127                 H_d_corrected(:,:,j) = H_d_corrected(:,:,j) + H_d(:,:,i);
128             end
129             % Checking if the next coil belongs to the same group or not
130             if i == coils
131                 break
132             elseif Lia(i+1) == 1
133                 j = j + 1;
134             end
135         end
136
137
138     % Hx, Hy and Hz -components of the field
139         HxT(:,:) = H_d_corrected(:,1,1:NumTx); % H-field x-component (transmit)
140         HyT(:,:) = H_d_corrected(:,2,1:NumTx); % H-field y-component (transmit)
141         HzT(:,:) = H_d_corrected(:,3,1:NumTx); % H-field z-component (transmit)
142
143         HxR(:,:) = H_d_corrected(:,1,NumTx+1:end); % H-field x-component (receive)
144         HyR(:,:) = H_d_corrected(:,2,NumTx+1:end); % H-field y-component (receive)
145         HzR(:,:) = H_d_corrected(:,3,NumTx+1:end); % H-field z-component (receive)
146
147         HxT = HxT';
148         HyT = HyT';
149         HzT = HzT';
150         HxR = HxR';
151         HyR = HyR';
152         HzR = HzR';
153
154
155
156     % Magnitude of the H-field
157     H_corrected = zeros(height(P), 1, NumRx+NumTx);
158
159     for j = 1:size(H_d_corrected,3)
160         for i = 1:height(P)
161             H_corrected(i,1,j) = norm(H_d_corrected(i,:,j));
162         end
163     end
164
```

Program 2. *Matlab code for H-field calculator.*